QATAR UNIVERSITY

COLLEGE OF ENGINEERING

ENHANCEMENT OF THERMOELECTRIC PROPERTIES OF LOW-TOXIC AND EARTH-ABUNDANT CHALCOGENIDES

BY

FARHEEN FATHIMA JALDURGAM

A Thesis Submitted to

the College of Engineering

in Partial Fulfillment of the Requirements for the Degree of

Masters of Science in Electrical Engineering

June 2022

COMMITTEE PAGE

The members of the Committee approve the Thesis of
Farheen Fathima J defended on 09/05/2022.

Prof. Farid Touati
Thesis/Dissertation Supervisor

Dr. Zubair Ahmad
Thesis/Dissertation Co-Supervisor

Prof. Imaddin Al-Omari
Committee Member

Dr. Muhammad Salman Khan
Committee Member

Dr. Mohammaed Korany Hussan
Committee Member

Approved:

Khalid Kamal Naji, Dean, College of Engineering

ABSTRACT

FATHIMA, FARHEEN JALDURGAM, Masters : June : 2022,

Masters of Science in Electrical Engineering

Title: Enhancement of Thermoelectric Properties of low-toxic and earth-abundant chalcogenides

Supervisor of Thesis: Farid, Touati.

Co-Supervisor of Thesis: Zubair, Ahmad.

Thermoelectricity is a promising technology that directly converts heat energy into electricity and finds its use in enormous applications. This technology can be used for waste heat recovery from automobile exhausts and industrial sectors, and convert the heat from solar energy to electricity, especially in hot and humid areas such as Qatar. This work aims to develop high-performance Chalcogenide-based thermoelectric (TE) materials using sustainable sources that would further the ongoing activities in developing a cost-effective TE system. This research revolves around two main parts as follows:

The objective of the first part is to investigate the optimum sintering method and temperature that can improve the efficiency of bismuth telluride cold compact pellets for thermoelectric applications. Different p-type and n-type bismuth telluride cold compact pellets were treated using three different sintering techniques and conditions, namely pressure less (conventional), microwave, and tube (using argon environment) at temperatures 250 °C, 300 °C, 350 °C, and 400 °C. The structural, microscopic, electron transport, thermal, dielectric, and mechanical properties of the non-sintered or pristine and sintered samples were examined. Even though each type of sintering has its own merits and demerits, results showed that the optimum conditions for enhanced electric and thermal properties could be obtained using the

microwave sintering method, followed by the tube and conventional ones. Low thermal conductivity of 0.4 W/m/K was observed in the samples sintered at 250 °C while the increase in sintering temperature in all the three sintering methods from 250 °C to 400 °C improved the crystallinity of the material. These samples exhibited also excellent thermal and mechanical stability.

In the second part, we enhanced the thermoelectric properties of p-type copper selenide (Cu_2Se) which is a low toxic earth-abundant intermediate material for thermoelectric applications, by a low-cost simple, and fast microwave-assisted metallurgy route. Hot pressed copper selenide pellets were treated at various temperatures in the range of 250 ^oC to 425 ^oC in a microwave furnace. We analyze the variation of several characteristics of the samples, such as electrical, thermal, structural, microscopic, dielectric, and mechanical properties when the samples were exposed to different annealing conditions. Broadband dielectric spectroscopy (BDS) analysis was used to understand the variation with temperature and frequency of the AC electrical characteristics of the samples such as AC conductivity, dielectric permittivity storage, dielectric loss, and AC capacitance. The results indicate exceptional electrical, thermal, and mechanical properties for samples annealed at 375^oC with room temperature electrical conductivity as high as 538.3 S/cm and ultra-low thermal conductivity as low as 0.59 W/mK. The crystallinity of samples with the increase in annealing temperature from 250 ^oC to 725 ^oC along with the formation of oxides above 400 ^oC annealing temperature. The method used in this research to develop high-performance chalcogenide-based thermoelectrics is a low-cost, simple, and quick process that has produced TE materials with excellent electrical, thermal, and mechanical characteristics.

DEDICATION

This thesis is dedicated to my husband Kareem and my son Yahya who supported me endlessly and were patient throughout my journey. Thanks for making me see this adventure through to the end.

ACKNOWLEDGMENTS

In the name of Allah, the Most Gracious and the Most Merciful, all praises to Allah for blessing me with strength and knowledge to complete this work.

Firstly, I would like to present my sincere gratitude to my Supervisor, Prof. Farid Touati for his valuable guidance throughout my Master studies. I would also like to extend my gratefulness to Dr. Zubair Ahmad (Qatar University-Young Scientists Center), my co-supervisor, for his enormous guidance and support.

I would like to also acknowledge Dr. Noora Al Thani (Qatar University-Young Scientists Center), Dr. Jolly Bhadra (Qatar University-Young Scientists Center), and Dr. R.A. Shakoor (Center of Advanced materials) for their positive feedback and motivation.

I also thank Dr. Nasser Abdullah Al Nuaimi (Associate Vice President for Research & Graduate Studies and Former Director of CAM), Dr. Mohammad R. Irshidat (Acting Director of CAM), and Dr. Peter Kasak (Technical Manager CAM) for their support at CAM. My special thanks to Mr. Moinuddin Mohammed Yusuf, Mr. Abdulla Al Ashraf, and Mr. Abdul Jaleel Naushad, the technical staff of CAM for their technical support during my thesis studies.

I owe my special gratitude to my colleagues Mr. Indra Gunawan, Ms. Sumayya M. Abdulrahim, Dr. Shoaib Alam Mallick, Dr. Arti Mishra, Mr. Jefin James Abraham, and Ms. Rokaya Abdelatty for developing a dynamic and friendly atmosphere.I also express my gratefulness to Qatar University, Center of Advanced Materials, QU-Young Scientist center for providing me facilities and technical assistance throughout my thesis research work.

Finally, and most importantly, a special thanks to my husband and son for their encouragement and support.

TABLE OF CONTENTS

LIST OF TABLES

LIST OF FIGURES

CHAPTER 1: INTRODUCTION

Global warming, climate change, environmental pollution, and the global fossil energy crisis have emphasized the rapid and steady increase in the research and development of healthy and sustainable energy resources. Green technology is a term used to describe technology that is deemed ecologically benign due to its manufacturing process or supply chain. The use of alternative fuels, clean energy generation, and technologies that are less detrimental to the environment than fossil fuels are all included under the term "green tech". Even though green technology is still relatively new, it has attracted a lot of interest as people have become more conscious of the depletion of natural resources and the effects of climate change. Green energy is an important category of green technology and is a feasible alternative to fossil fuels and is a carbon-neutral energy source. Some of the green energy sources are solar energy, wind energy, tidal energy, hydro energy, thermal energy, etc.

1.1 Green energy:

1.1.1 Solar energy:

The heat and light of the sun constitute solar energy. The sun’s energy can be harnessed in different ways: Photovoltaic cells or solar cells that produce electricity from sunlight, solar thermal technology that uses the sun’s heat to generate steam or hot water that in turn generates electricity, and passive solar heating that is as easy as allowing sunlight to flow through the windows to warm the interior of the buildings.

1.1.2 Wind energy:

The wind is a renewable energy source that is free, clean, and easily available. Wind turbines capture the wind's energy and convert it to electricity every day all around the world. Wind turbines allow us to harness the wind's energy-generating potential.

The turbine's blades rotate clockwise as the wind blows, collecting energy. This causes the wind turbine's primary shaft, which is coupled to a gearbox within the nacelle, to spin. The gearbox converts the wind energy into electricity and transmits it to the generator. The electricity is then sent to a transformer, which adjusts the voltage levels to match the grid.

1.1.3 Tidal energy:

Tidal energy is a renewable source of energy that is derived from the natural rise and fall of ocean currents and tides. Turbines and paddles are two examples of this technology. Tidal energy is obtained in three ways: tidal streams, barrages, and tidal lagoons. Turbines are situated in tidal streams for the majority of tidal energy producers. Tides form a fast-flowing body of water known as a tidal stream. A turbine is a mechanical device that extracts energy from a fluid flow. This fluid can be either wind or water. Tidal energy is more potent than wind energy because water is denser than air. Tides, unlike wind, are predictable and consistent. Tidal generators generate a continuous, consistent supply of energy wherever they are employed.

1.1.4 Hydro energy:

The energy created by hydropower is renewable since it is based on the water cycle, which is driven by the sun. Hydropower is a clean form of energy since it is powered by water. Hydroelectric power, unlike power stations that use fossil fuels like coal or natural gas, does not contaminate the air. Some hydropower plants may move from zero to full production in a couple of moments. Hydropower facilities offer vital backup power during large energy outages or disturbances because they can produce power to the system promptly. When demand is high, technologies like pumped storage hydropower (PSH) store energy to be used in conjunction with renewables like solar and wind power.

1.1.5 Thermal energy:

Thermal energy is mainly used for heating and cooling in industrial systems, buildings, commercial cooking applications, and domestic hot water. Renewable thermal energy uses energy and resources that would otherwise be spent or dissipated to supply thermal energy from sources that renew themselves over a short period of time. Thermoelectric generators otherwise known as TEGs work on the principle of thermoelectricity and are a type of energy harvester and environmentally friendly power production devices that convert thermal energy directly into electrical energy.

1.2 Thermoelectric technology:

Thermoelectric energy (TE) converters are one of the viable technologies that are of increasing interest and are widely investigated for this purpose since these noiseless solid-state devices can transform heat or temperature gradient into electricity and vice versa that is given off from various sources such as automobiles, factories, power plants, spacecraft, electronic devices or even our human bodies based on the Seebeck and Peltier effects [1, 2]. Figure 1-1 gives an overview of the global energy harvesting market classified by technologies [3].

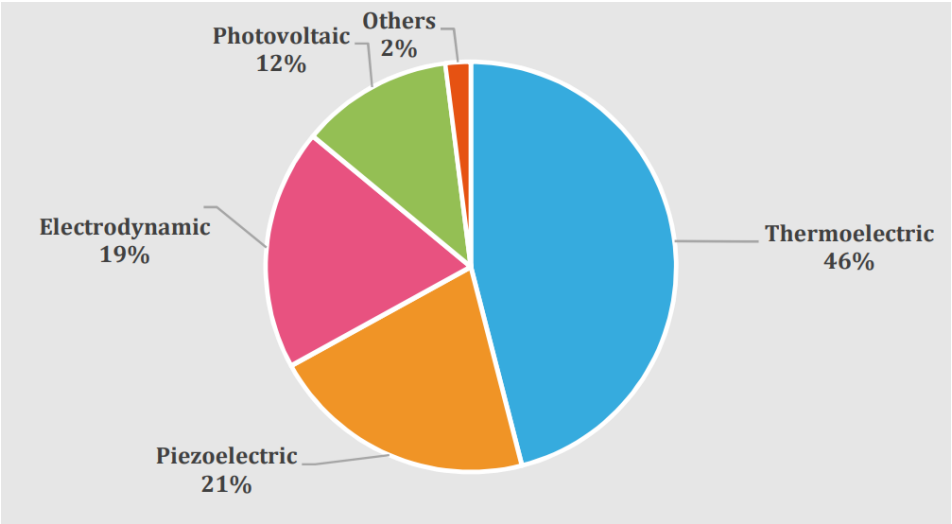

Figure 1-1. Global energy harvesting market [3].

1.3 What are thermoelectric materials:

Thermoelectric materials, are typically semiconductors, and are used to design thermoelectric generators that convert heat to electricity and vice versa. To generate electricity, they use the concept of temperature differential. Despite their numerous benefits, TEGs are mostly used in space technology and high-end applications. Only a few materials, such as Bi_2Te_s, PbTe, SiGe, and their alloys, were employed towards the end of the 1990s. Because of their great performance at ambient temperature, these materials are commonly used in generators and freezers. The ratio of energy gain to input energy is described as the figure of merit or efficiency of TE. Although the figure of merit ZT value for materials has no theoretical limit, these bulk thermoelectric materials have ZT values in the range of 1 to 2. Since the early twenty-first century, great progress has been made in improving thermoelectric characteristics by producing nanostructured materials like as nanowires. Due to the high prices and toxicity of the rare materials utilized in design, their adoption in mainstream applications has been hampered. Other eco-friendly and plentiful materials mentioned by the researchers include chalcogenides and silicides.

1.4 Thermoelectric classifications:

Based on the operating temperatures, thermoelectric materials are classified into three categories:

i. Low-temperature thermoelectric materials operating from room temperature to around 473 K (e.g., Bismuth, Antimony, Lead, etc.). Bismuth Telluride is the most widely used material in commercially available thermoelectric modules whose ZT is nearly unity at 50 ^{o}C. The application of these materials is mainly for cooling, air conditioning, and refrigeration purposes. Toxicity, heaviness, and high cost due to the low abundance of traditional materials have limited

the use of thermoelectric materials in typical applications. For a long, manufacturers are in search of an inexpensive and eco-friendly replacement, which can be used in large-scale production. Organic Thermoelectric materials also can be used for energy harvesting in this temperature range. They are low-cost, flexible, and easy to manufacture and reproduce on a large scale.

ii. Intermediate temperature thermoelectric materials, ranging between 500-900 K (e.g., Skutterudites, Tin, Half-Heusler, etc.). Copper-based chalcogenides are appropriate low-toxic and low-cost materials in this range of temperature and can be used for waste heat recovery in industries, and automobiles.

iii. High-temperature thermoelectric materials of application temperatures higher than 900 K (Silicon, Germanium, etc.). Silicon-Germanium alloys have for a long time been used in space applications due to their high performance at temperatures beyond 900 K. But the rarity and thermal instability of germanium has increased the production cost of such materials. Since then, several silicon-based alloys (Magnesium silicide Manganese Silicide, Iron disilicide, Cobalt monosilicide, etc.) have been developed to reduce the cost and increase its availability.

1.5 Chalcogenides as thermoelectric materials:

The crystal structure of a PGEC material is commonly made up of two sublattices: one acts like an electrically conducting network, while the other functions as a thermal blocker and charge storage. Chalcogenides are compounds made up of at least one-chalcogen element atoms, such as tellurium, selenium, or sulfur. Chalcogenides especially copper-based, recently have emerged as a family of novel promising systems with enormous potential for power generation. They are better alternatives to the high-toxic traditional lead-based thermoelectric materials and are ecofriendly and

inexpensive contenders for sustainable thermoelectrics. For instance, bismuth telluride and copper selenide are chalcogenide materials for low-temperature range and intermediate temperature range applications, respectively.

1.6 Motivation and background:

The development of sustainable thermoelectrics is highly significant in waste-heat power conversion in several industrial and space applications. An ideal thermoelectric material can be selected depending upon the characteristics of the material such as electrical conductivity, thermal conductivity, Seebeck coefficient, and power factor that highly influence the figure of merit or efficiency of the overall thermoelectric module. Along with these characteristics, the material must be low toxic, inexpensive, and easily available in nature (abundant). The thermal and mechanical stability is critical for the endurance of the thermoelectric generators in robust practical applications. The synthesis technique also affects the development of sustainable thermoelectrics. The methods used to develop such efficient devices must be easy, simple, reliable, reproducible, scalable, and must provide superior characteristics to the materials. The motivation of this research work is to develop low-cost sustainable chalcogenide-based thermoelectric materials through simple and reproducible metallurgy routes and enhance the microstructure, electrical, thermal, and mechanical properties.

1.7 Research problem:

The high cost and toxicity have limited the use of thermoelectric materials for ordinary applications. Despite the significant development of traditional thermoelectric materials and generators both in terms of efficiency and practical applications, the need for low-toxic, earth-abundant and sustainable thermoelectric devices has been garnered a lot of attention over the past decade. The development of

materials such as copper-based chalcogenides is still in its infancy and enhancement of electrical, thermal, and mechanical characteristics is necessary for its successful commercialization. Thus, we need to develop highly efficient eco-friendly chalcogenide-based TE materials that have superior properties and will tend to replace the existing high toxic and expensive TE materials. The ecotoxicity of bismuth telluride and copper selenide is not considered hazardous to the environment. The market price of bismuth, telluride, copper, and selenium are 10.34 USD/kg, 55.68 USD/kg, 5.9 USD/kg, and 30.37 USD/kg, respectively (http://www.leonland.de/elements_by_price/en/list). Additionally, the scalability of cold compaction is superior when compared to the other consolidation methods and microwave annealing has also superior scalability among the other sintering methods. As such, we will develop both p-type and n-type bismuth telluride TE materials for low-temperature range applications and p-type copper selenide TE material for intermediate temperature range applications using low-cost, simple, and scalable metallurgy route.

1.8 Research objective:

This research aims on designing chalcogenide-based TE materials that have superior electrical, thermal, structural, dielectric, and mechanical properties. Different sintering methods such as conventional sintering, microwave sintering, and tube sintering have been employed to improve the figure of merit of the TE materials. We investigate the thermoelectric properties of both bismuth telluride and copper selenide TE materials and their applications in low-temperature and intermediate-temperature ranges. Our first objective is to compact the raw material powders by cold compaction and hot pressing to accommodate the sintering methods. The second objective is to study the effect of different sintering techniques and sintering temperatures on the

properties of both p-type and n-type cold-compacted bismuth telluride pellets. We use a hot pressing and microwave-assisted metallurgy route to prepare high-efficient p-type copper selenide TE materials. We study the thermoelectric properties of all the prepared samples and analyze the results with the existing studies. Finally, we conduct broadband dielectric spectroscopy to assess the temperature and frequency response of the samples.

1.9 Main contribution:

The following are the specific contributions to the body of knowledge made by this research work:

- Optimized the sintering method and sintering temperature for p-type and n-type bismuth telluride thermoelectric material in the conventional, microwave, and tube furnaces.
- Enhance the thermoelectric properties of p-type copper selenide by optimizing the sintering temperature of the microwave-assisted metallurgy route.
- Studied the structural, microscopic, electric, and thermal properties of the as-prepared and sintered samples.
- Conducted thorough Broadband dielectric spectroscopy analysis to determine the dielectric properties of the prepared materials.
- Analyzed the thermal and mechanical stability study of the prepared materials for durability in a practical environment.
- Comparison of pros and cons of the different sintering techniques in terms of efficiency, speed, complexity, and cost.
- Investigation of facile, and cost-effective method for preparation of high-performance chalcogenide-based thermoelectric materials.

1.10 Thesis organization:

This thesis has been organized as follows:

- Chapter 1 covers different green technologies for power generation applications. Gives brief information about thermoelectric technology, thermoelectric materials, and their classifications. This chapter also contains the motivation and background and outlines the research problems and objectives along with the contributions of this thesis.
- Chapter 2 covers the concepts of thermoelectricity such as the Peltier and Seebeck effect and Phonon-glass electron-crystal (PGEC) concepts. It also covers the properties of the thermoelectric materials and a brief literature review of bismuth telluride and copper selenide TE materials.
- Chapter 3 consists of the different materials and characterization methods that have been used throughout this research work.
- Chapter 4 addresses the investigation of the optimum sintering method and sintering temperature for high-performance bismuth telluride for thermoelectric applications.
- Chapter 5 presents the enhancement of thermoelectric properties of copper selenide TE material.
- Chapter 6 summarizes the research work provided by this thesis work and directs towards the future aspect of this work.

CHAPTER 2: THEORY AND LITERATURE REVIEW

2.1 Introduction:

In this chapter, we will study the theory behind thermoelectric technology and the materials used for TE applications. We will also explore the characteristics of the TE material and its effect on the efficiency or figure of merit of the TE generator. We will also investigate the existing works on bismuth telluride and copper selenide.

2.2 Seebeck and Peltier effects:

2.2.1 Seebeck effect:

An electromotive force (voltage) is created by introducing a temperature gradient across any isolated conducting material; this effect is known as the Seebeck effect defined as follows:

$$S = {}^{\Delta E_{emf}}/_{\Delta T}$$

The Seebeck effect typically describes the formation of electric potential difference across a conductor or semiconductor as a result of diffusion of charge carriers along the temperature gradient which is the difference between the temperature on the hot side to temperature in the cold side ($\Delta T=T_H-T_C$, where T_H and T_C are the hot and cold side temperature, respectively). The charges travel from the hot side to the cold side causing the charge carriers gradient and are balanced by the electric field internally at the equilibrium state. The Seebeck effect is represented in Figure 2-1(a).

2.2.2 Peltier effect:

The presence of cooling or heating at an electrified junction of two distinct conductors is known as the Peltier Effect. Heat can be supplied or removed at a junction between two conductors when a current is made to flow through it. The Peltier Effect could be thought of as the Seebeck Effect's back-action counterpart. To regulate the variation in chemical potential between the two materials, the electrical current passing through

the junction linking the two materials will produce or absorb heat per unit time at the junction. The representation of the Peltier effect is illustrated in Figure 2-1(b).

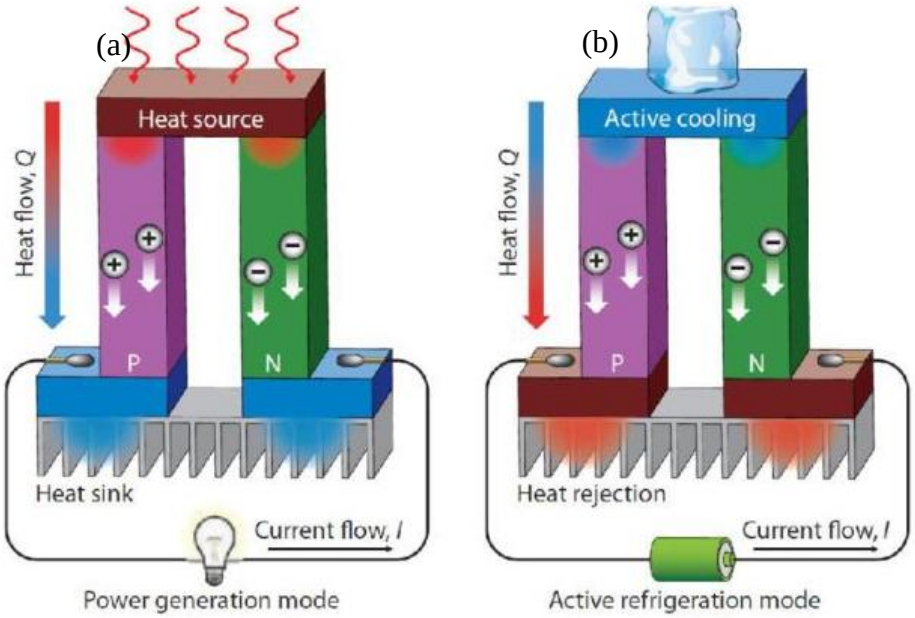

Figure 2-1. (a) Seebeck and (b) Peltier effect representation [4].

2.3 Phonon glass electron crystal concept:

The notion of a "phonon-glass electron-single-crystal," initially proposed by Slack and detailed in his study, is at the center of research into semiconductors with "glass-like" thermal conductivity values that may be preferable for thermoelectric applications [5]. Electronic characteristics of PGEC materials would be similar to those of excellent semiconductor single crystals, while thermal properties would be similar to those of amorphous materials. One of the most significant advances in the area of thermoelectrics in the last 30 years was the introduction of the PGEC idea. Practically, such a material is easy to identify but difficult to engineer. The main principle of the PGEC concept is to reduce the thermal conductivity, more importantly, the lattice thermal conductivity of the material.

2.4 Properties of thermoelectric materials:

The efficiency of thermoelectric materials is often termed as the Figure of merit (ZT)

is given by

$$Z = \frac{(\alpha_p - \alpha_n)^2}{((k_p.\rho_p)^{1/2} + (k_n.\rho_n)^{1/2})^2}$$

Where α_p & α_n are the Seebeck coefficients of the two materials of the thermocouple, ρ_p & ρ_n are the electrical resistivities, and k_p & k_n are the thermal conductivities.

ZT is the product of the temperature difference and the figure of merit and is called the dimensionless figure of merit and for a single material can be given by

$$ZT = \frac{\alpha^2 T}{k\rho} = \frac{\alpha^2 \sigma T}{k}$$

$$T = (T_H - T_C)/2$$

Where, T_H is the hot side temperature, T_C is the cold side temperature of the modules, σ and k are the electrical and thermal conductivity of the material, respectively. For a highly efficient material, the ZT should be very high. To maximize ZT, the material requires having high electrical conductivity, low thermal conductivity, high Seebeck coefficient, and high-power factor.

2.4.1 Electrical conductivity:

The electrical conductivity is given by the following equation:

$$I = \frac{\sigma V A}{L}$$

Where A and L are the cross-section area and length of the specimen, respectively.

I and V are the current passing through the specimen and voltage applied, respectively. From the PGEC concept, for good thermoelectric material, the electrical conductivity must be as high as possible. Amorphous semiconductors have very low electrical conductivities and excellent electrical conductivity is correlated with single-crystal semiconductors.

2.4.2 Thermal conductivity:

The thermal conductivity (k) comprises two principal components- lattice thermal conductivity (k_L) and electronic thermal conductivity (k_e) depending upon the contribution of phonons and charge carriers, respectively. A good thermoelectric material must demonstrate low thermal conductivity suggesting a lower flow of heat through the material at a certain gradient of temperature. The lowest k_L was found in glass. The thermal conductivity is given by

$$k = \frac{-Q}{\Delta T}$$

Where Q and T are the heat flow rate and absolute temperature, respectively.

2.4.3 Seebeck coefficient:

The Seebeck coefficient is defined as the ratio of potential difference across the free ends V to the temperature difference ΔT. It is denoted by α_{AB} and is given by

$$\alpha_{AB} = \frac{V}{\Delta T}$$

The Seebeck coefficient is also called the thermal electromagnetic field coefficient or thermoelectric power. For a good thermoelectric material, the Seebeck coefficient must be as high as possible.

2.4.4 Power factor:

The power factor comprises of both electrical conductivity and Seebeck coefficient and is given by

$$P.F = \alpha^2.\sigma$$

Where σ and α are electrical conductivity and Seebeck coefficient, respectively. The power factor mainly depends on carrier concentration since both σ and α depend strongly on it. The material that has the highest figure of merit is the one with the carrier concentration that has generated the largest power factor.

2.5 Approaches to improve the figure of merit value of thermoelectrics:

The wide application of thermoelectric generators relies primarily on two parameters: (1) materials that are low toxic and earth-abundant, and (2) synthesis techniques that are simple, easy, low cost, quick, scalable, and reliable. The methods must enhance the thermoelectric properties of the materials and be replicable or reproducible. The focus on advanced nanostructures, with an ultimate goal towards the materials made from sustainable, earth-abundant, economic, and non-toxic resources to replace conventional dopped with rare-earth elements, is definitely a good subject for future study. To fully explore this multidisciplinary research, a combined computational-experimental approach is necessary. There is a need to utilize the multidisciplinary (Materials Science, Physics, Engineering) collaborative environment to design truly extraordinary TE materials by grain boundary and interface engineering. The general approach should be to independently optimize the doping, electronic band structure, and thermal conductivity of complex TE semiconductor composites to maximize the ZT. The interaction between the material's parameters such as defects, alloy composition, and microstructure should be understood by modifying the material properties such as electron concentration (doping), effective mass, and lattice thermal conductivity (increasing the ratio μ/κl of quality factor that determines ZT).

The improvement in thermoelectric properties mainly relies on two factors, including minimizing the thermal lattice conductivities and increasing the electrical conductivity. The thermal conductivity can be reduced by a) nanostructuring and b) complex crystal structure. In fact, thermal conductivity comprises two parts: κ_e (due to heat-carrying electrons or holes charge carriers) and κ_L (lattice thermal conductivity). 2D structures such as superlattices and quantum wells and 1D structures like nanowires have been shown to significantly enhance the ZT by lowering the lattice thermal conductivity. Even though the complex crystal structures have limited phonon

mean free path, however, the elucidation and identification of the structural component influencing the transport properties are tricky.

To increase the electrical conductivity in the higher energy levels, resonant doping has proven an effective technique; however, successful identification of optimal resonant dopants is a herculean task. The high Seebeck coefficient is originated from the heavier density-of-states effective mass. This, in turn, leads to an enrichment of the thermoelectric properties of the material by the rise in the Seebeck coefficient and power factor. Zero-dimensional Point defects, one-dimensional linear defects, two-dimensional planar defects, and three-dimensional bulk defects are also induced in the materials for optimizing their thermoelectric properties. The introduction of these defects influences the physical parameters of the material and tunes the carrier concentration causing an enhancement in both the Seebeck coefficient and electrical conductivity. Research on complex point defects impacting the band structure is necessary for further expansion of thermoelectric applications.

The focus now needs to be shifted on superiorizing the thermoelectric power factor by enhancing the Seebeck coefficient. Quantum confinement engineering, distortion of electronic band structure by resonant impurity states, hot carrier filtering, or improving the number of carrier pockets near the band edges (larger band multiplicity) are some suggestions along this direction.

Nevertheless, to date, there are no vivid roadmaps for accomplishing many of these goals. Computational advancements and theoretical tools can aid in the quest to discover or innovate new TE materials. Better identification of the underlying factors for efficient correlation of the phonon and electron interactions can also contribute to elevated thermoelectric power. Few TE materials have been engineered using these techniques, and many more are yet to be explored both in theoretical and practical

terms. The future high-performance TE materials engineered must have a perfect balance between superior power factors and reduced thermal conductivities.

Currently, available consolidation processes have led to crystal domain growth, atomic redistribution, stoichiometric changes, phase or alloying segregation, and interface redefinition. A significant advancement in the surface chemistry engineering of nanoparticles is necessary to overcome these issues for better charge transport properties. Moreover, TE applications at high temperatures require extraordinary stabilization processes that avoid any unstable nanostructured assemblies.

The critical limitation of nanoparticle-based processes is difficulty in scaling and reproducing the materials with the same and exact features. To address this issue, significant improvements in the simple and straightforward engineering and design of the TE materials are required. These improvements must also accommodate the cost and volume of the highly functional nanomaterials. Another barrier in engineering high yield TE nanocomposites is the inferior understanding available on the transport features of the complex systems. Information on the precise effect of phase distributions, interfaces, quantum confinement, and crystal domain size on the performance is necessary. Better computational modeling, along with a large number of experimental characterizations of system models with tuned parameters, can assist in this aspect. The performance of TE materials is essentially measured by the figure of merit value the product material achieves. This belief in some way has restricted the growth of novel materials and processing techniques.

In printed TEGs, layer adhesion and crack formation are common difficulties that restrict the production of dense layers with adequate thickness. The nascent 3D printing technology offers some relief in overcoming these difficulties. However, it remains to be seen whether these technologies would suffice the throughput

requirements of the industries. Another thing is that the materials that are to be designed should consider their most plausible final application. Even with optimum cost and efficiencies, thermoelectrics cannot compete on a large scale with the existing steam engines or compressor-based refrigerators. The thing that makes thermoelectrics unique is the very accurate temperature control they provide, the capability to harvest small temperature gradients, their portability, their wide scalability, and their effectiveness at a very small scale. So, to summarize, the future of TE strongly relies on our capability to develop novel materials with optimized performance.

2.6 Background on bismuth telluride:

Bismuth telluride is a highly investigated material with a well-developed manufacturing approach for module design lowering any technical development risk. Yamashita *et al.* [6] prepared p-type and n-type Bi_2Te_3 TE materials using Bridgman method resulting in a ZT of 1.41 and 1.13, respectively. The introduction of copper telluride to bismuth telluride has resulted in a state-of-the-art electrical conductivity of $0.8*10^6$ $S\text{-}m^{-1}$ [7]. Additionally, ultra-low lattice thermal conductivity of 0.2 W/mK at 373 K was reported for Te-doped Bi2Te3 samples [8]. Zhou *et al*. [9] used the microwave-assisted polyol method to synthesize nanocrystalline Bi_2Te_3 with a combination of nanorods and hexagonal nanoflakes of length ranging from 200 to 400 nm and 90 to 150 nm, respectively. Kim *et al*. [10] used three different methods, namely the chemical reaction method, conventional pulverization method, and gas atomization method, to prepare the starting powders of nanostructured Bi_2Te_3 alloys. In the traditional pulverization method, the materials bismuth, tellurium, and antimony were mixed and treated in a quartz tube at 1000 ^oC temperature for 24 h. Their work suggested better crystal orientation alignment for enhanced TE

characteristics. High-quality bismuth selenide (Bi_2Se_3) single-crystalline bulk TE materials were synthesized in a 12-inch horizontal quartz tube furnace and heated in the 450-580^oC temperature range for 1-5 h [11]. Ashalley *et al*. reviewed in detail the characteristics and synthesis methods to realize various nanostructured Bi_2Te_3 materials (0D, 1D, 2D, and nanocomposites) [12]. Anandan *et al*. [13] investigated the influence of sintering temperature on the phase transformation and morphological evolution in a wet chemical synthesized Bi_2Te_3 nanocrystal pellets. Phase change to BiTe was observed at high sintering temperatures, and this BiTe phase dominated the Bi_2Te_3 phase at 773 K. Usually, the chemical methods lack efficient reproducibility in bulk production [14]. The bismuth telluride alloys prepared by the horizontal zone melting technique exhibited an average Vickers hardness of 85 ± 10 HV [15]. The bending strength of n-type Bi_2Te_3 fabricated via mechanical alloying and spark plasma sintering (SPS) was enhanced to 120 MPa after the hot forging. Zhao *et al.* [16] fabricated mechanically superior n-type nano-SiC dispersed Bi_2Te_3 compounds by mechanical alloying and SPS. Ball milling and SPS remarkably enhanced the mechanical strength to 2-3 times the p-type and n-type bismuth telluride ingots [17]. The increase in Te concentration weakened the microhardness of $Bi_{0.5}Sb_{1.5}Te_3$ [18]. The compressive strengths of 3D printed bismuth telluride alloys prepared from selective laser melting techniques reached a superior value of 91 MPa [19]. Even though these works have comparatively better mechanical stability, they lag either in their electrical or thermal properties. The ideal resultant TE material should have a perfect balance between electrical, thermal, and mechanical properties.

2.7 Background on copper selenide:

Initial Studies on copper selenide suggested that the copper selenide had a p-type conduction mechanism from the thermoelectric power and Seebeck coefficient

measurements [20, 21]. Prior studies developed high-performance nanostructured Cu_2Se thermoelectric materials using different methods such as solvothermal chemical reactions, high-temperature melting, annealing, dry and wet high energy ball milling, hot pressing, spark plasma sintering, etc., to name a few [22]. A figure of merit greater than two has been achieved by some renowned works [23]. Tyagi *et al*. [24] synthesized nanostructured Cu_2Se with a ZT~1.4 at 973 K by a combination of high-energy ball milling and spark plasma sintering. Microwave-assisted methods were also used in a few previous works, but it was mainly used to synthesize Copper selenide-based thin films [25-27]. Shi *et al*. [28] used conventional sintering to develop Cu_2Se with ZT~1.2 for samples annealed at 1173 K for 2 h. But in all these cases, the mechanical durability of the synthesized materials that is essential to determine the reliability in practical environments is hardly reported. The materials consolidated by hot isostatic pressing have better microstructure and reduced porosity, thereby increasing the mechanical strength of the materials with increased ductility, impact strength, and tensile strength [29].

2.8 Recent progress of figure of merit of low-toxic and earth-abundant thermoelectric materials

Figure 2-2 represents recent advancements in the low-toxic and earth-abundant TE materials, and their figure of merit (ZTmax) attained at low, intermediate, and high temperatures. These materials are sufficiently available and harmlessly disposable and consist of various low toxic silicides, Zintl compounds, and copper-base alloys, including copper sulfides and copper iodides. These materials possess enormous advantages and have room for further improvements, making them potential competitors to the traditional TE materials. For instance, silicides such as silicon germanium are available since the first synthesis of thermoelectric materials. They are

mainly used in space applications, with the only drawback of germanium's high fabrication cost, but over time, the researchers have resolved this issue by using lower amounts of germanium or replacing germanium with low-toxic and abundantly available materials such as magnesium, manganese, chromium, etc. Along with silicon, these materials form various silicides that have both the benefits of traditional silicides and eco-friendliness. The ZT value for such silicides has been successfully attained >1; even, in some cases, it has been reported to be over 1.5 (see Figure 2-2 (b)).

Similarly, the Zintl compounds are a subgroup of intermetallic compounds, initially comprising toxic and rare-earth materials, but lately, a few Zintl compounds, such as Ca_3AlSb_3, Mg_3Sb_2, $CaAl_2Si_2$, etc., have also been developed that have the benefits of Zintls as well as low toxicity and abundancy. Low-toxic Zintls likewise have good potential for commercialization for heat recovery applications. The average ZT value for such materials lies in the range of 0.8 ± 0.2, as shown in Figure 2-2 (c). Figure 2-2 (d) shows that copper sulfides (with a mean ZT value >1.2) also exhibit great potential for the intermediate and high-temperature range of low-toxic and geo abundant thermoelectric materials. In a case study of copper sulfides doped with trace amounts of rare-earth chalcogenides, the highest ZT value >2 is reported. However, low values of ZT have been observed in copper iodide and its alloys, as shown in Figure 2-2 (e). In the low-temperature range applications, copper iodide is a transparent and flexible thermoelectric material. Its maximum ZT value is deficient (~0.3) compared to other TE materials in this temperature range.

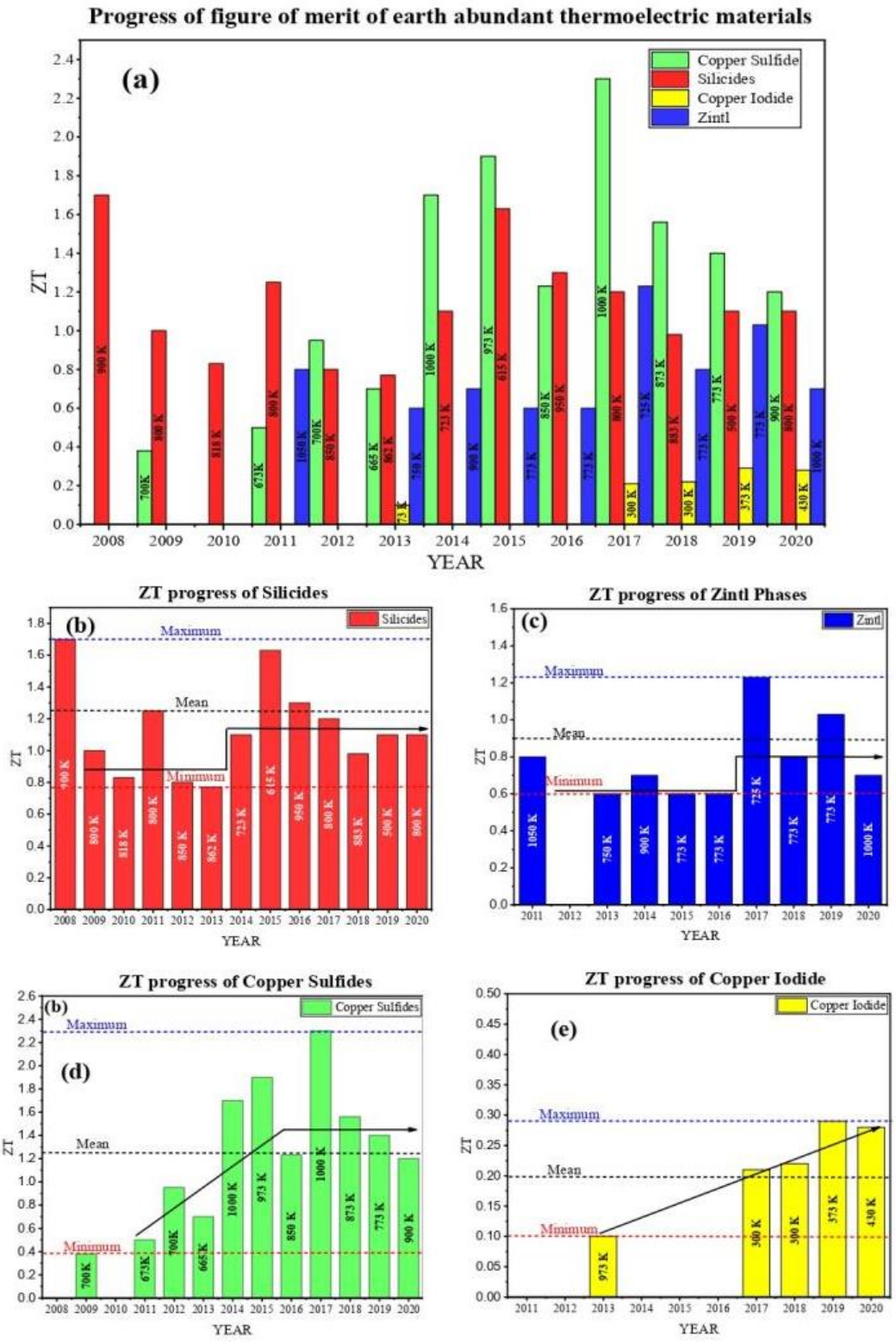

Figure 2-2. (a) Recent progress of figure of merit (ZT_{max}) of Earth-abundant low-toxic thermoelectric materials; Low-temperature thermoelectric materials (copper iodide and its alloys), Intermediate and high-temperature thermoelectric materials (copper sulfides, silicides, Zintl compounds, and their alloys) from the year 2008–2020. The

temperatures at which the maximum ZT is recorded are mentioned in the bar charts. (b) silicides, (c) Zintl compounds, (d) copper sulfides, (e) copper iodide.

2.9 Recent Advancements in Large-Scale Thermoelectric Synthesis and Fabrication Methods:

Table 2-1 gives a detailed summary of the processing cost, time, scalability, the figure of merit ranges, strengths, and drawbacks of different techniques. The microwave (MW)-assisted hydro or solvothermal method is mostly used to synthesize nanostructures in inorganic materials such as Bi_2S_3, SnTe, etc. Solvothermal or hydrothermal is an old method that has proven advantageous in producing highly crystalline nanostructures with high purity, narrow size distribution, and low aggregation. This MW-hydrothermal/solvothermal method combines and possesses the merits of both the hydrothermal/solvothermal and microwave approaches. These methods combined with microwave synthesis provide short sintering times, low temperatures, economic processing, rapid diffusion energies, and the existence of highly crystalline nanostructures. These are the features that are essential for successful large-scale manufacturing. Existing works show that the figure of merit for the materials with microwave-assisted synthesis is close to 2 (ZT ≈2 at 873 K for SnSe [15]) with maximum scalability of up to 10 g. However, this method requires a long reaction time, complex equipment, and high energy consumption. Some of the other materials that can be synthesized from these methods are metal oxides, hydroxides, metal composite oxides, inorganic biomaterials, and metal sulfides and can be used in areas such as gas sensors, photocatalytic, electrochemical, solar cell, and optical applications [16]. Chemical synthesis involves solution-phase chemical reactions using precursors at appropriate experimental conditions. Each chemical synthesis route differs from the other, indicating diverse synthesis environments and

chemicals involved in each method. These methods are mainly used to prepare the 1D and 2D nanostructures such as nanoflakes, nanotubes, nanorods, nanoparticles, etc., that are difficult to be structured by top-down approaches. These methods have superior controllability with high reproducibility. Various chemical synthesis methods have also been examined in thermoelectrics and have proved successful in synthesizing nanostructures in inorganic TE materials such as Bi_2Te_3, chalcogenides, etc. The current figure of merit of these methods is in the range 1–1.2 (ZT = 1.18 at 500 K for $Bi_2Te_{2.5}Se_{0.5}$ [17]) and provides better mechanical properties with good characterization and scalability up to 20 g. However, these chemical methods are moderately developed, and the synthesis of heterostructures is still not achieved. The development reached now has come a long way in enhancing the TE performance. The thermal conductivities and Seebeck coefficient have been notably optimized, whereas the electrical conductivities are still on the lower side due to the influence of grain boundaries and insufficient contact. Enhancing electrical conductivities to build high-quality bulk samples or films with various nanostructures and implementing them on a large scale is the most challenging step for these chemical methods. The advance of robust synthetic routes, optimized bulk sample preparation, precise micro-processing techniques, etc., would provide the attention these chemical methods deserve in the TE industry for wide-ranging applications.

The powder metallurgy process involves mixing alloy or elemental powders, compaction, sintering, and finishing. Several powder metallurgical processes such as gas atomization and cryogenic grinding provide good scalability with efficient thermoelectric properties. These methods produce high-quality powders with high scalability (up to 3–5 kg/min). Gas atomization methods have superiority in terms of scalability, whereas cryogenic grinding is better in terms of thermoelectric

performance (1.55 at 825 K for Yb single-filled $CoSb_3$ [18]). These methods have efficient material utilization, design of complex shapes, good surface finishing, energy-efficient, environmentally friendly, and most suitable for producing quantities in large quantities. These are not well-known methods due to limitations in variability and the high initial cost of powder, even with these exceptional benefits. These methods are extensively used in the automobile industry.

Conventional TEG fabrication methods involve electrically connecting the diced pellets with metal electrodes fashioned as a sandwich in two ceramic plates. These methods involve expensive equipment, high temperatures, and are not particularly suitable for flexible electronics applications. Several printing fabrication methods, such as inkjet printing, screen printing, dispenser printing, and photonic sintering, are utilized primarily for wearable and portable electronic applications. These methods are used for organic, inorganic, and hybrid organic-inorganic TE materials. They are simple, easy, quick, durable, and do not require complex post-processing. Printable methods also have the advantage of low-cost equipment, low-temperature, low-material wastage, vacuum-less fabrication, and high reproducibility. Compared to other techniques available for large-scale synthesis, these methods are still in their infancy and have low conversion efficiencies and figure of merit values (between 0 and 1). Some challenges faced in these methods are non-uniform deposition, low-resolution, and rough surface of the substrates. Even with the fast and extensive research, there is still a long way ahead for these methods before being employed in large-scale practical environments. Detailed evolution of the different large-scale, cost-effective, environment-friendly synthesis and fabrication methods are discussed in the next section. Table 2-2 gives a summary of the current progress made in different large-scale fabrication techniques.

Table 2-1. Summary of recent progress in prominent large-scale synthesis methods.

Technology	Materials	Processing Cost	Time	Scalability (Max Weight/ Batch)	Ztmax (Material-Ref)	Strengths	Drawbacks
Microwave-assisted hydrothermal/solvothermal	Inorganic (Bi_2S_3, SnTe, α-MgAgSb,etc) nanostructures	Medium	Moderate	≈10 g	2.2 (SnSe [15])	Lower operating temperatures, minimum material loss, good dispersion, and eco-friendliness, highly crystalline nanostructures	Inability to observe and monitor the reaction process
Chemical synthesis	Inorganic (Bi_2Te_3, Copper-based)	Low	Moderate	≈20 g	1.2 ($Bi_2Te_{2.5}Se_{0.5}$ [17])	Simple, inexpensive, better mechanical properties, better characterization	Controlling the parameters of deposition is difficult to achieve
Gas Atomization	Inorganic	Low	Ultra-fast	3–5 Kg/min	≈1 (Bi_2Te_3+ 75% Sb_2Te_3 [19])	High-quality pure powders, high powder flow rates, economical, very high scalability	Powder properties vary with the equipment from different suppliers
Cryogenic grinding	Inorganic, hybrid	High	Fast	High	1.5 (Yb single-filled $CoSb_3$ [18])	Fine sintered powders, improved mechanical abilities, power saver, no oxidation	Formation of ice around the delivery nozzle and piping system blocks delivery of liquid nitrogen

Table 2-2. Summary of recent progress in prominent large-scale fabrication techniques.

Technology	Materials	Processing Cost	Time	Scalability (Max Weight Per Batch)	Ztmax (Material-Ref)	Strengths	Drawbacks
Inkjet printing	Organic, hybrid organic-inorganic	Low	Medium	High	0.26 (Bi_2Te_3 [20])	High quality, fine, and smooth printing. Power source in wearable and portable electronics	Nozzle clogging, nozzle plate flooding, and erratic droplet ejection
Screen printing	Organic, hybrid organic-inorganic	Low	Fast	High	≈1($Bi_{0.5}Sb_{1.5}Te_3$ [21])	Printable on diverse substrates, durable and high quality	Relatively complex and less eco-friendly
Dispenser Printing	Organic, hybrid organic-inorganic	Low	Medium	Medium	0.41 (Sb_2Te_3-epoxy [22])	Higher contact resistance, simple, easy, and do not have post-processing requirements	Slow dispensing and difficulty in reproducibility
Photonic sintering	Inorganic (Bismuth-based)	Low	Fast	High	-	Higher conductivities, shorter processing times, better adhesion, flexibility	The intense light pulses lead to increased energy consumption

CHAPTER 3: EXPERIMENTAL MATERIALS AND METHODS

3.1 Introduction:

Chapter 1 explained the basics of the thermoelectric concept along with the classifications of thermoelectric materials based on their operating temperatures. The second chapter provides a comprehensive theory and literature review of thermoelectric materials. The current chapter outlines all the materials, consolidation methods, and sintering methods used in this thesis work. The different characterization techniques used to study the thermoelectric material's structural, electrical, thermal, dielectric, and mechanical responses have also been summarized.

3.2 Raw materials:

Chalcogenides are promising thermoelectric materials that consist of one or more elements from the chalcogen family (S, Se, Te). Chalcogenides due to their unconventional bonding mechanism are superior thermoelectric materials compared to the other traditional semiconductor TE materials. Bismuth telluride (both p-type and n-type- NS6130-12-000436A) and p-type copper selenide (purity: 99.995%, APS:100 µm, Stock no: NS6130–12–000158) powders were obtained from Nanoshel LLC and used without any purification. The p-type ($Bi_{0.5}Sb_{1.5}Te_3$) and n-type ($Bi_{1.894}In_{0.106}S_{0.11}Te_{2.89}$) bismuth telluride powders consisted of antimony and indium sulfide doping, respectively. The p-type copper selenide powder was an intrinsic semiconductor with a pure single phase of $Cu_{1.83}Se$ and no external doping. The commercial powders obtained from Nanoshel LLC are given in Figure 3-1.

Figure 3-1. Commercially obtained bismuth telluride and copper selenide powders from Nanoshel.

3.2.1 Bismuth telluride:

Bismuth telluride (Bi_2Te_3) is the first and best thermoelectric material to be developed for refrigeration and cooling purposes due to its immense capability of converting waste heat to beneficial electrical energy [30]. Bi_2Te_3 is basically a compound element of Bi (Bismuth) and Te (Tellurium) [31]. The behavior of bismuth physically is of metal but alloyed with tellurium, and it functions as a semiconductor TE material [32]. Bi_2Te_3 operates in the low to intermediate temperature range [33]. The crystal structure of bismuth telluride is shown in Figure 3-2 (a).

3.2.2 Copper selenide:

Copper selenide is a prominent I-IV semiconductor with a p-type conduction mechanism along with a direct and indirect transition bandgap of 2.79 eV and 1.36 eV, respectively [34]. Copper selenide is an intermediate temperature TE material and a superionic conductor with extraordinary ZT values (>1.5), and its liquid-like behavior of copper ions (Cu^+) promotes exceptional thermal properties aligning itself with the properties of the "Phonon-liquid electron crystal (PLEC)" effect [35]. These

properties have promoted copper selenide in various applications, including photovoltaic (PV) energy harvesting and thermoelectric. Excellent optical characteristics supported by vastly tunable localized surface plasmon resonance (LSPR) promote copper selenide as an excellent photodetector in the solar field [36]. This, combined with the superlative thermoelectric properties, proves copper selenide to be an ideal low-cost and sustainable material for hybrid solar thermal cell design. Copper selenide (Cu_2Se) exists in both non-stoichiometric ($Cu_{2-x}Se$) and stoichiometric compositions with various crystallographic forms, for instance, monoclinic, cubic, tetragonal, and orthorhombic configurations [37]. The crystal structure of copper selenide (Cu_2Se) at low temperature is monoclinic (α-phase) with the transformation of structure to face-centered cubic, i.e., β-phase in case the temperature exceeds 137 ^oC or 410 K. The liquid-like behavior of the copper ions around the selenium sub-lattice has boosted the TE performance of Cu_2Se, especially at high temperatures. The crystal structure of copper selenide is shown in Figure 3-2 (b).

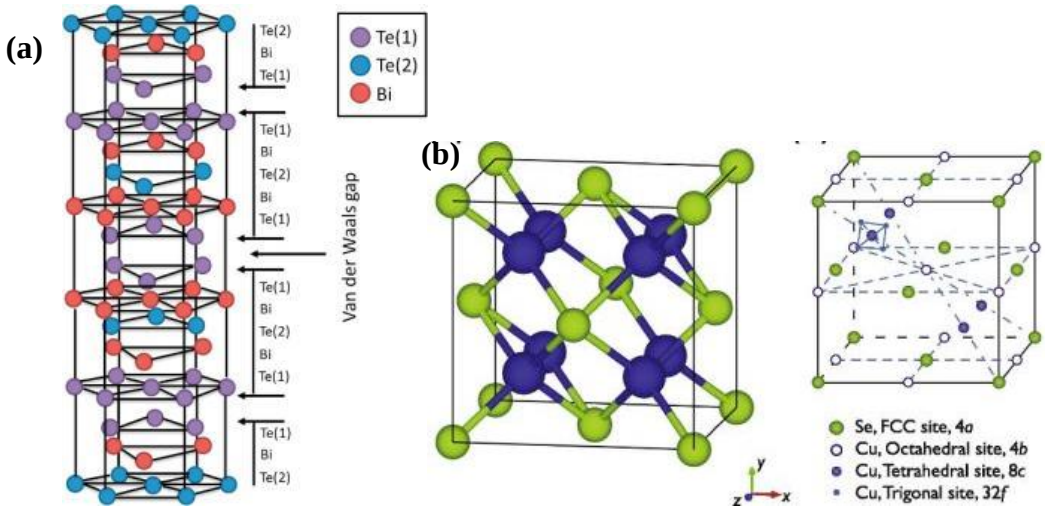

Figure 3-2. Crystal structure of (a) bismuth telluride [38], and (b) β-copper selenide [39].

3.3 Consolidation methods:

Consolidation or compaction of material powders results in a significant enhancement in material quality in terms of the microstructure and phase composition. We have used cold compaction to consolidate both p-type and n-type bismuth telluride powders and hot press to compact copper selenide samples.

3.3.1 Cold compaction:

Cold compaction is a technique in which granular materials are mechanically densified by cold pressing to make them cohesive. The commercially obtained p-type and n-type bismuth telluride powders were compacted at an applied pressure of 6 MPa for 30 s by cold uniaxial pressing to make circular pellets of weight 3.5 g and 5 g. The Archimedes principle was employed to calculate the densities of our sample. The non-sintered cold compacted sample was found to have a density of 5.92 gm/cm3 (76.88 %). The samples have densities in the range of 6.1-6.5 gm/cm3 after annealing, which is around 79.22-84.44 % of the ideal densities of bismuth telluride. The porosities of the samples were computed using the formula $\phi = \frac{\rho_0 - \rho}{\rho_0} * 100$ %, where ρ_0 is the theoretical density of the measured samples and ρ is the density of the tested samples. The porosities ranged from 15.5 % to 23.12 %. The principles and setup of cold compaction are illustrated in Figure 3-3.

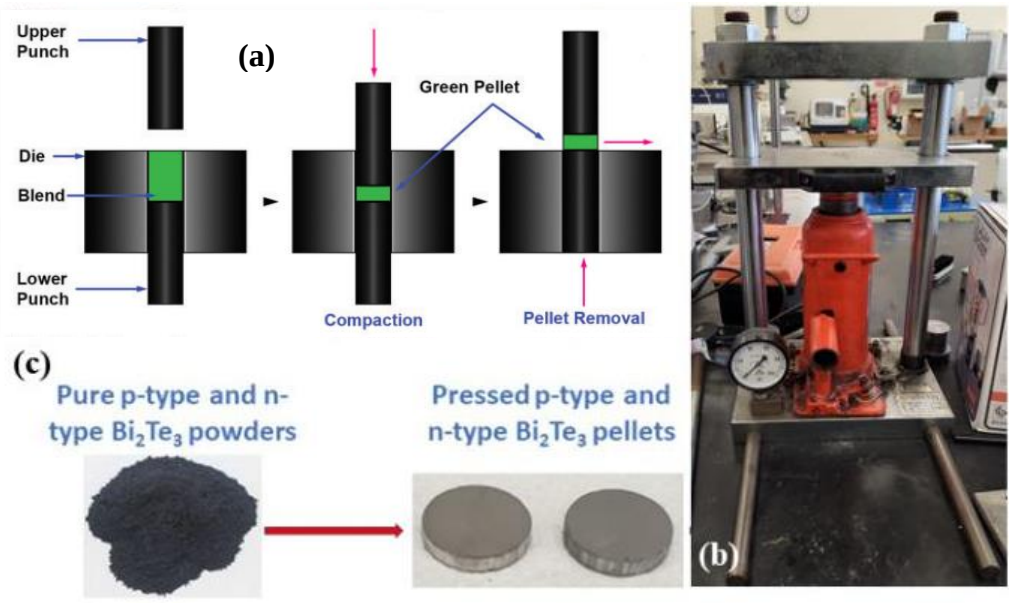

Figure 3-3. (a) Cold compaction process [40], (b) cold uniaxial pressing equipment, (c) cold compacted p-type and n-type bismuth telluride pellets.

3.3.2 Hot pressing:

Cold pressing has some drawbacks, including poor density and difficulties compacting hard powders. As a result, a hot-pressing (HP) technique for densifying materials with poor sintering behavior has been devised. In HP, applying pressure and high temperature at the same time can speed up the process of densification, resulting in a fine-grained and pore-free compact (Figure 3-3 (a)). In the case of p-type copper selenide powder, cold compaction up to a pressure of 50 MPa was unsuccessful in consolidating due to the liquid-like behavior of the copper in the commercial samples as shown in Figure 3-3 (b). Different pellets of weight 1.5 grams and 3.5 grams were made by the hot press (Carver, Model No. 4368, USA) at 250 ^{o}C temperature and a pressure of 350 MPa. The pellet made from hot pressing is shown in Figure 3-3 (c). The 3.5 grams identical pellets were designed to measure the thermal conductivities of the samples. The diameter of all the pellets was 13 mm, and the thickness of 1.5 grams and 3.5 grams pellets were 2.58 mm and 5.3 mm, respectively. We have used

Archimedes' method to calculate the sample densities. The density of the hot-pressed sample was found to be 5.112 gm/cm^3 (75.36%). The volumetric densities of the annealed samples by this method were found to be in the range of 5.2-5.5 gm/cm^3 which is about 76-81 % of the theoretical densities of copper selenide. The principles and setup of hot pressing are illustrated in Figure 3-4.

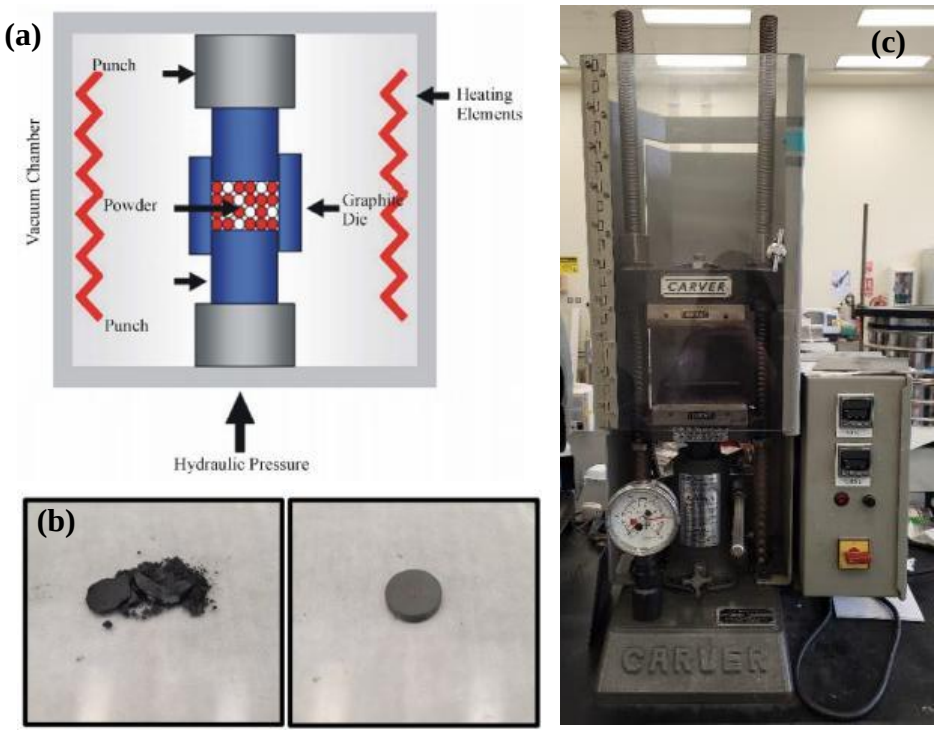

Figure 3-4. (a) Schematic representation of hot pressing, (b) copper selenide pellet formation cold compaction (left) and hot pressing (right), and (c) hot pressing equipment (Carver 4368).

3.4 Sintering methods:

3.4.1 Conventional or Box sintering:

Conventional or pressure-less sintering is the simplest sintering form that involves heating of the ambient temperature prepared powder compact without any applied external pressure [41]. The specimen is heated using heating devices such as silicon rods in conventional heating. Convection, conduction, or radiation are used to

transport heat to the specimen. This poses the critical problem of non-uniform heating, which causes temperature gradients in the material, resulting in internal tensions. The principle and the Nabertherm Muffle furnace used in this work are shown in Figure 3-5.

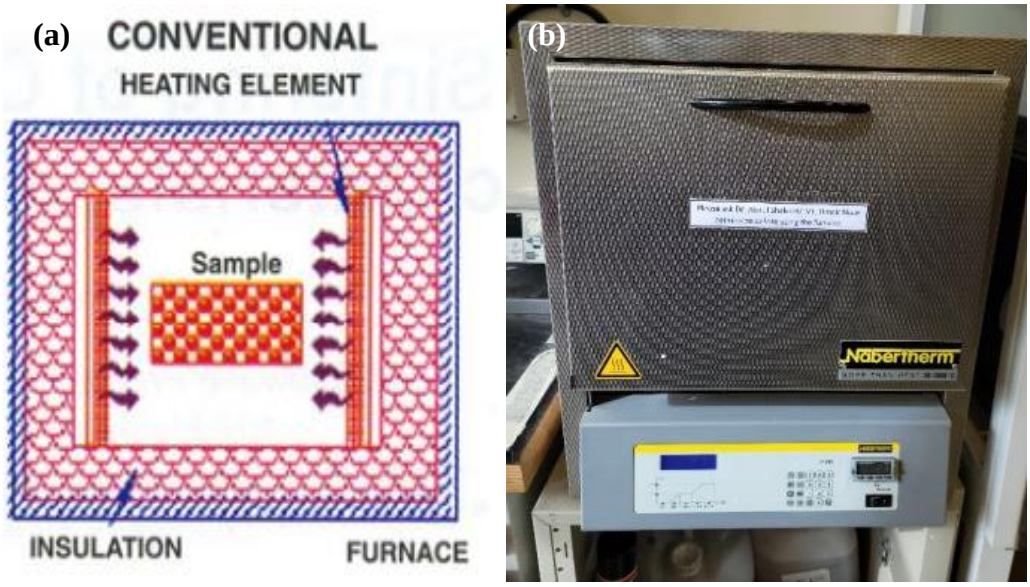

Figure 3-5. (a) Illustration of conventional sintering [42], (b) Box furnace equipment.

3.4.2 Microwave sintering:

The microwave annealing uses the electromagnetic field of the microwave to heat inside the materials at the atomic level through interaction between material and microwaves. In microwave sintering, the heat is generated internally, whereas, in conventional sintering, the heating occurs from around the edges of the material [43]. The advantage of microwave annealing over traditional sintering methods is mainly the capability to produce unique, uniform, and high-quality microstructures and nanostructures by transfer of energy by microwaves uniformly throughout the volume of the target material [44]. In this research, the microwave-assisted bidirectional rapid sintering method provided by (VB ceramic furnace, VBCC/MF/1600 ◦C/14/15, Chennai, India) was used in this work as shown in Figure 3-6.

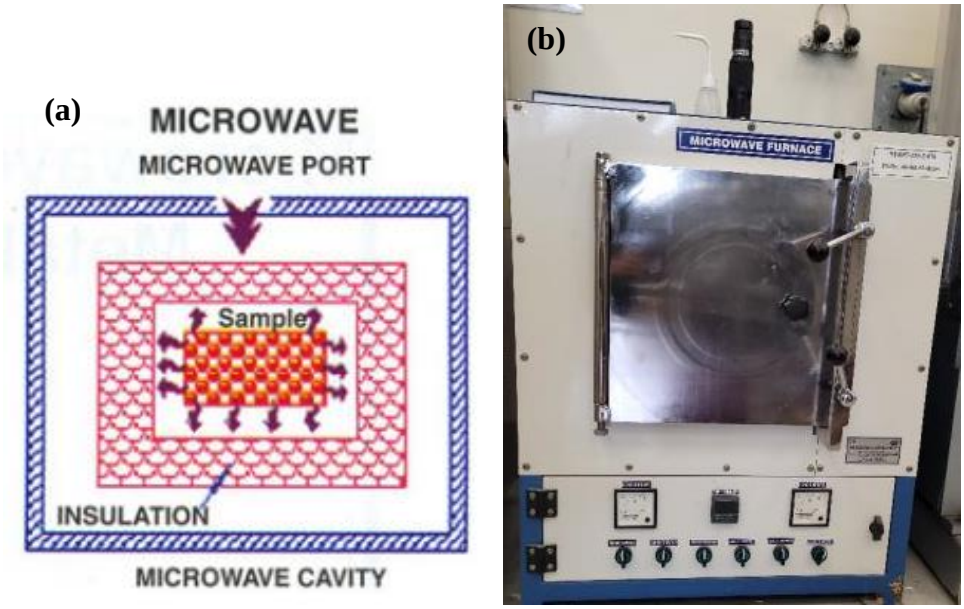

Figure 3-6. Illustration of microwave sintering [42], (b) equipment of microwave sintering.

3.4.3 Tube sintering:

The material samples are heated in presence of argon gas in the tube sintering. The presence of argon gas reduces any kind of impurities in the samples during the sintering process and has reduced oxidation concentration when compared to the conventional sintering process. The schematic of a typical tube furnace is shown in Figure 3-7.

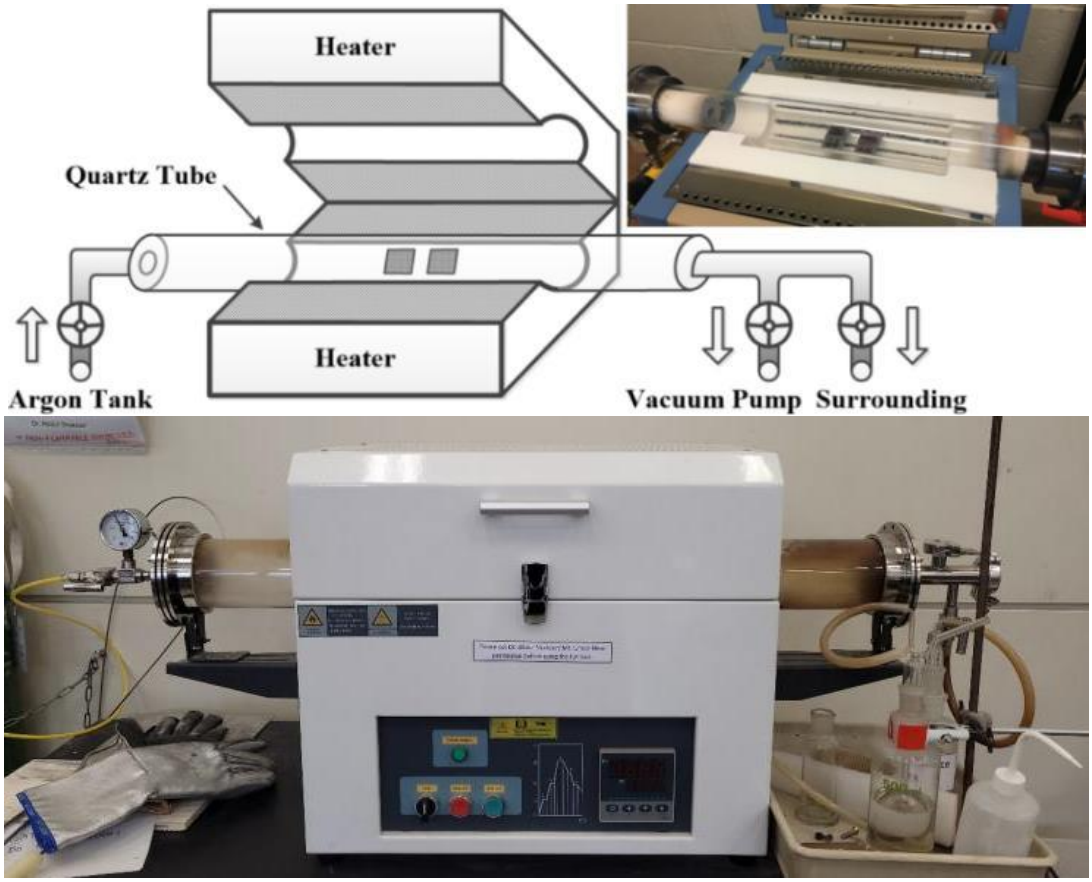

Figure 3-7. Schematic of tube furnace or tube sintering [45], (b) tube sintering equipment.

Table 3-3. Sintering conditions for bismuth telluride and copper selenide preparation.

Sample	Compaction type	Sintering method	Sintering temperature range	Ramp heating rate
p-type bismuth telluride	Cold compaction	1. Conventional sintering 2. Microwave sintering 3. Tube sintering	250 ºC-400 ºC	10 ºC/min
n-type bismuth telluride	Cold compaction	1. Conventional sintering 2. Microwave sintering 3. Tube sintering	250 ºC-400 ºC	10 ºC/min
p-type copper selenide	Hot pressing	Microwave	250 ºC-725 ºC	10 ºC/min

3.5 Characterization techniques:

3.5.1 X-ray diffraction (XRD) analysis:

The characterization technique of X-ray diffraction analysis is used to examine the physical and chemical characteristics of materials. It is utilized to realize a material's crystallography, which comprises crystal structure, crystal orientation, and indicating the various phases within the crystalline structure. The influence of changing content in the composition of polycrystalline materials on grain boundaries and average grain size may also be seen via X-ray diffraction analysis. The XRD patterns were documented using a PANalytical EMPYREAN, Netherland (45 kV/40 mA) with CuKα1 (λ = 1.540598 Å) and CuKα2 (λ = 1.544426 Å) radiation across the range of 2θ between 10º and 90º. The grain size was approximated through the Debye-Scherrer formula [46],

$$D = \frac{k \,.\, \lambda}{\beta . cs\theta}$$

where D is the crystallite size in nm, k is the shape factor (0.93), λ is the wavelength of X-ray and in this case, CuKα (1.54 nm), β is the FWHM (full width half maximum) of the intense peak in radians, and θ is the Braggs angle. The data for the XRD analysis were acquired in the 2θ range from 10º to 90º. The setup of X-ray powder diffraction analysis used in this research is shown in Figure 3-8.

Figure 3-8. X-ray powder diffraction analysis setup at CAM.

3.5.2 Scanning electron microscopy (SEM) and Energy dispersive X-ray (EDX) analysis:

Field emission scanning electron microscopy (FESEM) and energy dispersive X-ray (EDX) analysis were used to evaluate the chemical composition and morphological changes of elements in the specimen, as well as the detection of oxide concentrations, using a Nova Nano Scanning Electron Microscopy with Bruker EDX Detector (Model: Nova Nano SEM 450, Manufacturer: FEI, Netherland). SEM is used to examine the surface microstructures of the material samples. SEM creates pictures and gives high-resolution images by focusing a high-energy electron beam on the surface of materials. This helps comprehend the surface's shape. Surface morphology is studied using SEM on a variety of specimens for use in the characterization of the sensors. SEM has the ability to magnify objects up to 200,000 times.

The X-ray technique Energy Dispersive X-Ray Analysis (EDX), often known as EDS or EDAX, is used to determine the elemental composition of the specimen. The imaging capacity of the microscope detects the specimen of interest in EDX systems, which are attachments to Electron Microscopy equipment (Scanning Electron Microscopy (SEM) or Transmission Electron Microscopy (TEM)). EDX analysis

produces spectra with peaks corresponding to the elements that make up the real composition of the material under investigation. Image analysis and element mapping of a sample are additional options. The setup used for SEM analysis is shown in Figure 3-9.

Figure 3-9. SEM analysis setup at CLU.

3.5.3 Transmittance electron microscopy (TEM):

The transmission electron microscopy (TEM) images were attained by TECNAI G2 TEM, TF20 (FEI). In electron microscopy, TEM is a critical tool for characterizing nanoparticles. The pictures of nanoparticles obtained by TEM have a spatial resolution equivalent to that of the atomic level. The electron beam from which the incoming light is emitted into a thin foil electrode is turned into elastically or

inelastically dispersed electrons when it interacts with the specimen. The lens is said to magnify the ratio of the distance between the objective lens, the specimen, and the image plane. To identify the crystal structure, shape, and size of nanomaterials, high TEM resolution is required. The setup used for TEM analysis is shown in Figure 3-10.

Figure 3-10. TEM analysis setup at CLU.

3.5.4 Four-point probe method:

The DC electrical resistivities and conductivities were measured using the Ossila four-point probe system with the assistance of the Ossila sheet resistance v1.0.01 software. The four-point probe is the most popular piece of equipment for determining a material's resistance. The lateral resistance through a thin square of conducting/semiconducting material is represented by sheet resistance, which is the resistivity of a material divided by its thickness. Four probes are organized in a line with identical spacing between them for this measurement. A current is transmitted between the outer and inner probes, resulting in a voltage drop between them. The sheet resistance may then be estimated by monitoring the voltage change. The Ossila

four-point probe system is shown in Figure 3-11.

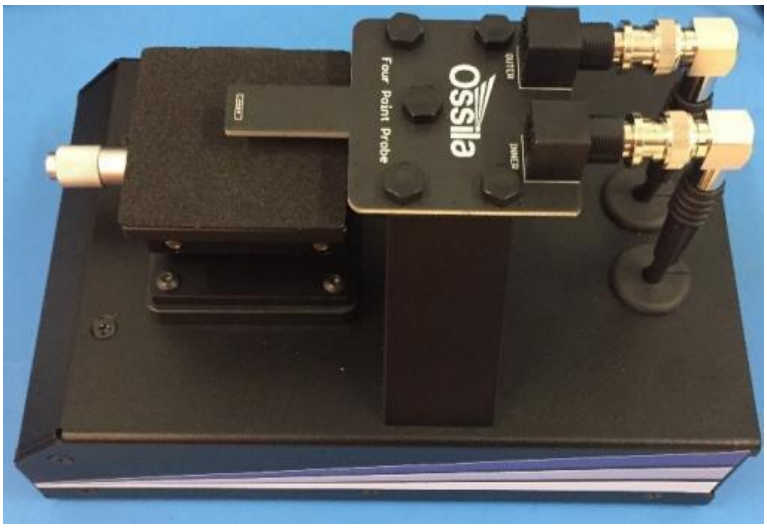

Figure 3-11. Four-point probe system for electrical conductivity.

3.5.5 Thermal constants analysis (TCA):

The thermal characteristics such as thermal conductivity, specific heat capacity, and thermal diffusivity were determined by thermal constants analyzer (TCA) test using the TPS 2500s hot disk analyzer. Thermal conductivity is measured using the Hot Disk Thermal Constants Analyzer. A source meter, a high sensitivity resistance sensor and a computing unit make up the system. Two identical samples are sandwiched between layers of Kapton film on either side of an electrically conducting wire pattern in the shape of a double spiral. A steady electric current is then used to heat the sensor for a brief period of time. The heat evaporates into the surrounding material, lowering the sensor's temperature, which is detected by the equipment. After that, the computer unit analyzes the data and calculates the thermal conductivity, thermal diffusivity, and specific heat capacity of the samples. The thermal constants analyzer setup is given in Figure 3-12.

Figure 3-12. Hot Disk Thermal Constants Analyzer at CAM.

3.5.6 Thermal Gravimetric analysis (TGA):

A Perkin-Elmer TGA is used for TGA analysis (4000). The mass loss of the sample material with temperature is measured using TGA. In the crucible or aluminum oxide pan, a powder sample of the thermoelectric material with a weight of 10 mg is placed. There is no requirement for reference material because TGA only has one furnace. The sample has no cover, allowing gases to escape into the environment, and the gases are prevented from escaping into the environment directly by a sucker system. The sample material's room temperature (30 °C) is elevated at a rate of 20 °C/min from room temperature to 600 °C. At a rate of 19 ml/min, nitrogen gas is injected. The setup used for TGA analysis is shown in Figure 3-13.

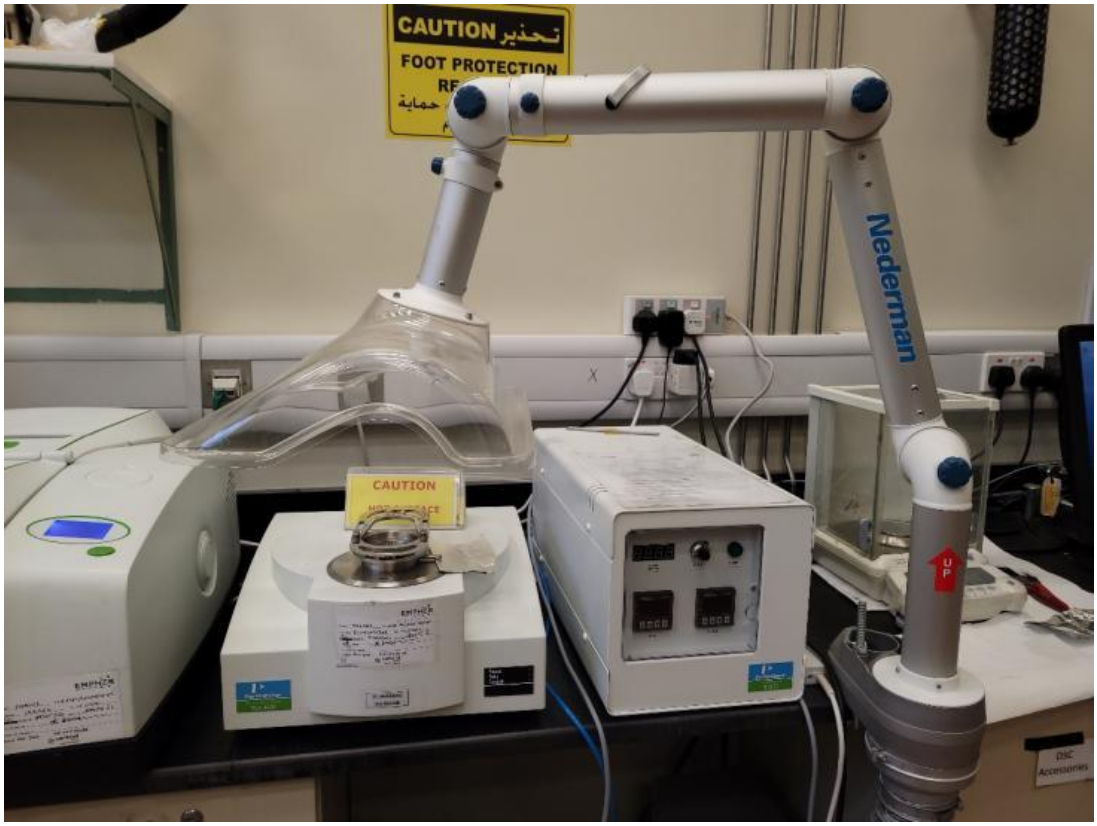

Figure 3-13. Thermal Gravimetric analysis setup at CAM.

3.5.7 Differential scanning calorimeter (DSC):

A Perkin-Elmer DSC (8500) apparatus was used to perform differential scanning calorimetry measurements in a nitrogen atmosphere. DSC (8500) is made up of two crucibles, one of which holds the sample material and is put in a temperature-controlled furnace. The reference material is placed in the empty second crucible; both crucibles are constructed of aluminum. The samples are tested at temperatures ranging from 30 °C to 700 °C. The sample is heated with nitrogen gas in the furnace, which eliminates air from the furnace, at a preset heating rate of 10 °C/min. To examine both crystallization processes, the temperature is reduced from 700 °C to 30 °C after reaching the melting point. The information obtained from DSC analysis is utilized to better understand material thermal stability and thermal degradation of the thermoelectric materials across a wider temperature range. The setup used for DSC analysis is shown in Figure 3-14.

Figure 3-14. Differential scanning calorimeter setup at CLU.

3.5.8 Nanoindentation test:

Nanoindentation is a standard method applied to determine the nanomechanical properties of the materials. nanoindentation test involves applying and releasing a load from a sample using a geometrically well-defined probe in a very controlled manner. The transducer applies a force during the nanoindentation process, and the probe displacement is continually monitored to form a conventional force vs. displacement curve. The resultant force vs. displacement curve assists as the material's 'mechanical fingerprint,' from which quantifiable nanoscale material attributes may be calculated. The quantitative information about the mechanical characteristics of the sample can be obtained by analyzing the observed force vs. displacement curve (especially the unloading section). Hardness (H) and Reduced Modulus (Er) are typical values that are derived from nanoindentation testing. Other data, such as delamination force, stiffness, fracture toughness, and film thickness, can also be collected. The Young's modulus and nano-hardness were measured using a nanoindenter at room temperature (MFP-3D Nano Indenter, Asylum Research,

Oxford, UK). A maximum load of 1 mN at a dwell time of 5s at peak load was applied on the samples. The setup used for the nanoindentation test is shown in Figure 3-15.

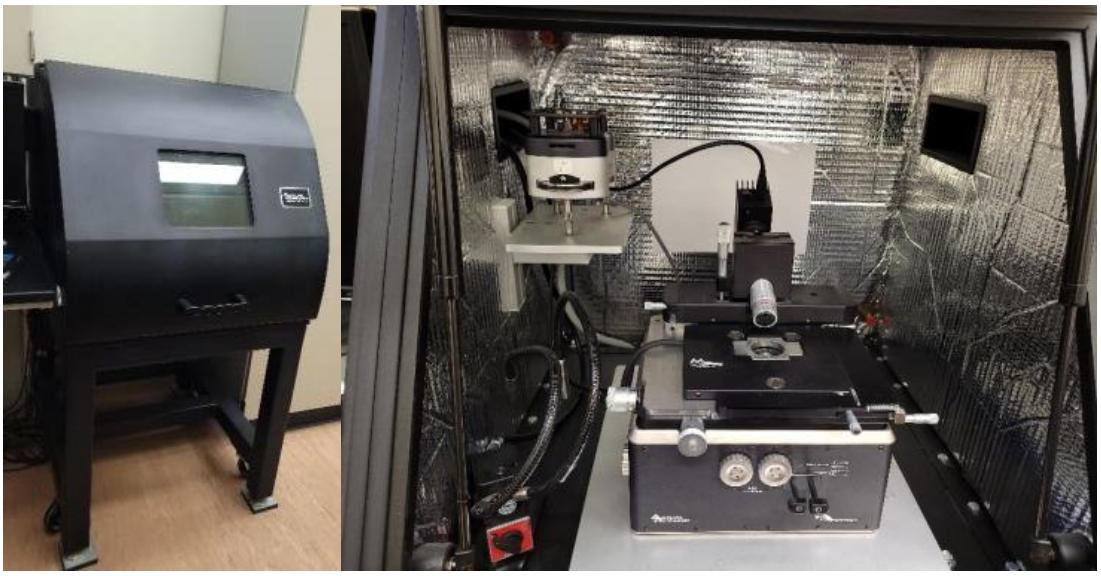

Figure 3-15. Nanoindentation setup at CAM.

3.5.9 Compression test:

Compressive strength test is a mechanical test that determines how much compressive stress a material can withstand before cracking. A progressively applied load compresses the test item, which is commonly in the shape of a cube, prism, or cylinder, between the platens of a compression-testing machine. Compression tests of the samples were examined using an instrument Lloyd, USA-LR50Kplus, Sussex, UK, a universal testing machine under standard conditions of pressure and temperature with a 0.6 mm/min engineering strain rate. The average of four successful iterations was recorded. The universal testing machine (UTM) for the compression test is shown in Figure 3-16.

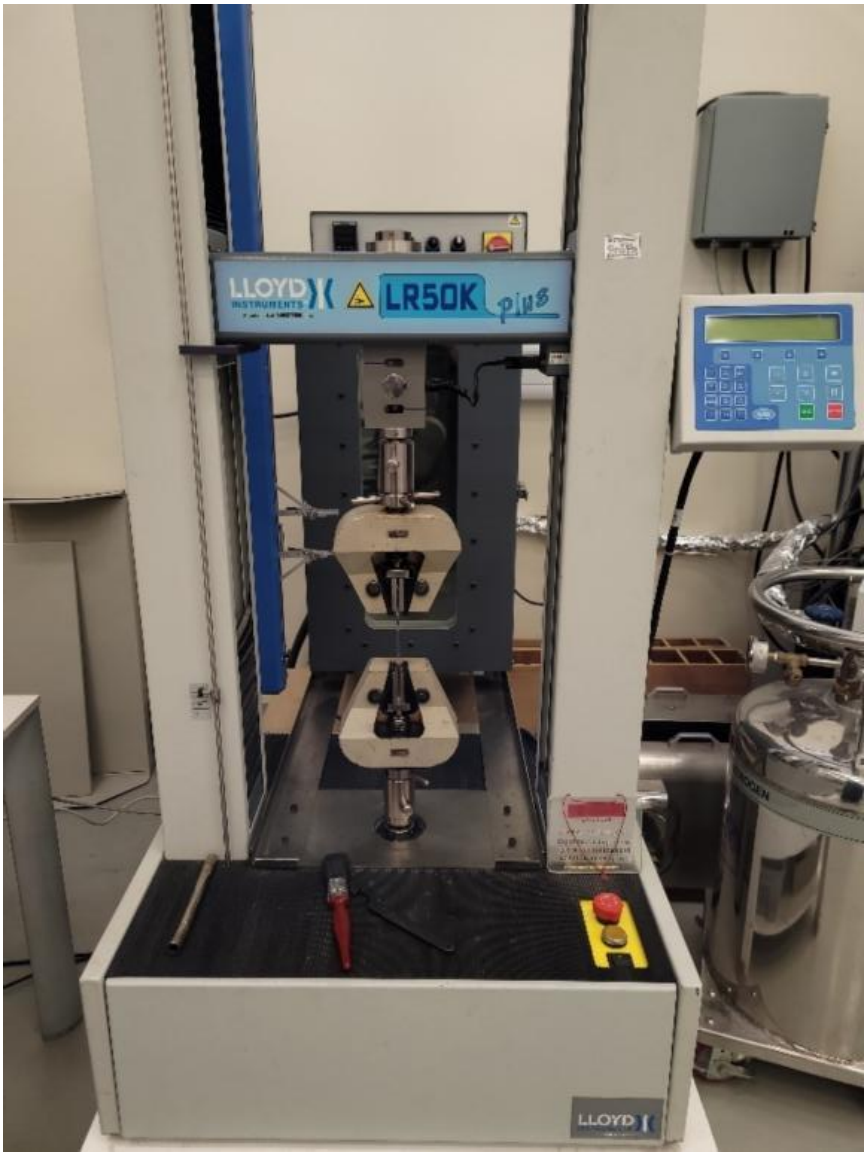

Figure 3-16. Universal testing machine at CAM.

3.5.10 Microhardness test:

When test materials are not acceptable for macro-hardness, microhardness testing is used to determine the resistance or hardness of a material to deformation. Microhardness testing is useful for determining the hardness of extremely small/thin samples, complicated geometries, material phases, and surface coatings/platings. The microhardness of the samples was investigated using a Vickers tester (FM-ARS9000, MKV-h21, Tokyo, Japan). Each specimen was put through five successful iterations under the load of 5 gf and 10 s dwell time to accomplish highly accurate results. The

microhardness setup is shown in Figure 3-17.

Figure 3-17. Microhardness testing setup at CAM.

3.6 Broadband dielectric spectroscopy (BDS):

Electrical parameters such as AC electrical conductivities, AC capacitance, impedance measurements, dielectric permittivity (both real and imaginary), and loss tangent were assessed using Broadband Dielectric Spectroscopy (BDS). The BDS was accomplished by Novocontrol GmbH Concept 40 broadband dielectric spectrometer. The software used for computing various parameters was Novocontrol Win DETA. The sample's data was recorded at fixed temperatures in the range of 25 ^{o}C to 400 ^{o}C with a 25 ^{o}C temperature increment over a frequency range of 10 mHz–10 MHz. The Broadband dielectric spectroscopy setup is pictured in Figure 3-18.

Figure 3-18. Broadband dielectric spectroscopy setup at CAM.

CHAPTER 4: OPTIMIZATION OF THERMOELECTRIC PROPERTIES OF BISMUTH TELLURIDE

4.1 Introduction:

Chapter 4 deals with the enhancement of electrical, thermal, and mechanical properties of p-type and n-type bismuth telluride thermoelectric materials by optimizing the sintering methods and sintering temperatures. The successful incorporation and feasibility of thermoelectric (TE) materials into high-performance and reliable commercial thermoelectric generator systems require enhancement in electrical, thermal, and mechanical properties. Currently, several TE materials are researched that have comparatively high figure of merit (ZT) values in the low, medium, and high-temperature range applications such as bismuth tellurides, chalcogenides, skutterudites, half-Heusler, silicon germanium, and other complex alloys [47]. Among these materials, bismuth telluride TE materials are popular in the low to intermediate-range materials due to benefits such as high chemical stability from their layered structure favoring low thermal conductivities resulting in high conversion efficiencies [48]. Additionally, these materials can be designed both as p-type and n-type materials [6]. Owing to these unique properties, bismuth telluride alloys find themselves in applications such as heating, refrigeration, and as a power source in radioisotope thermoelectric generators (TEGs) for planetary exploration and deep space missions [33]. Bismuth telluride is a highly investigated material with a well-developed manufacturing approach for module design lowering any technical development risk. Our objective in this work is to study the structural, electrical, dielectric, thermal, and mechanical properties of both p-type and n-type bismuth telluride thermoelectrics.

4.2 Experimental Details:

The materials used to prepare samples are the commercially available p-type and n-type bismuth telluride powders (Bi_2Te_3 -purity:99.99% and size: 200 mesh) supplied by Nanoshel LLC (NS6130-12-000436A). The p-type powders were bismuth telluride doped with antimony, and n-type powders were bismuth telluride with indium sulfide doping. The powders were weighed to be 5 grams each, and then various p-type and n-type pellets were compacted by cold uniaxial pressing under an applied pressure of 6 MPa for 30 seconds. Each pellet prepared was of diameter and width 13 mm and 3 mm, respectively. These samples were then sintered in conventional or box furnace, tube furnace, and microwave-assisted bidirectional rapid sintering method provided by (VB ceramic furnace, VBCC/MF/1600 ◦C/14/15, Chennai, India) at temperatures 250 ^{o}C, 300 ^{o}C, 350 ^{o}C, and 400 ^{o}C. In the tube furnace, the sintering is done in the presence of argon gas flow. In all the cases, the heating ramp time is considered as 10 ^{o}C/min. At each temperature, the samples were sintered for 1 h and left to be cooled down to room temperature and then removed from their respective chambers. We have used the Archimedes principle to estimate the densities of our sample. The density of the non-sintered cold compacted sample was found to be 5.92 gm/cm^3 (76.88%). Post annealing, the densities of the samples were in the range of 6.1-6.5 gm/cm^3 which is about 79.22-84.44% of the theoretical densities of bismuth telluride. The porosities of the samples were calculated using the formula $\phi = \frac{\rho_0 - \rho}{\rho_0} * 100\%$, where ρ is the theoretical density of the measured samples and ρ_0 is the absolute density of bismuth telluride. The porosities were in the range of 15.5%-23.12%. The sintered samples were then investigated for structural, microscopic, electric, and thermal properties.

****Nomenclature:**

BPXXX: p-type samples sintered in the box furnace at temperature XXX ^{o}C.

MPXXX: p-type samples sintered in the microwave furnace at temperature XXX ^{o}C.

TPXXX: p-type samples sintered in the tube furnace at temperature XXX ^{o}C.

BNXXX: n-type samples sintered in the box furnace at temperature XXX ^{o}C.

MNXXX: n-type samples sintered in the microwave furnace at temperature XXX ^{o}C.

TNXXX: n-type samples sintered in the tube furnace at temperature XXX ^{o}C.

4.3 Structural properties:

Figure 4-1 shows the XRD profile of all the samples treated through the microwave sintering method at different temperatures. To study, analyze and compare the structural behavior, bonding, and impurity phase changes of Bi_2Te_3 at different sintering temperatures, powder X-ray diffraction data were collected from 26 Bi_2Te_3 samples using Cu-Kα radiation. Out of the 26 samples, two were pristine p-type and n-type samples, and others were sintered samples at temperatures 250 ^{o}C, 300 ^{o}C, 350 ^{o}C, and 400 ^{o}C in the box, microwave, and tube furnace, respectively. The XRD analysis data were collected in the 2θ range from 10° to 90°. Bragg's peaks and fitted profile for all the samples are shown in Figure 4-1. The grain size calculations of the different sample XRD profiles are given in Appendix A. The grain size was approximated through the Debye-Scherrer formula [49],

$$D = \frac{k\lambda}{\beta . \cos\theta}$$

Where D is the crystallite size in nm, k is the shape factor (0.93), λ is the wavelength of X-ray and in this case, CuKα (1.54 nm), β is the FWHM (full width half maximum) of the intense peak in radians, and θ is the Braggs angle.

The pure p-type samples consisted of a pure single phase of antimony bismuth telluride ($Bi_{0.5}Sb_{1.5}Te_3$) with hexagonal structure as confirmed by ICDD: 98-061-7062

data whereas the n-type samples comprised of a pure single phase of bismuth indium sulfide telluride ($Bi_{1.894}In_{0.106}S_{0.11}Te_{2.89}$) with hexagonal structure as confirmed by ICDD: 98-065-8770 data. Doping bismuth telluride with antimony made the p-type material and doping bismuth telluride with indium sulfide made n-type samples.

For the p-type samples in conventional sintering, the pristine and BP250 showed sharp peaks indicating high crystalline nature. Peak broadening can be observed at 2θ=27.6 with (0 1 5) plane in BP300 and BP350 samples, and this may be due to descent in size of the crystallite with the increase in sintering temperature up to 350^{o}C. But in the sample BP400, as shown in figure S1(b) (Appendix A), peak shifts can be observed due to the introduction of the oxidized impure phase of $Bi_1O_4Sb_1$ as confirmed by ICDD:98-007-5901. There have also been changes in peak position and intensities above 350^{o}C temperatures. On the contrary, in the case of n-type Bi_2Te_3, the peaks and phases are similar for pristine, BN250, and BN300 samples. But whereas for the samples BN350 and BN400, there are various new peaks at different 2θ indicated by several impure phases such as $Bi_2O_5Te_1$, $Bi_2O_7Te_2$, and $Bi_2O_{11}Te_4$ as seen in Figure S1(c) (Appendix A) that can be confirmed by ICDD:98-028-0627, 98-008-5725 and 98-007-2709. It is also noteworthy that as the sintering temperature increased, there has been an exponential increase in the various oxide phases. To summarize, it can be said that the p-type samples are pure single-phase and crystalline until sintering temperature 350 ^{o}C and have an oxide impure phase at temperatures beyond it. On the other hand, in the n-type samples, the impure phases have been introduced at a lower sintering temperature of 350 ^{o}C. The estimated grain size (from Appendix A) indicates that the crystallite size decreased as the sintering temperature increased. It can be vividly deduced that the size of the sub-microns depends on the sintering temperature. The size of the sub-microns ranges from 400 nm to 1000 nm.

In the microwave furnace, the p-type samples have an almost similar XRD profile for all the samples, as shown in Figure 4-1(a). There has been a slight increase in intensities and some broadening at some peaks with some negligible shifts in the phases. Also, oxidations phases are from low to null in the p-type samples. On the contrary, in the n-type material, the profile is similar for pristine, MN250, and MN300 samples with pure single phases whereas, there are some considerable amounts of impure bismuth oxide phase of $Bi_2O_5Te_1$ in MN400 as depicted in Figure 4-1(b) and confirmed by ICDD:98-028-0627. Overall, the p-type material in the microwave furnace has been stable and did not change any phase through temperatures 250 ^oC to 300 ^oC and had some antimony oxide (O_3Sb_2) impurity in samples MP350 and MP400 as confirmed by ICDD:98-000-1994. In the n-type samples, there were considerable phase changes at sintering temperatures 350 ^oC and 400 ^oC. In the tube furnace, the p-type materials have no peak shift for pristine, TP250, and TP300 samples. But for the TP350 and TP400 samples, there are several new oxidized impurity peaks, such as $Bi_2S_{0.15}Te_{2.85}$ and O_3Sb_2 confirmed by ICDD:98-061-7047, as shown in figure S1(d) (Appendix A). For the n-type, the impure phases are similar to that observed in the box and microwave furnaces.

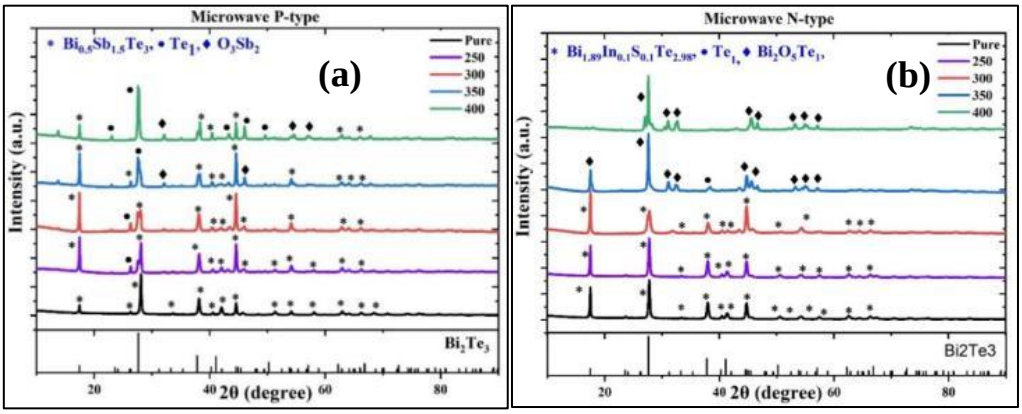

Figure 4-1. XRD profile of (a) microwave sintered p-type Bi_2Te_3, and (b) microwave n-type Bi_2Te_3.

4.4 SEM:

4.4.1 P-type:

The Scanning Electron Microscopic (SEM) images of both non-sintered and sintered p-type bismuth telluride samples are shown in Figure 2(a)-(d). The dependence of crystallization on sintering temperature is illustrated in these images. Figure 4-2(a) represents the SEM image of the non-sintered p-type sample. It can be seen in Figure 4-2(a) that the non-sintered samples had a layered structure with tellurium-rich phases. The thickness of each layer is in the range of ~10 nm. Figure 4-2(b)-(d) indicates the crystallization process in the microwave furnace. The SEM images illustrating the crystallization process in conventional and tube furnaces are given in Appendix A. It can be seen at 250 ^{o}C sintering temperature in the box and microwave furnace, the morphology and size were quite similar to the pristine p-type sample with an addition of a few small ununiform micro-sized crystals. But in tube sintering, several micro-sized crystals were observed between the layers at 250 ^{o}C sintering temperature. Subsequently, the samples contained a mixture of nanocrystals and microcrystals (namely fine grains and coarse grains, respectively). The size of the sub-microns kept on decreasing with an increase in sintering temperatures in all the sintering methods. That means with temperature increase, better and uniform finer grains were formed. This can be confirmed by the grain size calculated from XRD characterization data using the Debye-Scherrer formula given in Appendix A. At sintering temperatures 300 ^{o}C and 350 ^{o}C in all the furnaces, the sub-microns were finer and uniformly distributed with sizes ranging between 500-900 nm, as shown in Figure 4-2.

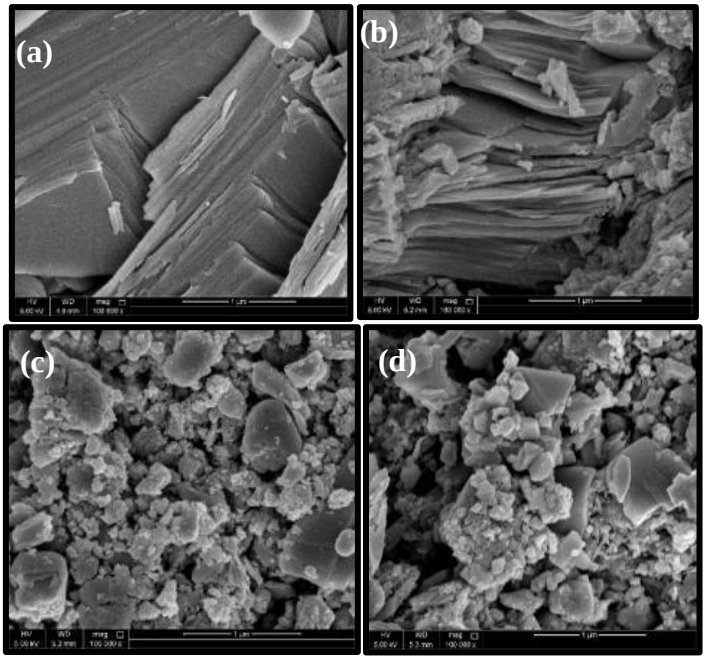

Figure 4-2**.** Field emission scanning electron microscopy (FESEM) images at 1µm of (a) pristine p-type Bi_2Te_3 sample, (b) MP250. (c) MP300, (d) MP350. Sub-microns of sizes less than 1 µm can be observed in the SEM images of samples sintered at 300 ^oC and 350 ^oC.

4.4.2 N-type:

The Scanning Electron Microscopic (SEM) images of the n-type bismuth telluride samples both with and without sintering are shown in Figure 4-3(a)-(d). The images indicate how crystallization occurs in different sintering at different temperatures. Figure 4-3(a) represents the SEM image of the pristine n-type sample. It can be seen in Figure 4-3(a), the pure sample had a layered structure with bismuth-rich phases. Figure 4-3(b)-(d) indicates the crystallization process in the microwave furnace. The crystallization process in the conventional and tube furnace is given in Appendix A. In p-type samples, the formation of micro-nano-sized crystals started roughly around 300 ^oC. But here, in the case of n-type samples, the crystallization started at a lower sintering temperature of 250 ^oC in all the sintering. At sintering temperatures, 250 ^oC and 300 ^oC, the size and morphology of the samples consisted of uneven and

ununiform micro-sized crystals. In the box furnace at 250 ^{o}C, some layered structures can be observed. The SEM images also indicate that the samples consisted of both fine and coarse grains. Finer and finer particles were formed with an increase in sintering temperature. The size of the sub-microns for the n-type samples ranges from 400-700 nm, as shown in Figure 4-3.

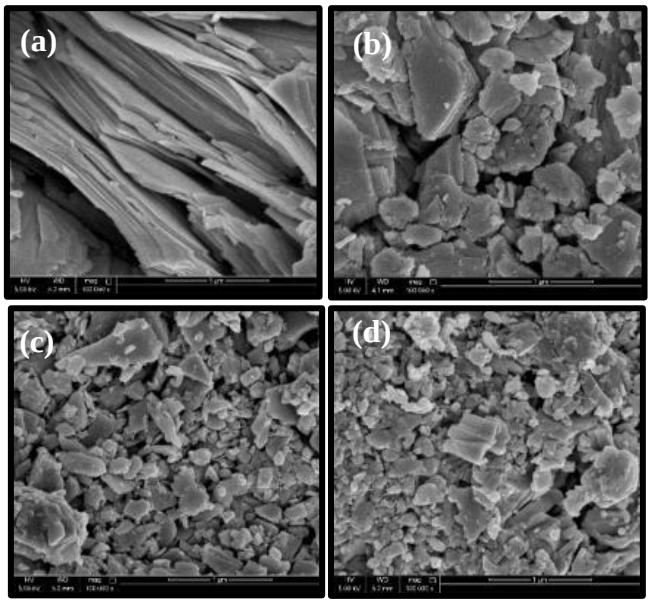

Figure 4-3**.** Field emission scanning electron microscopy (FESEM) images at 1µm of (a) Pristine n-type Bi_2Te_3 sample, (b) MN250. (c) MN300, (d) MN350. Sub-microns of sizes less than 1 µm can be observed in the SEM images of samples sintered at 300 ^{o}C and 350 ^{o}C.

4.5 TEM:

The TEM images were examined since the SEM images are not sufficient in defining the grain size. The TEM images of the pristine p-type and n-type samples are shown in Figure 4-4(b)-(d) and Figure 4-5(b)-(d), respectively. The low and moderate magnification images are depicted in Figure 1(b) and (d), respectively. The p-type ($Bi_{0.5}Sb_{1.5}Te_3$) nanoparticles have a hexagonal lattice (space group: R-3m) with lattice parameters of a = 4.300 Å and c = 30.470 as confirmed by ICDD: 98–061–7062 data from the XRD (given in Appendix A). The TEM images reveal that the size of

agglomerated particles is in the range of 100-200 nm and is verified by the selected area electron diffraction (SAED) as demonstrated in the inset of Figure 4-4(b) and the size is comparatively smaller than depicted in the SEM images of Figure 4-4(a). However, the inter-planar spacing of~ 0.310-0.321 nm corresponding Bi_2Te_3:hkl-indices of 015 are shown in Figure 4-4(c), S12(c), and S13(c). The HRTEM image shown in Figure 4-4(c) further illustrates that the smaller grains of approximately 5-10 nm compose the larger grains in Figure 4-4(a). This same explanation can be given to the pristine n-type samples except with the grains at a much smaller size (50 nm-100 nm) than the p-type samples. Similarly, the n-type ($Bi_{1.894}In_{0.106}S_{0.11}Te_{2.89}$) nanoparticles have a hexagonal lattice (space group: R-3m) with lattice parameters of a = 4.3500 Å and c = 30.3200 as confirmed by ICDD: 98–065–8770 data (given in Appendix A). However, the inter-planar spacing of~ 0.310-0.320 nm corresponding Bi_2Te_3:hkl-indices of 015 are shown in Figure 4-5(c), S14(c), and S15(c). The SEM, TEM, SAED, and HRTEM images of MP250, MP300, MN250, and MN300 are given in Appendix A (Figure S12-S15). These ultra-fine grains might have a significant role in enhanced thermal and mechanical stability.

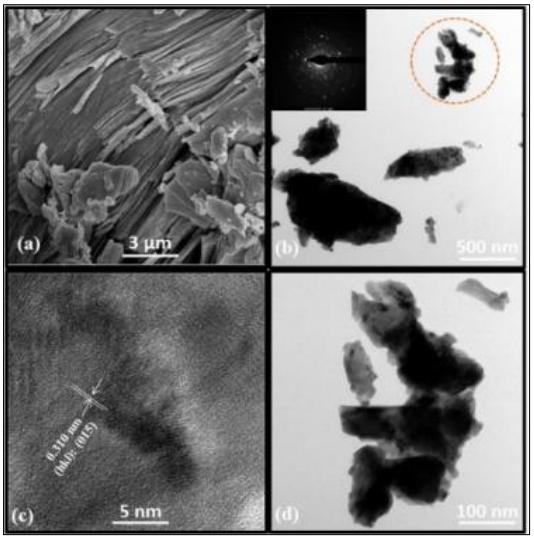

Figure 4-4**.** (a) Scanning electron microscopy (SEM) image of the p-type Bi_2Te_3 pellet at 3 µm, (b) low magnification transmission electron microscopy (TEM) image with

SAED pattern (selected area electron diffraction) shown in the inset of the p-type Bi_2Te_3 pellet at 500 nm resolution, (c) High-resolution TEM (HRTEM) image of p-type Bi_2Te_3 pellet at 5 nm, (d) Zoom in TEM image at 100 nm resolution.

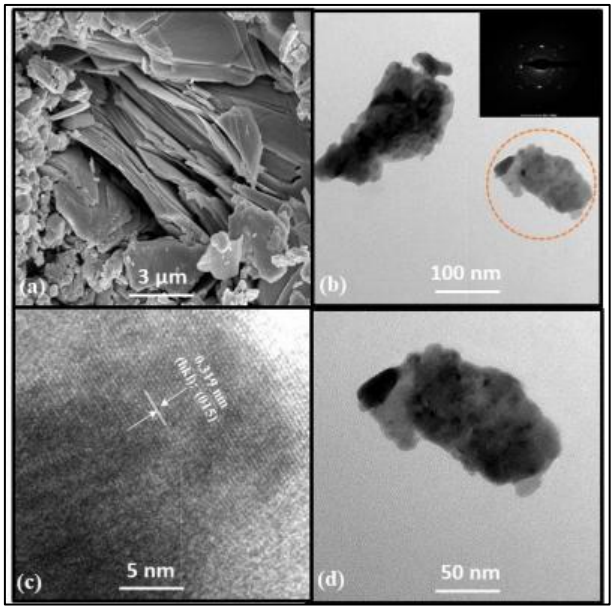

Figure 4-5. (a) Scanning electron microscopy (SEM) image of the n-type Bi_2Te_3 pellet at 3 µm, (b) low magnification transmission electron microscopy (TEM) image with SAED pattern (selected area electron diffraction) shown in the inset of the n-type Bi_2Te_3 pellet at 100 nm resolution, (c) High-resolution TEM (HRTEM) image of n-type Bi_2Te_3 pellet at 5 nm, (d) Zoom in TEM image at 50 nm resolution.

4.6 DC Electrical Conductivity:

The DC electrical conductivity of the pristine and the sintered samples were calibrated by Ossila four-point probe system. The software used was Ossila sheet resistance v1.0.01. The equipment applies direct current on the samples, and respective DC sheet resistances are measured. The DC conductivities of all the samples are given in Figure 4-6. The p-type samples after sintering have become better conductors than the n-type samples with maximum conductivity values of 140 S/m and 47 S/m for p-type and n-type, respectively. For both p-type and n-type samples and all three types of sintering, the conductivities are higher at sintering temperatures 250 ^oC and 300 ^oC. The

electrical conductivities have drastically reduced to the range of 2-20 S/m for samples at temperatures 350 ^{o}C and 400 ^{o}C. The impurity in the samples sintered at 250 ^{o}C and 300 ^{o}C have no or negligible impurity concentration leading to high electrical conductivity values of 140 S/m. And for the samples sintered at 350 ^{o}C and 400 ^{o}C, the electrical conductivities were mostly from the bismuth oxide phases resulting in low values of 10 S/m. These oxide phases have restricted the free movement of electrons in the crystal of the samples [50, 51]. Besides, the conductivities are higher for microwave and tube furnace-sintered samples due to lesser impurity concentration and oxidation in the chambers of the microwave and the presence of argon gas in the tube furnace.

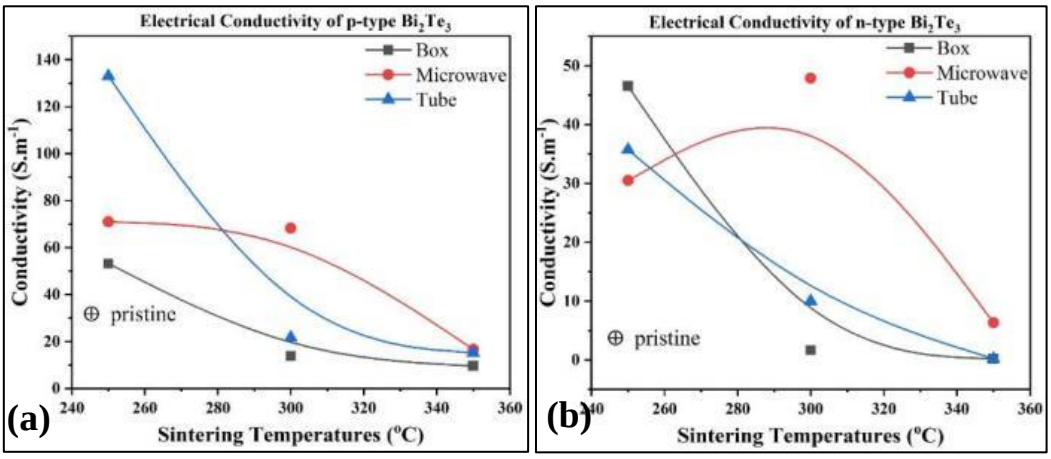

Figure 4-6**.** The variation of DC electrical conductivities of (a) p-type and (b) n-type bismuth telluride samples in different furnaces at different sintering temperatures.

4.7 Thermal characteristics:

4.7.1 Thermal constants analysis (TCA):

Two identical samples were prepared at each sintering temperature in the three furnaces, namely box, microwave, and tube. These samples were then tested for their thermal properties such as thermal conductivity, specific heat capacity, and thermal diffusivity by the Thermal constants analyzer (TCA) device. Figure 4-7 depicts how the thermal conductivity of p-type and n-type varies with the sintering temperatures.

The thermal conductivities for the p-type samples are in the range 0.5-1.1 W/m/K, whereas, for the n-type, they are in the range 0.4-0.7 W/m/K. It is to be observed that the thermal conductivities are lower for n-type than p-type. The thermal conductivities are linearly proportional to the sintering temperatures. The samples sintered at 250 ^{o}C and 300 ^{o}C have very low conductivities compared to samples sintered at 350 ^{o}C and 400 ^{o}C. The samples sintered in the box furnace have relatively high thermal conductivities of 1.1 W/m/K when compared to samples in other furnaces. The oxides of bismuth have very high thermal conductivities [52]. This is probably why the samples have high thermal conductivities at higher sintering temperatures (formation of oxide phases shown in the XRD data), especially in the box furnace.

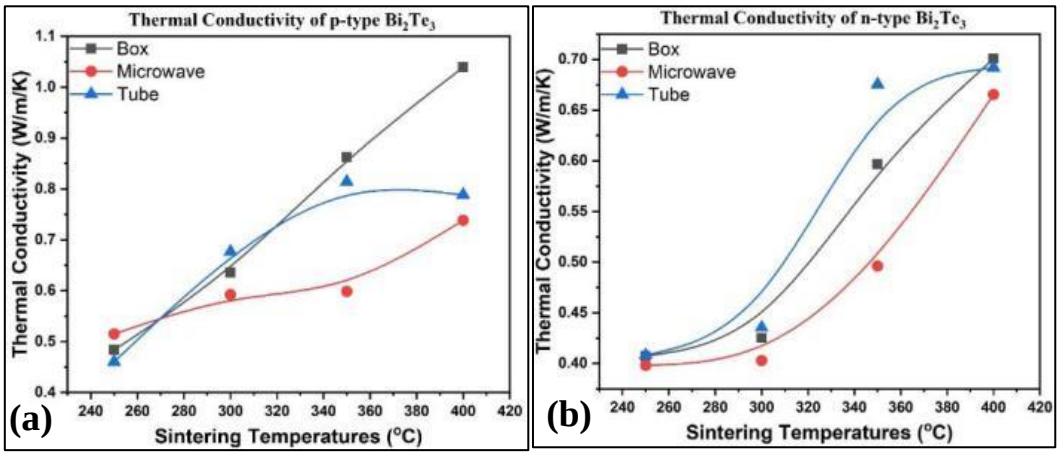

Figure 4-7**.** The variation of thermal conductivities of (a) p-type and (b) n-type Bismuth telluride samples at different sintering temperatures.

4.7.2 Thermogravimetric analysis (TGA) and Differential scanning calorimetric (DSC):

Figure 4-8(a) and (b) illustrate the variation of weight % of p-type and n-type bismuth telluride samples when heating the specimens until 800 ^{o}C. In the p-type, there is no weight loss until 350 ^{o}C indicating high thermal stability of the samples in this temperature range. This trend is observed in both MP250 and MP300 samples. Beginning at approximately 350 ^{o}C, the images indicate a relatively sharp weight

gain. This may be due to some chemical reaction in the specimens due to the environment taking place. The volatility of tellurium at temperatures beyond 350 ^{o}C might have led to the formation of oxides of antimony in p-type samples and bismuth in the n-type samples resulting increase in weight percentage which is consistent with the findings in the previous work [53]. This oxidation saturates at around 550 ^{o}C and from then there is a drastic decrease in mass till 700 ^{o}C due to evaporation of the residues. The n-type samples demonstrated similar behavior except with a lower weight loss of around 5%. The reason for this is that the p-type samples had excess Te phases than the bismuth oxide phases leading to a higher weight loss of 30%. Conversely, the n-type samples had fewer Te phases with a majority of bismuth oxides that have a melting point of around 817^{o}C. The MN250 and MN300 samples had a negligible difference in their weight loss profile. Differential scanning calorimetry is used to analyze phase transition or the crystallization/melting behavior, the specific heat, oxidative stability, polymorphism, solid-solid transitions, purity determinations, degree of crystallinity, or thermokinetics of different methods. DSC results from Figure 4-8(c) and (d) indicate one small endothermic sharp peak around 230 ^{o}C that is close to the melting point of bismuth (271.4 ^{o}C) and another large endothermic sharp peak at 420 ^{o}C that is close to the melting point of tellurium (449.5 ^{o}C) and aligns with structural transformation during the heating procedure. This same reaction is observed in both p-type and n-type samples and pure and sintered samples except with a variation in magnitudes of heat flow. A good degree of crystallinity is observed from the high sharpness of these two endothermic peaks that can be confirmed from the SEM and TEM images in the Appendix. The absence of any other peaks, on the other hand, indicates insufficient phase separation and negligible nanograin growth during the heating cycle of TE specimens in high-temperature

ranges (30-400 ^{o}C) beyond their operating temperature ranges (150 ^{o}C), which provides an added advantage of safety in operation [54]. With a little variation, the onset temperature of the crystallization process is closer to the onset temperatures of melting in the heating cycles [55].

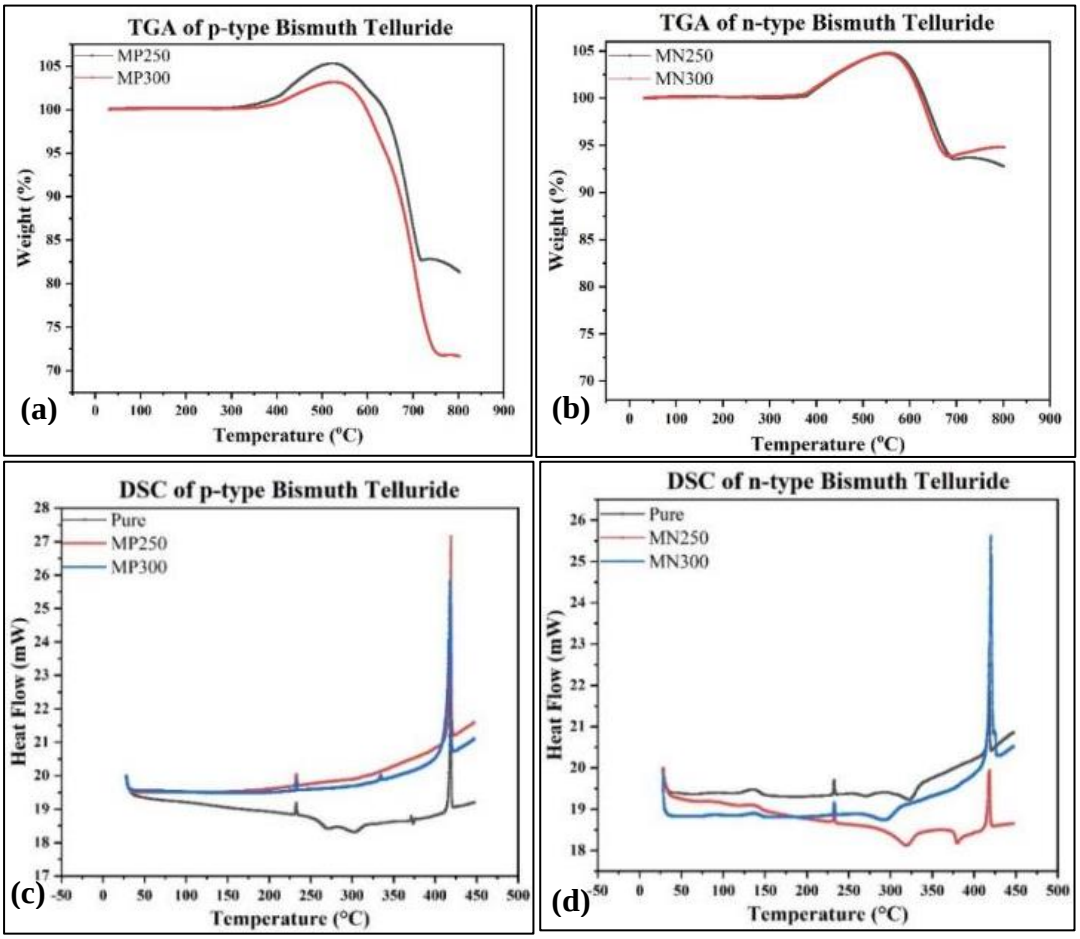

Figure 4-8**.** TGA weight loss curves of (a) p-type Bi_2Te_3, and (b) n-type Bi_2Te_3. DSC analysis curves of (c) p-type Bi_2Te_3, and (d) n-type Bi_2Te_3 (Here pure represents the pristine sample curves).

4.8 Mechanical characteristics:

4.8.1 Nanoindentation:

The load-nanoindentation curves of the p-type and n-type samples are given in Figure 4-9(a). The loading and unloading curves are marked in the image. It can be observed that the indentation depth increases with the increase in sintering temperature from 250 ^{o}C to 300 ^{o}C indicating a reduction in hardness of the samples as the temperature

increases. This trend is more dominant in the p-type rather than the n-type samples. This also can be validated from the Youngs modulus and hardness of the samples as illustrated in Figure 4-9(b). The samples sintered over 300 ^{o}C almost completely oxidized and became exceedingly brittle and fragile as a result. Due to this oxidation, the samples were unsuitable for thermal and mechanical stability testing. There is a drastic decrease in the nanohardness and Young's modulus in the samples sintered at 300 ^{o}C, particularly in the p-type samples. This behavior can be attributed to the fact that high annealing temperatures had a negative influence on the mechanical properties of the pressed pellets. The high temperatures have made the samples brittle and exposed to even lighter amounts of loads. The highest value of nanohardness and Young's modulus is demonstrated by the MP250 sample of approximately 1.4 GPa and 5 GPa respectively, indicating that at 250 ^{o}C annealing temperature, the p-type had better mechanical stability. However, at 300 ^{o}C temperature this quality was in converse and MN300 had nanohardness and Young's modulus of 350 MPa and 2.5 GPa, respectively which is better than that of MP300 (320 MPa and 2 GPa). This decrease in hardness with an increase in annealing temperatures is consistent with previous literature [56]. Porosity typically has a detrimental impact on the mechanical characteristics of a material [57]. Our porous samples, on the other hand, have significantly improved thermoelectric and mechanical characteristics due to their unique microstructure, which includes strongly connected equiaxed grains and evenly dispersed pores (with a porosity of ca. 0.15-0.23). Grain refining aids in the improvement of mechanical characteristics. Furthermore, the equiaxed grain structures in our samples provide isotropic deformation behavior and inhibit fracture development, which contributes to strengthening (Figure 4-10, and Figure 4-11). As a result, the improved mechanical characteristics of our porous samples may be

attributed to the combined impact of grain refining, firmly bonded quasi-equiaxed grains (for increasing), and the insertion of pores (for weakening). Furthermore, the porous samples exhibit outstanding thermal stability and mechanical qualities as a result of their robust internal structure [58].

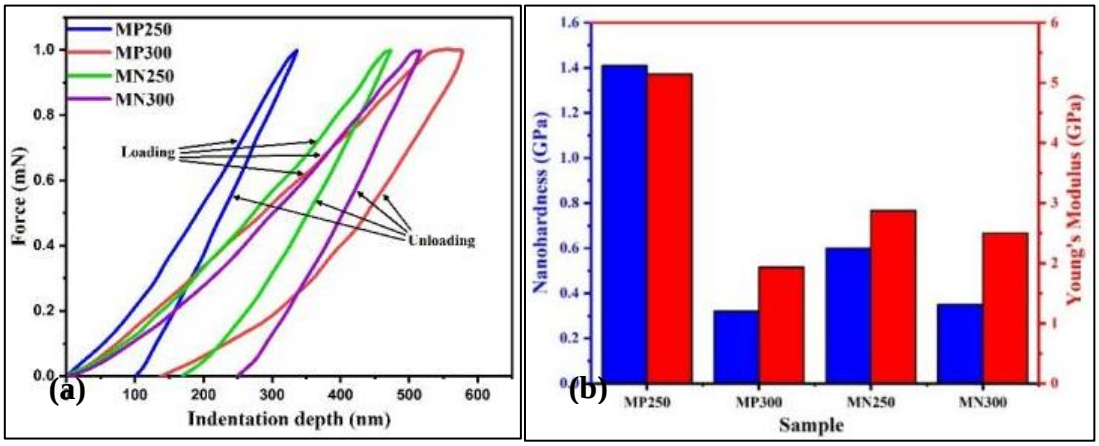

Figure 4-9**.** (a) Load-nanoindentation depth curves, and (b) Young's modulus and nanohardness of p-type and n-type bismuth telluride samples.

4.8.2 Compression test:

Figure 4-10 represents the typical stress-strain curve of the compression test of microwave sintered bismuth telluride p-type and n-type samples. The engineering stress-strain curve of the p-type and n-type specimens are given in Figure 4-10(a) and (b) respectively. The corresponding compressive strength and stiffness values of the samples are illustrated in Figure 4-10(c). It can be noticed that the compressive strengths of both p-type and n-type samples remained unchanged with variations in annealing temperatures. The stress-strain curves depicted, illustrate a typical brittle fracture nature with a compressive strength around 64 ± 0.5MPa. The compressive strength of single-crystal bismuth telluride is low due to the weak van der Waals force. For example, bismuth telluride grown using zone melting or selective laser melting or gas atomization has compressive strength less than 50 MPa in case of sample orientation perpendicular to the building direction [19] [59]. A large number

of disordered sub-micron particles might have strengthened the mechanical properties on a macroscopic level. This might be the reason for the increase in compressive strength of the microwave-sintered samples. The stiffness of the compound is decreased from around 8000 N/mm to less than 6000 N/mm with a change in sintering temperature from 250 ^{o}C to 300 ^{o}C indicating a decline in elasticity of the material at higher annealing temperatures. Even though the material has retained its compressive strength, it has lost its elasticity through sintering temperature variation. However, in all the cases, the shear stress drops suddenly at different points of strain and then gradually increases to the maximum stress point suggesting a significant structural rearrangement at those strain points. Similar curve nature was documented in the mechanical properties study of SnSe [60].

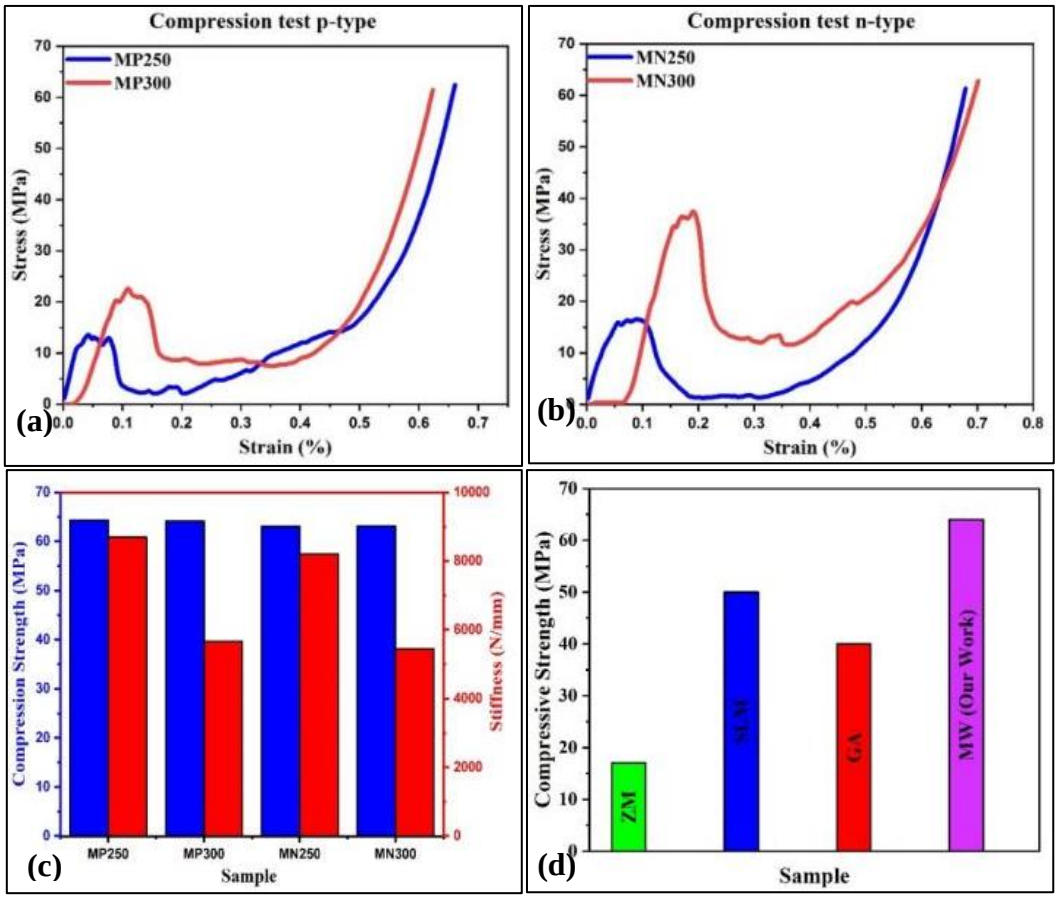

Figure 4-10**.** Engineering stress-strain curve of (a) p-type, and (b) n-type bismuth telluride samples under compressive loading, (c) Compressive strength and stiffness

values of the samples, (d) Comparison of compressive strength of microwave (MW) sintered p-type and n-type bismuth telluride with compressive strength of bismuth telluride prepared by zone melting (ZM) [19], selective laser melting (SLM) [19] and gas atomization (GA at 380 ^{o}C) [59].

4.8.3 Microhardness:

A comparison of Vickers hardness (HV) or microhardness of MP250, MP300, MN250, and MN300 are depicted in Figure 4-11. Similar to the results of the nanohardness test, the HV values are slightly better for samples sintered at 250 ^{o}C in both p-type and n-type Bi_2Te_3. This reduction in hardness in samples with 300 ^{o}C annealing temperature corresponds to the existence of impure oxide phases from the non-vacuum microwave furnace. The results obtained for all our samples are better than the microhardness values of commercially obtained p-type and n-type bismuth telluride materials (~40 HV [61]) suggesting improvement in hardness of the microwave sintered samples. From the Hall-Petch equation, the decrease in grain size corresponds to an increase in the hardness of the material [62]. The random distribution of the crystals and grain refinement would have contributed to the increase in hardness. These values are less than the microhardness values available in some of the ongoing research literature (60 HV [18] and 58 HV [63]) but the thermal conductivities of those compounds are very much higher than our current work [64] and overshadows the gain provided by the improved Vickers hardness. Low thermal conductivities are essential to fulfill the phonon glass electron crystal effect for high efficient thermoelectrics [65]. Improvement in microhardness should not be achieved by compromising the electric and thermal characteristics of the finish product. To our knowledge, this is the highest Vickers hardness achieved with ultra-low thermal conductivities for bismuth telluride thermoelectrics.

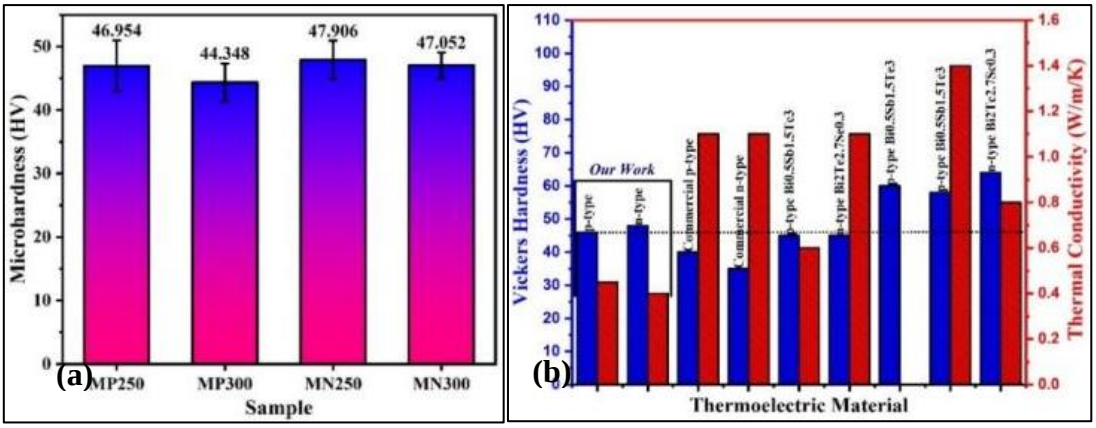

Figure 4-11. (a) Microhardness or Vickers Hardness of p-type and n-type bismuth telluride samples, (b) Comparison of Vickers hardness of our work with other p-type and n-type works from the literature ([64], [61], [66], [67], [18], [63], [68]).

4.9 Broadband dielectric spectroscopy results:

Broadband Dielectric spectroscopy is a powerful means to investigate dielectric material characterization since both the chain motion and conductivity can be monitored with respect to temperature and frequency in the same spectra [69]. It is also sometimes known as impedance spectroscopy and is used to study the physical and chemical properties of the materials and their interactions with electromagnetic radiation. Materials are made of atoms and molecules with electric charges that respond with the application of the electric field. The reactions may be in terms of state transition or rotational motion, ultimately resulting in changes in macroscopic dielectric or electric behaviors in the materials. Gathering, sorting, and examining the dielectric behavior information of the materials is necessary for diverse fields such as material science, electronic chemistry, physical chemistry, and electrical engineering. Thus, using dielectric spectroscopy, we can effectively study the dielectric or electrical properties of thermoelectric materials related to the molecular structure, chemical composition, and phase morphology of the samples.

4.9.1 The variation of AC conductivity with temperature:

Figure 4-12 illustrates the AC electrical conductivities (σ_{ac}) at different frequencies 10 mHz, 1 Hz, 1 kHz, and 1 MHz for p-type and n-type Bi_2Te_3 samples sintered in the box furnace at 300 ^oC. The results show the variation of σ_{ac} with the temperature at different frequencies 10 mHz,1 Hz, 1 kHz, and 1 MHz. The p-type samples demonstrated better σ_{ac} than n-type samples. The p-type samples sintered at 300 ^oC had the maximum electrical conductivity of 1.1 S/cm. The conductivities had a very low or no change until the measuring temperature was 250 ^oC. Beyond 250 ^oC, there has been a sudden spike in the conductivities, probably due to the introduction of defects and improvement in the crystal size in the samples leading to increased carrier concentration and mobility [70]. The charge carriers at high temperatures are highly localized, leading to higher conduction through the hopping mechanism [71]. It also suggests that the pellets became highly conductive above 250 ^oC due to the availability of free majority charge carriers. There is a broad hump from 200 ^oC to 300 ^oC within the frequency range of 1 Hz to 1 MHz; however, the hump specified is rather very small or negligible for 10 mHz. Similar behavior has been previously reported in the case of CuO-doped $SrTiO_3$ [72].

Additionally, the coarse structures of samples sintered at 250 ^oC favor better electron transportation, as there is a decrease in the quantity of grain boundaries due to the formation of micro-sized structures. The movement of electrons is easier in coarse structures all the way through the electrically neutral grain boundaries that enhance the carrier transport in coarse and fine structures, unlike the phonon scattering [73]. However, even though the samples sintered at 350 ^oC and 400 ^oC had finer micro and nanostructures, the oxide impurity phases restricted the free movement of electrons, especially in the n-type samples, which had an abundance of bismuth resulting in a

massive number of distinct bismuth oxide phases [50, 51]. The samples in the microwave furnace and tube furnace had better σ_{ac} than the samples in the box furnace.

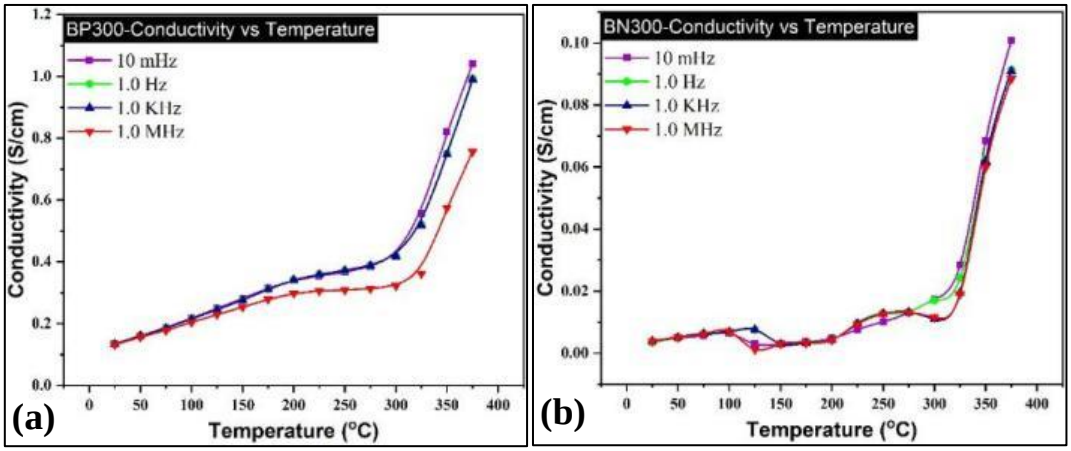

Figure 4-12**.** Temperature dependence of electrical conductivity at frequencies 10 mHz, 1 Hz, 1 KHz, and 1 MHz for (a) p-type and (b) n-type Bi_2Te_3 samples sintered in the box furnace at 300 ^oC. The conductivity increases with an increase in temperature and a sudden spike can be observed in the range 350 ^oC-400 ^oC. Also, the conductivity is high in case the frequency is 10 mHz.

4.9.2 The variation of AC conductivity with frequency:

The variation of AC conductivity with frequency is necessary to analyze the electrical conduction behavior in the bismuth telluride thermoelectrics. The capacitance and parallel conductance measurements were obtained in the spectrometer and Windeta software to calculate the appropriate frequency-dependent values of the AC conductivity σ_{ac}. The total conductivity is the sum of AC and DC conductivities, which is proposed by Jonscher's Universal power-law equation [74] given by

$$\sigma = \sigma_{dc} + A\omega^n$$

Where, σ_{dc} is the DC conductivity, which is frequency independent, A is the AC component or pre-exponential constant and ω is the angular frequency ($2\pi f$) and n is the power-law exponent of the mobile ions and ranges between 0 and 1. The σ_{ac}

complies with the Almond-west universal power law given by $\sigma_{ac} = A\omega^n$ [75]. The variation of AC conductivity through temperatures 25 ^oC to 375 ^oC with frequency f can be seen in Figure 4-13. A typical conductivity vs. frequency spectrum exhibits three distinct regions, namely 1) low frequency dispersion, 2) an intermediate frequency plateau, and 3) an extended dispersion at higher frequencies [69]. The low frequency (10mHz- 1Hz) variation of the conductivities can be attributed to the dielectric polarization in the material [76]. This dielectric effect increases the capacitance in the material, thereby decreasing the AC conductivity that can be seen in the plots of Figure 4-13. In the intermediate frequency range, the conductivity is almost independent of frequency and can be given by the DC conductivity. A sudden increase of the conductivity around 1MHz indicates decreased polarization at higher oscillations in the high-frequency dispersive region. It is also noted that the conductivities increased with an increase in temperatures from 25 ^oC to 375 ^oC, implying the linear relationship of conductivity with temperature. This increase may be ascribed to the generation of multiple oxygen vacancies at higher temperatures and enhancement in the drift mobility of the charge carriers through thermal activation because of the increase in the hopping rate in the conduction mechanism [71]. The samples sintered at 300 ^oC showed a steady independent response to the frequency variations in conductivity. There is a rapid drop in conductivities in the samples at 350 ^oC from the low-frequency region to the intermediate frequency region.

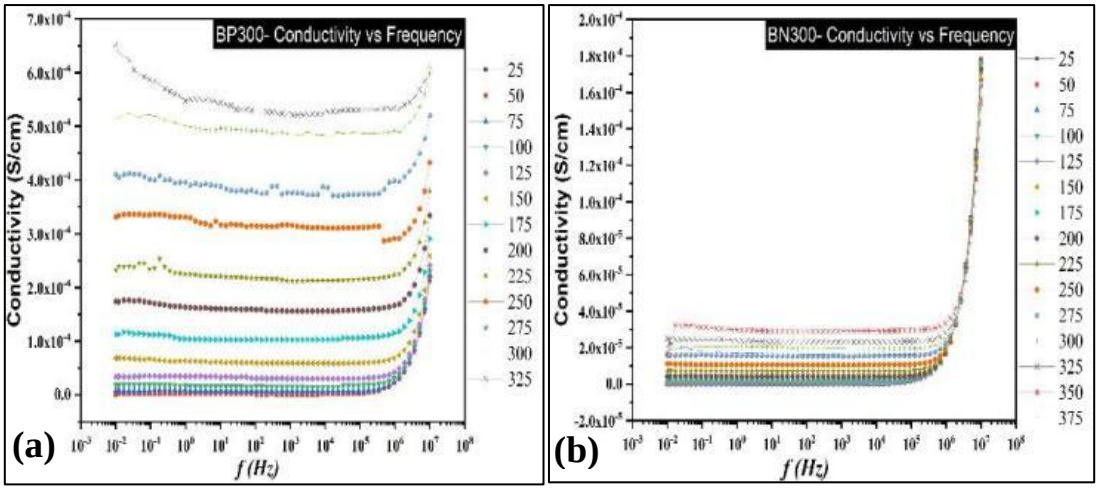

Figure 4-13. Frequency dependence of electrical conductivity in the temperature range 25 ^{o}C to 375 ^{o}C for (a) p-type and (b) n-type Bi_2Te_3 samples sintered in the box furnace at 300^{o}C. The conductivity is high at temperature 375 ^{o}C. A spike in AC conductivity can be observed at higher frequencies.

4.9.3 The variation of dielectric permittivity storage with frequency:

The variation of dielectric permittivity storage of as-prepared and sintered bismuth telluride samples with frequency through temperatures 25 ^{o}C to 375 ^{o}C are depicted in Figure 4-14. The sintering conditions and temperatures influence the physical properties of the sample pellets, which in turn affects their dielectric properties. The electron transport properties are affected, making it an absolute necessity to investigate the influence of temperature and sintering method on the dielectric constant, dielectric loss, and electric modulus of the referenced samples. The frequency-dependent dielectric parameter is termed by the complex form of permittivity given by

$$\varepsilon^* = \varepsilon' - j\varepsilon''$$

Where real part ε' is the relative dielectric permittivity or dielectric permittivity constant or storage and imaginary part $\varepsilon''$is the dielectric loss. The dielectric constant can be calculated from the capacitance C and is given by

$$\varepsilon' = C \times (\frac{d}{A})$$

Where A is the surface area of the sample (πr^2; r is the radius) and d is the thickness of the sample.

The dielectric loss ε''can be calculated from the measured conductance (G) with the following expression:

$$\varepsilon'' = G \times (\frac{d}{\varepsilon_o \omega A})$$

where $\varepsilon_o$is the permittivity in free space.

The plots in Figure 4-14 show that the dielectric storage decreases with increasing frequency. This may be related to the tendency of dipoles in the sample pellets to orient themselves in line with the applied electric field direction [77]. On the other hand, the values of the dielectric storage remained constant with a change in frequency in the higher frequency range. The temperature change did not have much effect on the characteristics except with a slight shift in the transient frequencies. This trend remained the same for all the samples, with some variation in the magnitude of the dielectric constant values. It could be attributed to the fact that the rotation of dipoles is hindered by higher frequencies making it hard for the dipoles to reorient [77]. The dielectric constant rapidly decreased with an increase in frequency and remained very low and almost constant after the 1Hz frequency. This dielectric dispersion was larger for higher temperatures and decreased with temperature decrease. This dielectric behavior can be attributed to the mechanism of the polarization process in bismuth tellurides quite similar to that of the conduction process.

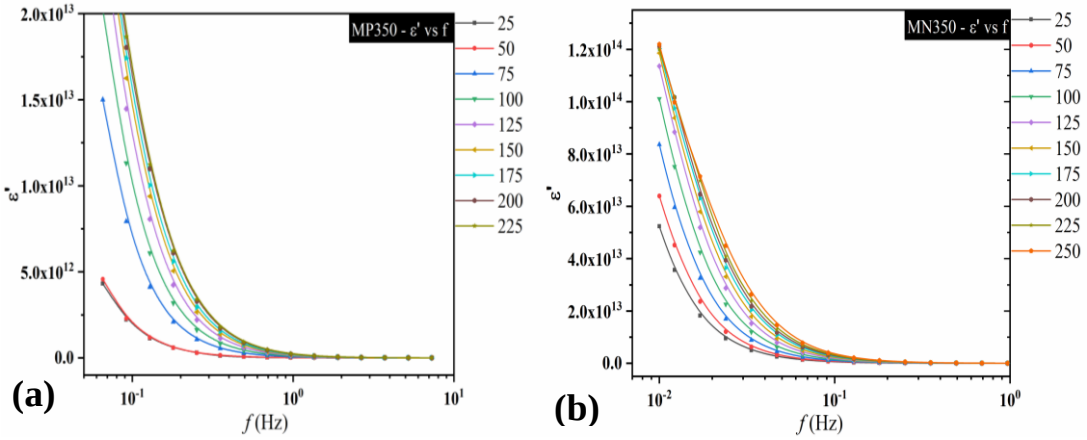

Figure 4-14**.** Frequency dependence of dielectric storage in the temperature range 25 ^{o}C to 375 ^{o}C for (a) p-type and (b) n-type Bi_2Te_3 samples sintered in microwave furnace sintered at 350 ^{o}C.

4.9.4 The variation of dielectric loss with frequency:

Dielectric permittivity loss can be loosely stated as the loss of energy when heating a material when the varying or AC electric field is applied. The dielectric losses rely on the frequency of the electric field applied and the permittivity or dielectric feature of the material.

Figure 4-15 shows the changes in the dielectric loss of the as-prepared and sintered bismuth telluride samples in the electromagnetic spectrum at various temperatures from 25 ^{o}C to 375 ^{o}C. ε'' is very high at low frequencies correspondent to the DC electrical conductivities, probably from the free charge polarization within the sample material [76]. This dielectric loss decreased linearly with an increase in frequency. So, it can be said that the dielectric loss increases with a temperature rise and decreases with an increase in frequency. The relation of this dielectric loss ε'' with frequency can be given from the power law [78],

$$\varepsilon'' = \mathrm{B}.\,\omega^{m}$$

where B and m are constant and frequency power factor, respectively. The plots of log ε'' versus log(freq) or log(ω) depict straight lines at different temperatures. The m

values can be obtained from the slopes of the lines at various temperatures using eq. (7). It can be observed that this m value tends to decrease with a temperature rise. The response of dielectric loss on the low-frequency side corresponds to the low AC conductivity and electric modulus values in this frequency range. The response of AC conductivity at a low frequency is DC conductivity. This response corresponds to the typical Debye relation given by $\sigma dc=2\pi f\varepsilon_o\varepsilon''$ [79].

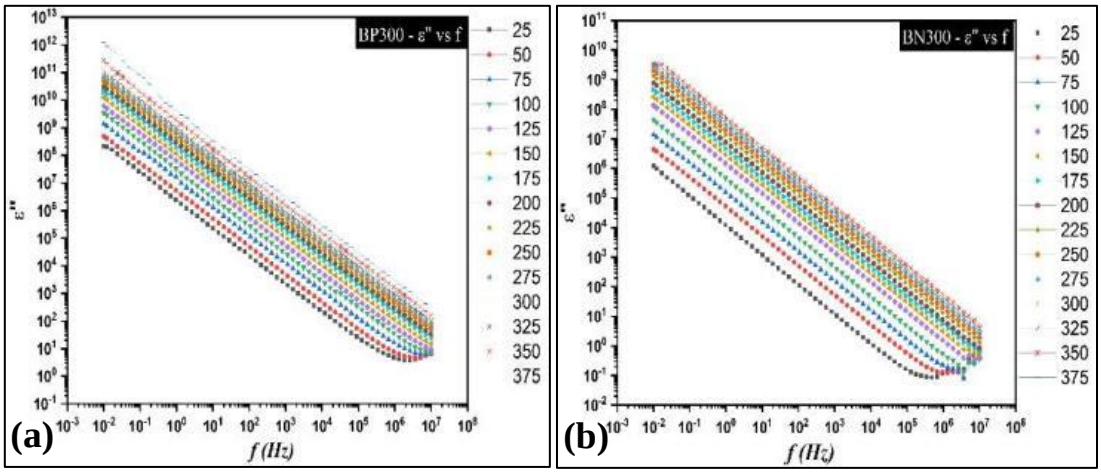

Figure 4-15**.** Frequency dependence of log of the imaginary part of permittivity or dielectric loss in the temperature range 25 ^oC to 375 ^oC for (a) p-type and (b) n-type Bi_2Te_3 samples sintered in the box furnace at 300 ^oC.

4.10 Conclusion:

In this work, we have treated p-type and n-type bismuth telluride nanocrystals using conventional, microwave, and tube sintering. The XRD, SEM, and EDX characterization were done to study the structural, compositional, and microscopic properties of the treated materials. The DC electrical conductivity and thermal conductivity were determined by the 4-point probe method and TCA test, respectively. The dielectric characterization was done using dielectric spectroscopy. The XRD analysis showed that the prepared materials remained stable with a single-phase at sintering temperatures 250 ^oC and 300 ^oC. However, beyond 300 ^oC, phase change occurred with the appearance of oxide impurities at 350 ^oC to 400 ^oC sintering

temperatures. This feature existed in all three furnaces and was more pronounced in the n-type samples, which was confirmed by the EDX data. The volatile nature of tellurium caused a decrease in its concentration with the increase in the sintering temperature. Also, the DC electrical conductivity decreased as the sintering temperature went from 250 ^{o}C to 400 ^{o}C with an increase in coarse and crystalline structures. On the contrary, the thermal conductivity increased with an increase in sintering temperatures. The EDS spectrum confirms the occurrence of tellurium deficiency due to its volatile nature at higher temperatures. The broadband dielectric spectroscopy confirmed that the conduction behavior in the samples was from the hopping mechanism, and the samples exhibited characteristics more similar to glass. Therefore, the samples had an exceptionally ultra-low thermal conductivity of approximately 0.4 W/m/K. The microwave furnace samples demonstrated better thermoelectric properties among all the sintering with an optimum annealing temperature of 250 ^{o}C. However, the higher oxidation levels have restricted the characteristics of the materials that can be avoided by acute control of the sintering atmospheres. The TGA test results indicate no weight loss until 350 ^{o}C measuring temperature signifying good thermal stability and the DSC results show two very sharp endothermic peaks around the melting points of bismuth and tellurium proposing a very good crystallinity in the samples. From the mechanical characterization tests, the hardness of the materials decreased with an increase in annealing temperature, which agrees with the previous literature. The corresponding nanohardness, Young's modulus, stiffness, and microhardness are 1.4 GPa, 5 GPa, 8689.2 N/mm, and 46.954 HV for the p-type and 350 MPa, 2.5 GPa, 8207 N/mm, and 46.9 HV for n-type samples. The treatment used here is simple, easy, quick, cost-effective, scalable, and provides superiority in terms of the enhancement of

thermoelectric properties. The bismuth telluride samples prepared by our work have a balance of electrical, thermal, mechanical properties, and a cost-effective fabrication process.

CHAPTER 5: OPTIMIZATION OF THERMOELECTRIC PROPERTIES OF COPPER SELENIDE

5.1 Introduction:

In this chapter, we deal with the enhancement of thermoelectric properties of p-type copper selenide by the microwave sintering method. The discovery of Chalcogenides as effective thermoelectric (TE) materials has influenced the way electricity is harnessed from waste heat. The primary materials developed for this purpose, such as lead-based TE or silicon-germanium, have scarce availability, high toxicity, and high costs, compelling researchers to search for low-toxic, low-cost, and sustainable alternatives. Copper-based chalcogenides have gathered a lot of attention over the past two decades due to their affordable accessibility, ecofriendly nature, and their intriguing semiconducting, physical, chemical, and optoelectronic properties that accommodate numerous applications in the field of energy conversion, energy harvesting, biomedical electronics, and sustainability. Additionally, these materials are driven by tailorable crystalline structure and chemical compositions through intelligent control of treatment, synthesis, and fabrication conditions. Our objective is to improve the thermoelectric properties of low-toxic and earth-abundant copper selenide thermoelectric material.

5.2 Experimental Details of copper selenide:

P-type Copper (I) Selenide powder was acquired from Nanoshel LLC (purity:99.995%, APS:100 μm) (Stock no: NS6130-12-000158). Cold compaction with pressure up to 50 MPa was unsuccessful in consolidating copper selenide powders, as shown in Figure S1(a) (Appendix B). Different pellets of weight 1.5 grams and 3.5 grams were made by the hot press (Carver, Model No. 4368, USA) at 250 ^{o}C temperature and a pressure of 350 MPa. The pellet made from hot pressing is

shown in Figure S1(b) (Appendix B). The 3.5 grams identical pellets were designed to measure the thermal conductivities of the samples. The diameter of all the pellets was 13 mm, and the thickness of 1.5 grams and 3.5 grams pellets were 2.58 mm and 5.3 mm, respectively. The compacted pellets were subjected to sintering at different temperatures 250 ^{o}C, 275 ^{o}C, 325 ^{o}C, 375 ^{o}C, 425 ^{o}C, and 725 ^{o}C in a microwave-assisted bidirectional rapid sintering method provided by (VB ceramic furnace, VBCC/MF/1600 ^{o}C/14/15, Chennai, India). The heating ramp rate was set at 10 ^{o}C. The samples were left at the target temperature for a dwell time of 10 mins and were removed from the furnace upon automatic slow cooling to room temperature. The specimens were then examined for microscopic, structural, electrical, thermal, and mechanical characterizations. The specimens are marked as CS250, CS275, CS325, CS375, CS425, and CS725. We have used Archimedes' method to calculate the sample densities The density of the hot-pressed sample was found to be 5.112 gm/cm^3 (75.36%). The volumetric densities of the annealed samples by this method were found to be in the range of 5.2-5.5 gm/cm^3 which is about 76-81% of the theoretical densities of copper selenide.

5.3 Structural characterization:

Figure 5-1 represents the X-ray diffraction patterns of pure and annealed samples of p-type copper selenide at different annealing temperatures. Powder XRD data were collected from the 7 Cu_2Se samples using Cu-Kα radiation to study the crystal structure by identifying the material's various crystalline phases, impurity phases, bonding, and structural behavior. One of the seven samples was a pristine or unannealed sample, while the rest were annealed at 250 ^{o}C, 275 ^{o}C, 325 ^{o}C, 375 ^{o}C, 425 ^{o}C, and 725 ^{o}C. The data for the XRD analysis were acquired in the 2θ range from 10^{o} to 90^{o}. The fitted profile and Bragg's peaks of all the samples except CS725

are depicted in Figure 5-1. The XRD profile of CS725 is given the Appendix B (Figure S2(b)). The famous Debye-Scherrer formula given by $D = {k\lambda}/{\beta . \cos(\theta)}$, was used to estimate the grain size of the samples. Here D is the crystallite or the grain size (in nm), λ is the wavelength of X-rays used (here $\lambda = 1.54$ nm for CuKα), $k = 0.93$ is the shape factor, θ is the Braggs angle, and β is the full width half maximum (FWHM) of the intensity peaks in radians. The variation of grain size with annealing temperature is given in Figure S2(a) (Appendix B).

The unannealed samples comprised of a pure single phase of copper selenide ($Cu_{1.83}Se$) of cubic structure as validated by ICDD:98-015-0760. The unannealed sample was pure with no impurities or any kind of external doping. The very sharp high-intensity peaks in the samples suggest a very high crystalline nature of the samples. An increase in the intensity of the CS250 peaks, especially at 2θ=44.4^{o} with (2 2 0) plane from the pure samples can be seen, implying an increase in the grain size of the annealed samples [28]. However, with the increase in the annealing temperatures, the intensities of the peaks decreased, and a slight peak broadening can be noticed. This resulted in a decrease in the grain size as the annealing temperature soared, as seen in Figure S2(a) (Appendix B). This behavior is probably because the crystallization kinetics of copper selenide, in this case, is more influenced by the nucleation rate, and the nucleation activation energy is comparatively higher than the growth activation energy in the crystal. Thus, as the crystallization temperature elevated, the rate of crystallization increased drastically. A similar response has been noticed in some of the previous works [80-82]. At annealing temperature above 400 ^{o}C, phase shifts and oxide impurity phases of copper selenide start to appear, as can be seen from the XRD profile of the CS425 sample. This oxide phase at different 2θ for CS425 samples is $Cu_2O_4Se_1$ as confirmed by ICDD: 98-006-0652. This oxide

concentration soared as the annealing temperature went further, and at 700 ºC, selenium evaporated utterly, leaving only monoclinic copper oxide (Cu_1O_1) phase as confirmed by ICDD: 98-062-8616 (refer Appendix B Figure S2(b)). To summarize, the samples were stable till the annealing temperature was 400 ºC, and beyond that temperature, oxidation started to occur, and this oxidation elevated with the temperature.

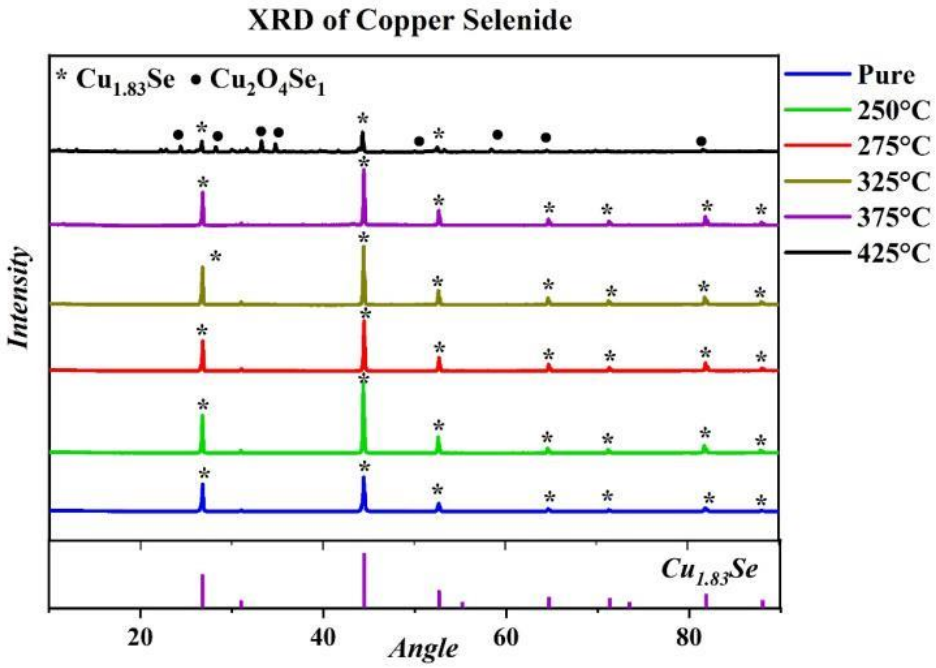

Figure 5-1. X-ray diffraction patterns of copper selenide pure and microwave annealed samples at 250 ºC, 275 ºC, 325 ºC, 375 ºC, and 425 ºC.

5.4 SEM and EDX:

The field emission scanning electron microscope (FESEM) and Energy Dispersive X-Ray Analysis (EDX) are used to analyze the surface morphological properties and elemental composition of the as-prepared and annealed copper selenide samples. The FESEM images of the samples at 5 µm magnification are given in Figure 5-2(a)-(f). The images illustrate the effect of the increase in annealing temperature on the crystallites of the samples. Figure 5-2(a) depicts the FESEM image of the as-prepared p-type sample. It is indicated that the pristine samples consisted of particles of

different sizes. The microwave annealing, especially at 250 ^{o}C of the hot-pressed samples resulted in densification. The smaller sub-micron particles of the pristine sample formed larger grains, as seen in Figure 5-2(b). This increase in the size of the grains post-annealing can be due to the increased mass transfer among the grains, especially at high temperatures. Simply put, the larger grains have formed due to the merging of smaller ones causing significant growth. However, at annealing temperatures beyond 300 ^{o}C and higher, the grain size decreased with increased temperatures. This can be credited to the atoms that have achieved enough thermal energy to travel to any location within the particle or undergo crystallographic rearrangement. As a result of the full-filled space within the crystallite, the grain size shrank. Beneficially, this phenomenon has contributed to the improvement in crystalline quality as the atom moved to a more favorable position. This decrease in grain size and the formation of uniform finer grains can be observed in the FESEM images and can be confirmed by the grain size measurements from the XRD data attached in Appendix B (Figure S2(b)). The sub-microns were in the range 400-1500 nm. Figure 5-2(g) shows the energy dispersive X-ray spectrum of the as-prepared p-type Cu_2Se sample, and the compositional data (both weight % and atomic %) for all the pristine and sintered samples are tabulated in Table 5-1.

From Table 5-1, the pristine and annealed samples' compositions show the copper selenide phases to be highly stable at lower temperatures. The samples consisted more of copper and less of selenium from the weight concentration data. Further, the concentration of copper increased, and selenium decreased as the annealing temperature increased. The variation of selenium with annealing temperature is given in Figure S3 (Appendix B). Completing compounds with more copper concentration, such as Cu2Se, Cu2O4Se1, and Cu1O1 could explain the decline of selenium.

Selenium reduces with annealing, and a similar phenomenon has been observed before [83, 84]. The oxygen presence can be observed in EDX data of the samples annealed above 400 ^{o}C and explains the oxidation confirmed previously from our XRD data.

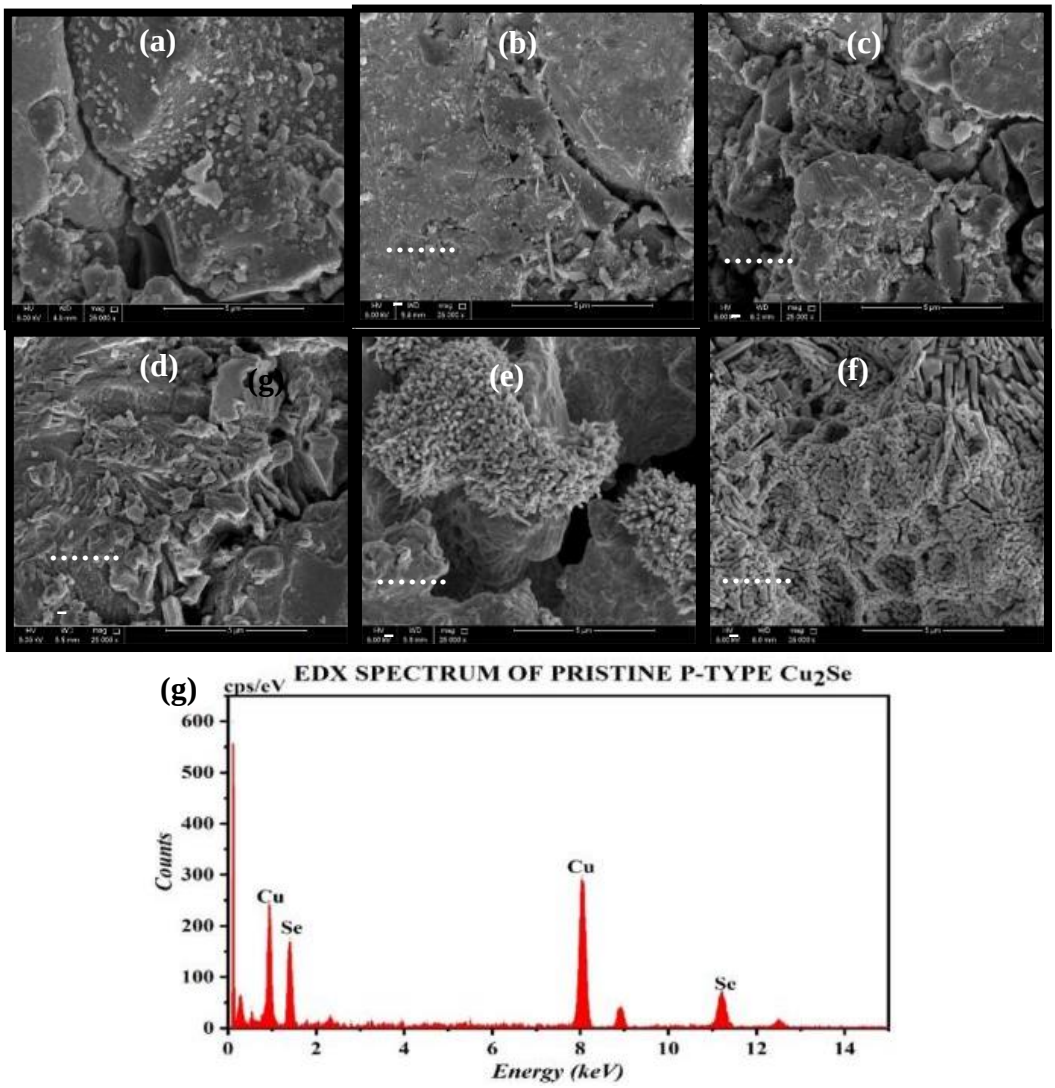

Figure 5-2. FESEM images at 5 µm magnification of (a) as-prepared p-type Cu_2Se sample, (b) CS250, (c) CS325, (d) CS375, (e) CS425, (f) CS725, (g) EDX spectrum of the as-prepared sample. The crystallite size decreased with increase in annealing temperatures and the size of sub-microns was less than 1 µm.

Table 5-4. Comparison of compositional analysis from the EDS data for the pristine and sintered p-type copper selenide samples.

(a) Atomic Percentage

	Pristine	Annealing Temperature					
Sample		250 ºC	275 ºC	325 ºC	375 ºC	425 ºC	725 ºC
Copper Cu	53.74	52.01	54.62	54.70	54.91	51.20	75.77
Selenium Se	46.26	47.99	45.38	45.30	45.09	38.35	2.15
Oxygen O						10.45	22.09

(b) Weight Percentage

	Pristine	Annealing Temperature					
Sample		250 ºC	275 ºC	325 ºC	375 ºC	425 ºC	725 ºC
Copper Cu	48.32	46.58	49.2	49.28	49.94	50.45	90.2
Selenium Se	51.68	53.42	50.8	50.72	50.51	46.96	3.18
Oxygen O						2.59	6.62

5.5 TEM:

Since the SEM images alone are inconclusive in determining the grain, we perform TEM analysis. The TEM images of the as-prepared and annealed (up to 375 ºC) p-type copper selenide samples are shown in Figure 5-3(a)-(h). The p-type ($Cu_{1.83}Se$) nanoparticles have a cubic lattice (space group: Fm-3m) with lattice parameters of a = 5.7600 Å and c = 5.7600 as confirmed by ICDD: 98–015–0760 data from the XRD data given before. The variation of the average particle size distribution of the samples was estimated using the ImageJ image processing program and is shown in Figure S10 (Appendix B). The size distribution range appears to be from 200 nm to 1400 nm. The particle size seems to be decreasing with an increase in annealing temperature as confirmed by both SEM and XRD. Here the size of the particles

appears to be smaller than revealed by the SEM images indicating nanoparticles formation in the designated samples. These nanoparticles have random particle size distribution with d-spacing between the lattice fringes in the range 0.27-0.38 nm corresponding to (111) plane of $Cu_{1.83}Se$ cubic structure hkl indices. The HRTEM images in Figure 5-3(b),(d),(f) & (h) clearly show the increase in d-spacing after annealing and decrease with an increase in annealing temperature. The corresponding selected area electron diffraction (SAED) pattern of the samples is illustrated in the inset of the HRTEM images. The crystallinity of the annealed samples improved with the increase in temperatures, as depicted by the SAED bright spot rings of the CS375 sample. This crystal nature validated by the SAED images agrees with the XRD observations.

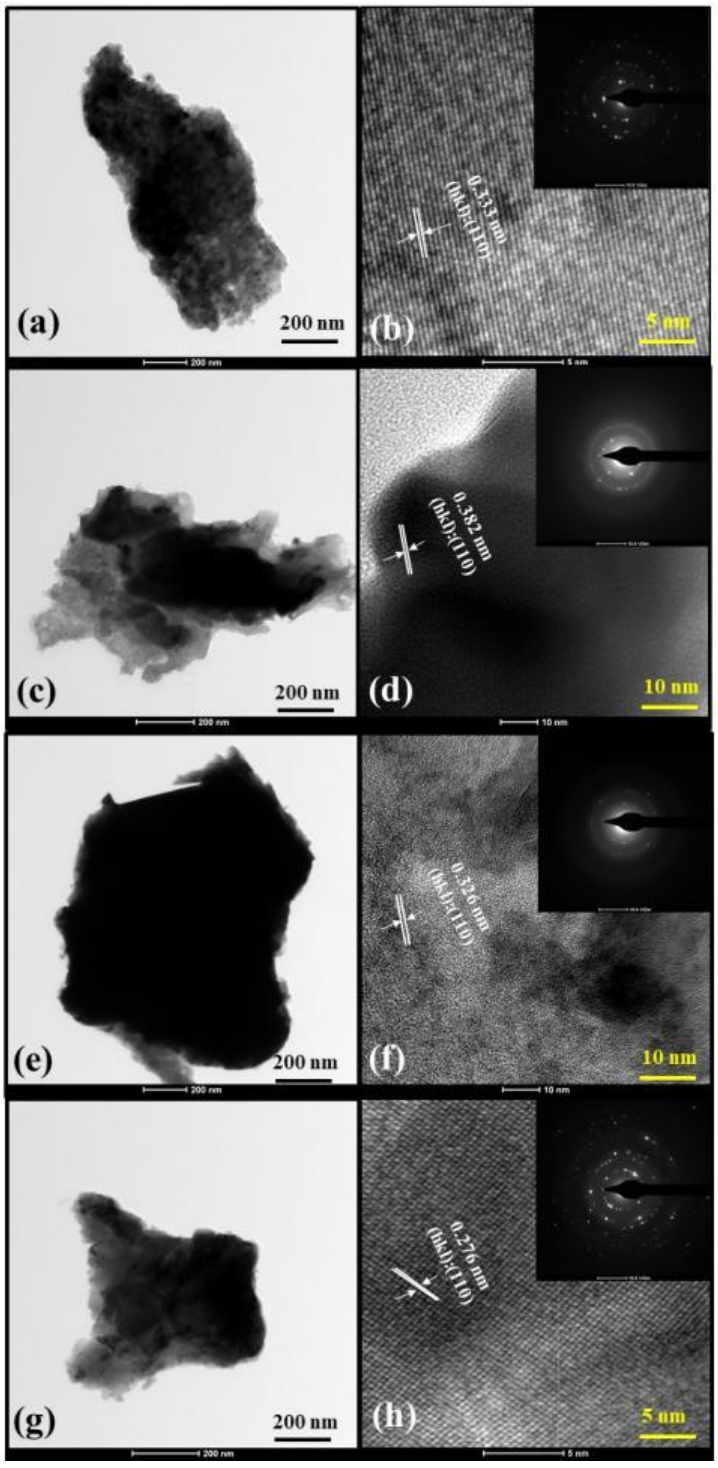

Figure 5-3. Low magnification transmission electron microscopy (TEM) image of the (a) pristine p-type Cu_2Se hot-pressed pellet, (c) CS250, (e) CS325, (g) CS375 at 200 nm resolution. High-resolution TEM (HRTEM) image of the (b) pristine p-type hot pressed Cu_2Se pellet, (d) CS250, (f) CS325, (h) CS375 at 2 nm and 5 nm, insets show the corresponding selected area electron diffraction (SAED) patterns.

5.6 Electrical characteristics:

The DC electrical conductivity was measured at room temperature of pure (non-sintered) and microwave sintered p-type copper selenide at various annealing temperatures by the Ossila 4-point probe system. The system applies DC signal on the samples and measures corresponding DC sheet resistance, resistivity, and conductivities. Figure 5-4 illustrates the variation of DC electrical conductivities. The DC electrical conductivity of the pure sample was 141.1 S/cm. The DC electrical conductivity of samples has improved after annealing with the highest conductivity for the CS375 sample of 538.3 S/cm. The increase in electrical conductivities with an increase in annealing temperatures up to 375 ^{o}C can be attributed to the high purity phases of the samples and a decrease in grain size, as confirmed by the XRD data. The reduction in grain size has led to a decrease in resistivities, thereby increasing the electrical conductivities [85]. The decrease in average grain size leads to enhancement in grain boundaries and increases the frequency of scattering defects for the electrons traveling through the lattice in the material [86]. The increase in electrical conduction within the material can be attributed to the predominance of grain-boundary conduction coupled with grain-boundary ionic diffusivity in the nanostructured materials as the grain size decreases. This behavior is also reported in other works on copper-based compounds [85, 87]. The electrical conductivity of the CS425 sample was 71.2 S/cm, which is way less than that of the pure samples. However, above 400^{o}C annealing temperatures, the oxide phases have primarily influenced the conduction behavior of samples. The oxidation by the formation of copper oxides increased the resistivity of the samples, consequently decreasing the conduction mechanism to a very large extent [88].

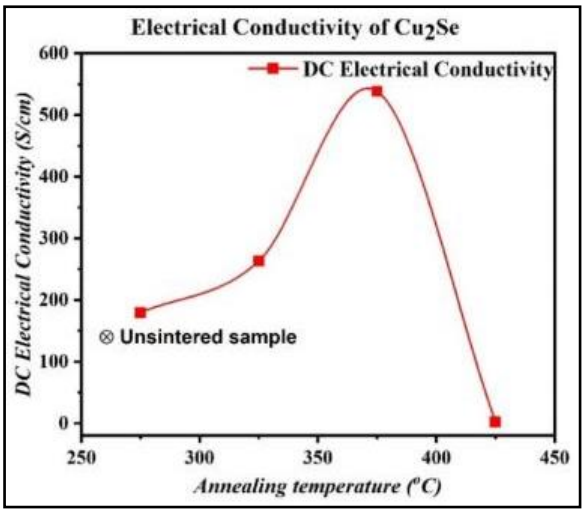

Figure 5-4. The variation of room temperature DC electrical conductivity of pure (non-sintered) and microwave sintered p-type copper selenide at various annealing temperatures.

5.7 Broadband dielectric spectroscopy results:

Insight into the behavior of materials over a large frequency spectrum (10^{-3} to 10^{10} Hz) as in the case of broadband dielectric spectroscopy technique offers a significant advantage over typical spectroscopies by enabling better access to different frequency processes (ex. Lattice process) that influence the electronic conduction mechanism in the material. Broadband spectroscopy assists in the comprehension of material behavior in the frequency range and the temperature range up to 400 ^{o}C. The electronic conduction mechanism in materials, especially in semiconductor materials, is challenging due to the high rate of complexity. The elements of materials have a very dynamic response when an electric field is applied. Various types of reactions may trigger the dielectric response of the semiconductor materials such as TE materials. Therefore, in this section, we study copper selenide thermoelectric material's electrical or dielectric behavior in both the frequency and temperature ranges.

The variation of AC electrical conductivity with measuring the temperature at

different frequencies for the CS250 sample is illustrated in Figure 5-5(a). Similarly, the variation of AC electrical conductivity, AC capacitance, dielectric permittivity storage, dielectric permittivity loss, and tan(δ) with frequency at different temperatures are depicted in Figure 5-5(b)-(f). The AC electrical conductivity is very low at measuring temperature below 350^{o}C and increases drastically at all the frequencies mainly due to higher mobility and increased carrier concentration from the introduction of defects (Figure 5-5(a)). A high AC electrical conductivity of nearly 0.06 S/cm was noted for samples annealed at 375 ^{o}C (Appendix B Figure S6(a)). The electrical conductivities were saturated at lower frequencies, and a significant boost is observed beyond 1 MHz frequency (Figure 5-5(b)).

The frequency-dependent response of AC capacitance is very high in the low-frequency region and decreases to become saturated in the high-frequency region (Figure 5-5(c)). Additionally, as the temperature increases the capacitance increase with an AC capacitance value of 7.5 mF at 375 ^{o}C for CS250 samples at low frequencies. The dispersion of interfacial charge carriers is a key component in increasing capacitance value in the frequency range. At higher temperatures, the accumulation of extra charge carriers at the interface states resulted in excess capacitance. This behavior is the response of a typical semiconducting material [89] and analogous results are reported for chalcogenide-based nanocomposites [90].

The real and imaginary part of dielectric permittivity as a function of frequency at various temperatures is given in Figure 5-5(d) & (e). The high values of dielectric constants, particularly in the low-frequency region, can be related to the grain boundaries and polarization mechanism. These measurements are in agreement with the famous Debye relaxation model [79]. The dielectric constant values increase at higher temperatures. These variations can be attributed to charge carriers' orientation

in the electric field's direction applied at lower temperatures. These charge carriers at higher temperatures gain adequate thermal excitation energy to repel the external electric field easily. We have previously reported similar behavior from our broadband dielectric spectroscopy study on bismuth telluride thermoelectrics [91].

The frequency-dependent dielectric loss tangent (tan(δ)) at various temperatures is revealed in Figure 5-5(f). As the frequency increases, tan(δ) decreases. The energy loss in the low-frequency area is substantial because the hopping of charge carriers among energy levels demands more energy. The conduction behavior of copper selenide in the low-frequency region has mainly been attributed to the charge carriers hooping between the localized states [92]. On the other hand, the high-frequency area encourages electron mobility between energy levels. As a result, the energy loss in the high-frequency zone is minimal. These results are consistent with previous works [93, 94]. Analogous dielectric behavior is noted in all the other samples with slight variations in the measurements (Appendix B data Figure S4-S8).

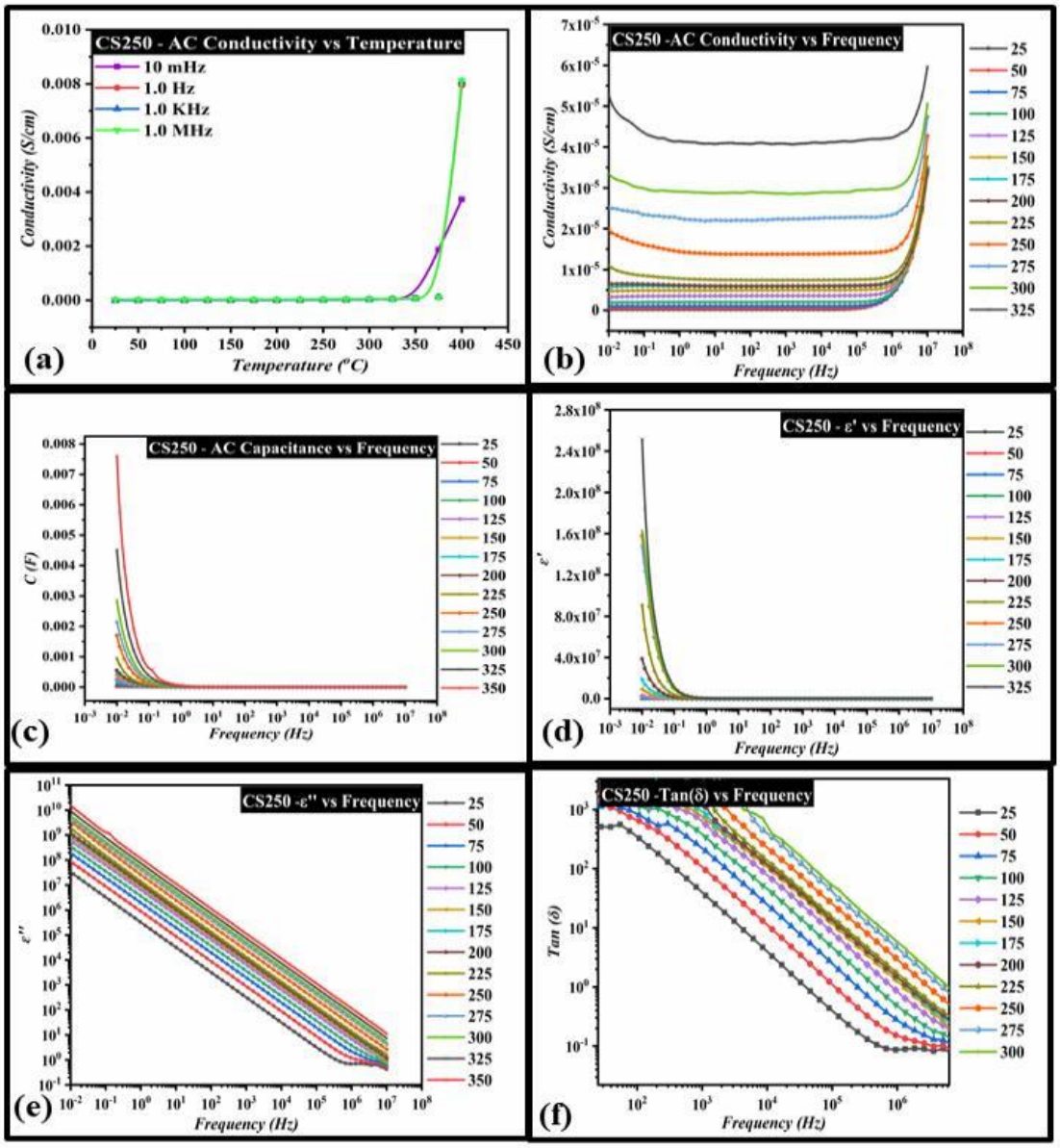

Figure 5-5. Alteration of (a) the AC electrical conductivity with temperature, (b) the AC electrical conductivity with frequency, (c) the AC capacitance with frequency, (d) the dielectric permittivity storage with frequency, (e) the dielectric permittivity loss with frequency, (f) the tan(δ) with frequency, in the range 25 ^{o}C to 400 ^{o}C at frequencies 10 mHz, 1 Hz, 1 kHz, and 1 MHz for the sample CS250. The conductivity is almost constant at low temperatures and increases drastically beyond 350 ^{o}C temperature.

5.8 Thermal characteristics:

The Thermal constants analyzer (TCA) equipment was used to examine these samples for thermal properties such as thermal diffusivity, specific heat capacity, and thermal conductivity. Two identical samples each of similar dimensions and conditions were made at each annealing temperature. Figure 5-6(a) illustrates the change in room temperature thermal conductivities with annealing temperature. The variation of thermal diffusivity and specific heat with annealing temperature is given in Appendix B (Figure S9). The pristine sample had a very high thermal conductivity (TC) of 2.4 W/mK. Post annealing, the thermal conductivities drastically reduced and were in the range of 0.59-0.94 W/mK. Thus, microwave-assisted annealing, especially at low temperatures, has significantly enhanced the thermal profile of the samples. There has been an increase in thermal conductivity at high annealing temperatures. For example, at 725 ^{o}C, the measured TC at room temperature was 1.35 W/mK. Oxides of copper are better conductors of heat than the single and pure phase copper selenides. This response aligns with the existing report [95]. Figure 5-6(b) represents the weight % variation of p-type copper selenide until the samples reach 800 ^{o}C temperature. In the case of the pristine samples, there is negligible weight loss up to 300 ^{o}C temperature suggesting high thermal stability until 300 ^{o}C. However, when the pellets were annealed, the temperature at which the weight loss occurred went higher, signifying a boost in thermal stability of Cu_2Se with an increase in annealing temperature. The samples exhibited excellent thermal stability up to 500 ^{o}C for CS725 samples.

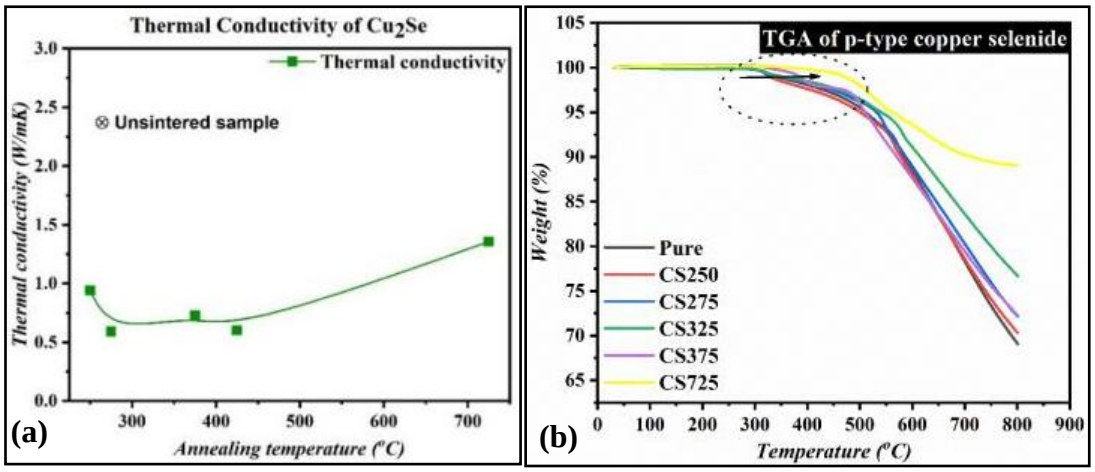

Figure 5-6. The variation of room temperature (a) thermal conductivity, and (b) TGA weight loss curves of pure (non-sintered) and microwave sintered p-type copper selenide at various annealing temperatures.

5.9 Mechanical characteristics:

The reliability, robustness, durability, and longevity of thermoelectric materials rely on their mechanical properties. These properties, in some way, also determine the efficiency of the TE material and are very crucial for practical applications. An excellent TE material has admirable mechanical stability and withstands high stress encountered in the practical environment all while maintaining the thermoelectric properties. Most of the works focused on developing copper selenide material mainly concentrated on improving the thermoelectric properties. Fewer works have reported the mechanical properties of copper selenide TE material [96-99]. Currently, in our paper, we have reported the nanoindentation and compression tests results, and our findings suggest considerable improvement in mechanical characteristics over the existing literature.

5.9.1 Nanoindentation:

The force-indentation depth curves, nanohardness, and young modulus variation with annealing temperature of microwave sintered copper selenide samples are illustrated in Figure 5-7(a). The penetration depth from the load-displacement curves decreased

with an increase in annealing temperature up to 375 ^{o}C. This consistent decrease implies improvement in nanohardness of the copper selenide samples that align with our compression test results. The penetration depth of samples annealed at 425 ^{o}C increased, suggesting a decline in nanohardness values. The dependence of young's modulus and nanohardness on annealing temperature is plotted in Figure 5-7(b). The nanohardness and young's modulus of pure samples were 455.47 MPa and 2.05 GPa, respectively. Post annealing, these values improved consistently with the maximum nanohardness, and young's modulus was reported for samples annealed at 375 ^{o}C (3.75 GPa and 7.13 GPa, respectively). A similar response has been reported in [100]. Reports show that Young's modulus and nanohardness increase with a decrease in grain size [101]. The higher densification in the annealed samples contributes to the reduction in grain size, causing an increase in the number of grain boundaries that improves the elasticity of the material by creating structural obstructions to the propagation of cracks within the samples. These findings indicate that the samples were mechanically stable below 400 °C annealing temperatures, but the higher temperatures damaged the structure and made the samples brittle. To the best of our knowledge, this is the first work reporting the nanohardness results for copper selenide thermoelectric materials.

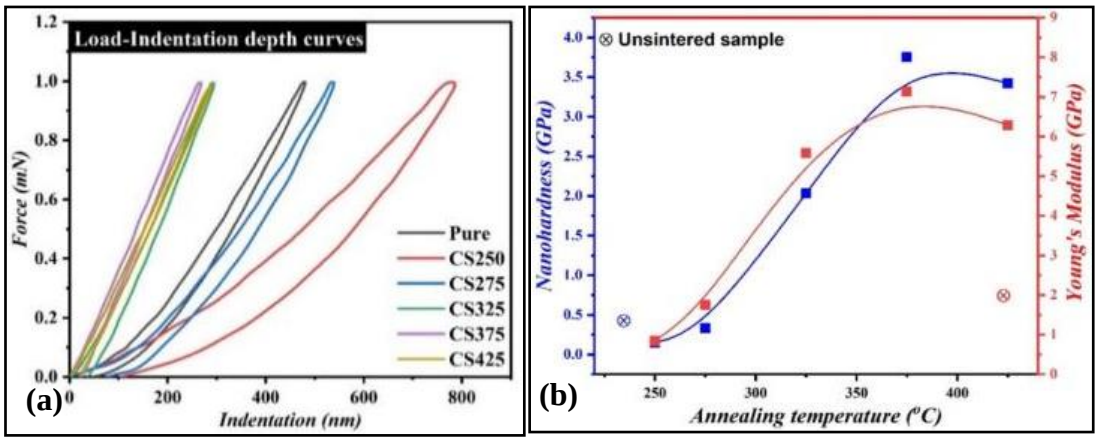

Figure 5-7. Nanoindentation assessment of pure and annealed copper selenide

samples; (a) Force-indentation depth curves, and (b) Nanohardness and Young's modulus variation with annealing temperature.

5.9.2 Compression test:

The variation of room temperature yield strength and compressive strength with annealing temperature of microwave-sintered copper selenide thermoelectrics under uniaxial compressive loading is plotted in Figure 5-8(a). The compressive and yield strength of pure non-sintered samples was 97.353 MPa and 77.727 MPa, respectively. The annealed samples exhibited higher strength than the pure samples. Furthermore, the compressive and yield strength increased with an increase in annealing temperatures and reached a maximum value of 326.75 MPa and 307.61 MPa, respectively, at 375 ^{o}C temperature. This surge in strength can be associated with the nanostructuring approach's boost in grain boundary strengths. The strength of the samples deteriorated above an annealing temperature of more than 400 ^{o}C, suggesting a negative effect of high annealing temperatures. To the best of our knowledge, the values of strengths achieved for Cu_2Se TE materials are significant improvements over the other works reported on Cu_2Se, as depicted in Figure 5-8(b) [96-98].

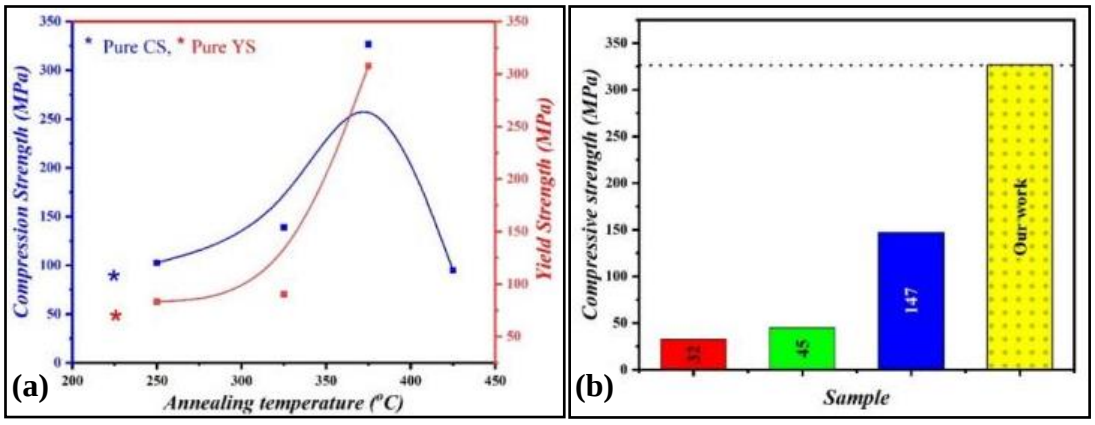

Figure 5-8. (a) The variation of compression and yield strength with annealing temperature for microwave-annealed copper selenide thermoelectrics, (b) Comparison of maximum compressive strength of our work with previously reported values for

copper selenide TE (32.5 MPa [96], 45 MPa [97], and 147 MPa [98]).

5.10 Conclusion:

In this chapter, we have treated low-cost, low-toxic, and earth-abundant p-type copper selenide thermoelectric materials using a microwave-assisted metallurgy route. The crystalline structural analysis (XRD) and compositional study (EDX) validated the samples' pure, single-phase, and high crystallinity nature up to 400 ^{o}C annealing temperature. The microscopic analysis (SEM & TEM) suggested the agglomerated particle size of the samples to be in the range of 100-200 nm. The optimized annealing temperature for microwave annealing was around 375 ^{o}C with very high electrical conductivity (room temperature) of 538.3 S/cm, ultra-low thermal conductivity of 0.59 W/mK, superior nanohardness, and compression strength of 3.75 GPa and 326.75 MPa, respectively. The electrical, thermal, and mechanical characteristics improved until the annealing temperature reached 375 ^{o}C and deteriorated above 400 ^{o}C. The broadband dielectric spectroscopy established that the samples responded to typical semiconducting material. The state-of-the-art results achieved by our work contribute to the development of cost-effective, lead-free, and reliable Copper selenide-based thermoelectrics.

CHAPTER 6: SUMMARY AND FUTURE WORK

6.1 Summary:

Bismuth telluride and copper selenide thermoelectric materials were prepared and their thermoelectric properties were studied. In this pursuit, several methods were employed such as cold compaction, hot pressing, conventional sintering, microwave sintering, and tube sintering to improve the TE materials characteristics. Also, a detailed study of broadband dielectric spectroscopy was accomplished deliberately to study the temperature and frequency response of the TE materials.

In the first part, optimum sintering techniques and sintering temperature for cold-compact p-type and n-type bismuth telluride were investigated. The impact of different sintering conditions and temperatures on the morphological, electric, thermal, and mechanical characteristics of the bismuth telluride TE materials were studied. The results confirmed that the microwave furnace samples demonstrated better thermoelectric properties compared to other sintering methods featuring an optimum annealing temperature of 250 °C. Phase change occurred with the appearance of oxide impurities at 350–400 °C sintering temperatures. Also, the DC electrical conductivity decreased as the sintering temperature increased from 250 °C to 400 °C. This was accompanied by an increase in coarse and crystalline structures. On the contrary, the thermal conductivity increased with an increase in sintering temperatures. The broadband dielectric spectroscopy confirmed that the conduction behavior in the samples was from the hopping mechanism, and the samples exhibited characteristics more similar to glass. In addition, the samples exhibited good thermal and mechanical stability. The corresponding nanohardness, Young's modulus, stiffness, and microhardness are 1.4 GPa, 5 GPa, 8689.2 N/mm, and 46.954 HV for the p-type and 350 MPa, 2.5 GPa, 8207 N/mm, and 46.9 HV for n-type samples.

These values are less than the microhardness values available in some of the ongoing research literature (60 HV [18] and 58 HV [63]) but the thermal conductivities of those compounds are very much higher than our current work [64] and overshadows the gain provided by the improved Vickers hardness. Improvement in microhardness should not be achieved by compromising the electric and thermal characteristics of the finish product. To our knowledge, this is the highest Vickers hardness achieved with ultra-low thermal conductivities for bismuth telluride thermoelectrics.

In the second part, we optimized the thermoelectric properties of low-toxic and earth-abundant copper selenide TE material by varying the sintering temperature in a microwave furnace. The microscopic analysis (SEM & TEM) suggested that the agglomerated particle size of the samples is in the range of 100-200 nm. The optimized annealing temperature for microwave annealing was around 375 ^{o}C with very high electrical conductivity (room temperature) of 538.3 S/cm, an ultra-low thermal conductivity of 0.59 W/mK, superior nanohardness, and compression strength of 3.75 GPa and 326.75 MPa, respectively for CS375 samples. The electrical, thermal, and mechanical characteristics improved until the annealing temperature reached 375 ^{o}C and deteriorated above 400 ^{o}C. The broadband dielectric spectroscopy showed that the samples responded to typical semiconducting material. To the best of our knowledge, the values of strengths achieved for Cu_2Se TE materials are significant improvements over the other works reported on Cu_2Se [96-98]

The research conducted in this thesis was mainly dedicated to improving the thermoelectric properties of the low-toxic and earth-abundant chalcogenide-based thermoelectric materials in both low and intermediate temperature range applications. The results achieved throughout this work are expected to support the acceleration of the commercialization of low-cost, sustainable, and eco-friendly thermoelectric

modules for waste-heat recovery.

6.2 Future work:

Like any research work and open-ended problems, this work has opened doors for several future studies. The results discussed above can be tested and implemented in industrial and deep-space missions to develop thermoelectric generators for waste-heat recovery. We have developed p-type and n-type bismuth telluride and copper selenide TE materials in our lab and our future goal is to construct a thermoelectric generator that can operate in low and intermediate temperature range applications. Even though our results suggested that the prepared materials had excellent thermal properties, the materials slightly lag in terms of electrical behavior. Also, our lab-scale prototypes are required to be tested in practical applications. Additionally, the density of the samples is lower than the theoretical densities suggesting the excess contribution of pores to the TE characteristics. Superior densification is necessary for high-performance TE materials. Further works are required to address these issues. Some of the future endeavors might read:

1. Determine the Seebeck coefficient, power factor, and figure of merit of the TE materials prepared previously.
2. Further, resonant doping and interface engineering can enhance the thermoelectric properties.
3. Construct a thermoelectric cell or generator by alternatively and serially connecting p and n-type material using electrical conducting wires or tape and determine the efficiency of the TEG.
4. Determine the thermoelectric properties and mechanical reliability of the TEGs in practical environments.
5. Design a hybrid solar-thermal system by coupling the photovoltaic and TEG

system with the thermoelectric generator connected on the back of the PV cell using an analytical approach and calibrating the overall power conversion efficiency of the hybrid system. Additionally, the system will be tested under practical applications in the Qatar environment.

REFERENCES

[1] D. M. Rowe, *CRC handbook of thermoelectrics*. CRC press, 2018.

[2] D. M. Rowe, *Thermoelectrics handbook: macro to nano*. CRC press, 2018.

[3] L. Probst, B. Pedersen, and L. Dakkak-Arnoux, "Energy harvesting to power the rise of the internet of things," *Digital Transformation Monitor*, 2017.

[4] M. K. M. Chaturvedi, "Synthesis and Investigation of Thermo-Electric properties of Skutterudites CoSb3/Graphene particles nanocomposite," National Physical Laboratory, New Delhi.

[5] J. Cohn, G. Nolas, V. Fessatidis, T. Metcalf, and G. Slack, "Glasslike heat conduction in high-mobility crystalline semiconductors," *Physical Review Letters*, vol. 82, no. 4, p. 779, 1999.

[6] O. Yamashita, S. Tomiyoshi, and K. Makita, "Bismuth telluride compounds with high thermoelectric figures of merit," *Journal of Applied Physics*, vol. 93, no. 1, pp. 368-374, 2003.

[7] Y. Zhang *et al.*, "Influence of copper telluride nanodomains on the transport properties of n-type bismuth telluride," *Chemical Engineering Journal*, vol. 418, p. 129374, 2021/08/15/ 2021, doi: https://doi.org/10.1016/j.cej.2021.129374.

[8] Z.-H. Ge, Y.-H. Ji, Y. Qiu, X. Chong, J. Feng, and J. He, "Enhanced thermoelectric properties of bismuth telluride bulk achieved by telluride-spilling during the spark plasma sintering process," *Scripta Materialia*, vol. 143, pp. 90-93, 2018/01/15/ 2018, doi: https://doi.org/10.1016/j.scriptamat.2017.09.020.

[9] B. Zhou, Y. Zhao, L. Pu, and J.-J. Zhu, "Microwave-assisted synthesis of nanocrystalline Bi2Te3," *Materials Chemistry and Physics*, vol. 96, no. 2-3,

pp. 192-196, 2006.

[10] D. H. Kim, C. Kim, S. H. Heo, and H. Kim, "Influence of powder morphology on thermoelectric anisotropy of spark-plasma-sintered Bi–Te-based thermoelectric materials," *Acta Materialia,* vol. 59, no. 1, pp. 405-411, 2011.

[11] D. Kong *et al.*, "Topological insulator nanowires and nanoribbons," *Nano letters,* vol. 10, no. 1, pp. 329-333, 2010.

[12] E. Ashalley, H. Chen, X. Tong, H. Li, and Z. M. Wang, "Bismuth telluride nanostructures: preparation, thermoelectric properties and topological insulating effect," *Frontiers of Materials Science,* vol. 9, no. 2, pp. 103-125, 2015.

[13] P. Anandan *et al.*, "Tailoring bismuth telluride nanostructures using a scalable sintering process and their thermoelectric properties," *CrystEngComm,* vol. 16, no. 34, pp. 7956-7962, 2014.

[14] E. M. MODAN and A. G. PLĂIAȘU, "Advantages and disadvantages of chemical methods in the elaboration of nanomaterials," *The Annals of "Dunarea de Jos" University of Galati. Fascicle IX, Metallurgy and Materials Science,* vol. 43, no. 1, pp. 53-60, 2020.

[15] S. Augustine and E. Mathai, "Dislocation, annealing and quenching effects on the microindentation hardness of Bi2Te3 and Bi2Te2. 9Se. 1 single crystals," *Materials characterization,* vol. 52, no. 4-5, pp. 253-262, 2004.

[16] L.-D. Zhao, B.-P. Zhang, J.-F. Li, M. Zhou, W.-S. Liu, and J. Liu, "Thermoelectric and mechanical properties of nano-SiC-dispersed Bi2Te3 fabricated by mechanical alloying and spark plasma sintering," *Journal of Alloys and Compounds,* vol. 455, no. 1-2, pp. 259-264, 2008.

[17] Y. Pan, T.-R. Wei, Q. Cao, and J.-F. Li, "Mechanically enhanced p-and n-type

Bi2Te3-based thermoelectric materials reprocessed from commercial ingots by ball milling and spark plasma sintering," *Materials Science and Engineering: B,* vol. 197, pp. 75-81, 2015.

[18] S. Bano, A. Kumar, B. Govind, D. Nayak, N. Vijayan, and D. Misra, "Investigation of micro-indentation hardness of Bi2Te3 based composite thermoelectric materials," in *AIP Conference Proceedings*, 2020, vol. 2220, no. 1: AIP Publishing LLC, p. 120006.

[19] J. Qiu *et al.*, "3D Printing of highly textured bulk thermoelectric materials: mechanically robust BiSbTe alloys with superior performance," *Energy & Environmental Science,* vol. 12, no. 10, pp. 3106-3117, 2019.

[20] P. Hankare, A. Khomane, P. Chate, K. Rathod, and K. Garadkar, "Preparation of copper selenide thin films by simple chemical route at low temperature and their characterization," *Journal of Alloys and Compounds,* vol. 469, no. 1-2, pp. 478-482, 2009.

[21] Y. Zhang, C. Hu, C. Zheng, Y. Xi, and B. Wan, "Synthesis and Thermoelectric Property of Cu2− x Se Nanowires," *The Journal of Physical Chemistry C,* vol. 114, no. 35, pp. 14849-14853, 2010.

[22] Z. Zhang, K. Zhao, T.-R. Wei, P. Qiu, L. Chen, and X. Shi, "Cu 2 Se-Based liquid-like thermoelectric materials: looking back and stepping forward," *Energy & Environmental Science,* vol. 13, no. 10, pp. 3307-3329, 2020.

[23] W.-D. Liu, L. Yang, and Z.-G. Chen, "Cu2Se thermoelectrics: property, methodology, and device," *Nano Today,* vol. 35, p. 100938, 2020.

[24] K. Tyagi *et al.*, "Enhanced thermoelectric performance of spark plasma sintered copper-deficient nanostructured copper selenide," *Journal of Physics and Chemistry of Solids,* vol. 81, pp. 100-105, 2015.

[25] V. B. Ghanwat *et al.*, "Microwave assisted synthesis, characterization and thermoelectric properties of nanocrystalline copper antimony selenide thin films," *RSC advances,* vol. 4, no. 93, pp. 51632-51639, 2014.

[26] J. Li, W. Fa, Y. Li, H. Zhao, Y. Gao, and Z. Zheng, "Simultaneous phase and morphology controllable synthesis of copper selenide films by microwave-assisted nonaqueous approach," *Solid state sciences,* vol. 16, pp. 125-129, 2013.

[27] V. B. Ghanwat, S. S. Mali, C. S. Bagade, R. M. Mane, C. K. Hong, and P. Bhosale, "Thermoelectric Properties of Indium (III)-Doped Copper Antimony Selenide Thin Films Deposited Using a Microwave-Assisted Technique," *Energy Technology,* vol. 4, no. 7, pp. 835-842, 2016.

[28] D. Shi, Z. Geng, and K. H. Lam, "Study of conventional sintered Cu2Se thermoelectric material," *Energies,* vol. 12, no. 3, p. 401, 2019.

[29] R. Seshadri, B. D. Rao, V. Narayanaswamy, and L. Rangaraj, "Design and fabrication of a laboratory model uniaxial hot press," in *Proceedings of the National Conference on High Pressure Science and Technology*, 1994, pp. 10-11.

[30] S. Mishra, S. Satpathy, and O. Jepsen, "Electronic structure and thermoelectric properties of bismuth telluride and bismuth selenide," *Journal of Physics: Condensed Matter,* vol. 9, no. 2, p. 461, 1997.

[31] J. Drabble and C. Goodman, "Chemical bonding in bismuth telluride," *Journal of Physics and Chemistry of Solids,* vol. 5, no. 1-2, pp. 142-144, 1958.

[32] H. Goldsmid, "Recent studies of bismuth telluride and its alloys," *Journal of Applied Physics,* vol. 32, no. 10, pp. 2198-2202, 1961.

[33] H. Mamur, M. Bhuiyan, F. Korkmaz, and M. Nil, "A review on bismuth

telluride (Bi2Te3) nanostructure for thermoelectric applications," *Renewable and Sustainable Energy Reviews,* vol. 82, pp. 4159-4169, 2018.

[34] M. Petrović *et al.*, "Optical Properties of CuSe Thin Films–Band Gap Determination," *Science of Sintering,* vol. 49, no. 2, 2017.

[35] D. Voneshen, H. Walker, K. Refson, and J. Goff, "Hopping time scales and the phonon-liquid electron-crystal picture in thermoelectric copper selenide," *Physical review letters,* vol. 118, no. 14, p. 145901, 2017.

[36] S. C. Singh *et al.*, "Structural and compositional control in copper selenide nanocrystals for light-induced self-repairable electrodes," *Nano Energy,* vol. 51, pp. 774-785, 2018.

[37] J. Y. C. Liew, Z. A. Talib, Z. Zainal, M. A. Kamarudin, N. H. Osman, and H. K. Lee, "Structural and transport mechanism studies of copper selenide nanoparticles," *Semiconductor Science and Technology,* vol. 34, no. 12, p. 125017, 2019.

[38] M. Takashiri, S. Kai, K. Wada, S. Takasugi, and K. Tomita, "Role of stirring assist during solvothermal synthesis for preparing single-crystal bismuth telluride hexagonal nanoplates," *Materials Chemistry and Physics,* vol. 173, pp. 213-218, 2016/04/15/ 2016, doi: https://doi.org/10.1016/j.matchemphys.2016.02.007.

[39] H. Kim *et al.*, "Ultralow thermal conductivity of β-Cu2Se by atomic fluidity and structure distortion," *Acta Materialia,* vol. 86, pp. 247-253, 2015/03/01/ 2015, doi: https://doi.org/10.1016/j.actamat.2014.12.008.

[40] M. Govindaraju *et al.*, "Investigations on the tribological behavior of functionally gradient iron-based brake pad material," *Proceedings of the Institution of Mechanical Engineers, Part C: Journal of Mechanical*

Engineering Science, vol. 234, no. 12, pp. 2474-2486, 2020.

[41] R. H. Castro, "Overview of conventional sintering," in *Sintering*, 2012: Springer, pp. 1-16.

[42] D. Agrawal, "Microwave sintering of ceramics, composites and metallic materials, and melting of glasses," *Transactions of the Indian ceramic society,* vol. 65, no. 3, pp. 129-144, 2006.

[43] S. Ramesh *et al.*, "Comparison between microwave and conventional sintering on the properties and microstructural evolution of tetragonal zirconia," *Ceramics International,* vol. 44, no. 8, pp. 8922-8927, 2018.

[44] X. Y. Han, X. Xing, H. F. Cheng, and J. Wang, "Reducing thermal conductivity of polymer derived SiC ceramics via microwave sintering processing," in *Advanced Materials Research*, 2012, vol. 476: Trans Tech Publ, pp. 932-935.

[45] H. Sun *et al.*, "Shape Memory Alloy Bimorph Microactuators by Lift-Off Process," *Journal of Micro and Nano-Manufacturing,* vol. 8, no. 3, 2020, doi: 10.1115/1.4048146.

[46] U. Holzwarth and N. Gibson, "The Scherrer equation versus the 'Debye-Scherrer equation'," *Nature Nanotechnology,* vol. 6, no. 9, pp. 534-534, 2011/09/01 2011, doi: 10.1038/nnano.2011.145.

[47] F. F. Jaldurgam, Z. Ahmad, and F. Touati, "Low-toxic, earth-abundant nanostructured materials for thermoelectric applications," *Nanomaterials,* vol. 11, no. 4, p. 895, 2021.

[48] D. Wright, "Thermoelectric properties of bismuth telluride and its alloys," *Nature*, vol. 181, no. 4612, pp. 834-834, 1958.

[49] U. Holzwarth and N. Gibson, "The Scherrer equation versus the'Debye-

Scherrer equation'," *Nature nanotechnology*, vol. 6, no. 9, pp. 534-534, 2011.

[50] D. Smyth, "Electrical Conductivity in Ceramics: A Review," *Ceramic Microstructures' 86,* pp. 643-655, 1987.

[51] Y.-P. Wang, S.-S. Li, W.-X. Ji, C.-W. Zhang, P. Li, and P.-J. Wang, "Bismuth oxide film: a promising room-temperature quantum spin Hall insulator," *Journal of Physics: Condensed Matter,* vol. 30, no. 10, p. 105303, 2018.

[52] N. Anisimova, G. Bordovsky, V. Bordovsky, and V. Seldayev, "Electrical and thermal properties of Bi2O3, PbO and mixed oxides of Bi2O3-PbO system," in *2004 IEEE international conference on solid dielectrics (Toulouse, July 5-9, 2004)*, 2004.

[53] W. Brostow *et al.*, "Bismuth telluride-based thermoelectric materials: Coatings as protection against thermal cycling effects," *Journal of Materials Research,* vol. 27, no. 22, p. 2930, 2012.

[54] R. Setnescu, I. Bancuta, T. Setnescu, V. Cimpoca, S. Jipa, and I. Popescu, "Thermal characterization of semiconductor Bi2Te3 materials using DSC," *Journal of Science and Arts*, vol. 1, no. 12, pp. 95-102, 2010.

[55] M. C. Righetti, "Crystallization of polymers investigated by temperature-modulated DSC," *Materials,* vol. 10, no. 4, p. 442, 2017.

[56] K. Singkaselit, A. Sakulkalavek, and R. Sakdanuphab, "Effects of annealing temperature on the structural, mechanical and electrical properties of flexible bismuth telluride thin films prepared by high-pressure RF magnetron sputtering," *Advances in Natural Sciences: Nanoscience and Nanotechnology,* vol. 8, no. 3, p. 035002, 2017.

[57] J. Stef *et al.*, "Mechanism of porosity formation and influence on mechanical properties in selective laser melting of Ti-6Al-4V parts," *Materials & Design,*

vol. 156, pp. 480-493, 2018/10/15/ 2018, doi: https://doi.org/10.1016/j.matdes.2018.06.049.

[58] P. Zhao *et al.*, "Porous bismuth antimony telluride alloys with excellent thermoelectric and mechanical properties," *Journal of Materials Chemistry A*, vol. 9, no. 8, pp. 4990-4999, 2021.

[59] B. Madavali *et al.*, "Effect of Sintering Temperature on Thermoelectric Properties of p-Bi2Te3 Alloys Produced by Gas Atomization," *International Journal of Applied Ceramic Technology*, vol. 13, no. 2, pp. 245-251, 2016.

[60] G. Li *et al.*, "Ideal strength and deformation mechanism in high-efficiency thermoelectric SnSe," *Chemistry of Materials*, vol. 29, no. 5, pp. 2382-2389, 2017.

[61] H. R. Williams *et al.*, "Spark plasma sintered bismuth telluride-based thermoelectric materials incorporating dispersed boron carbide," *Journal of Alloys and Compounds*, vol. 626, pp. 368-374, 2015.

[62] K. Kubota, M. Mabuchi, and K. Higashi, "Review processing and mechanical properties of fine-grained magnesium alloys," *Journal of Materials Science*, vol. 34, no. 10, pp. 2255-2262, 1999.

[63] N. Bomshtein, G. Spiridonov, Z. Dashevsky, and Y. Gelbstien, "Thermoelectric, structural, and mechanical properties of spark-plasma-sintered submicro-and microstructured p-Type Bi 0.5 Sb 1.5 Te 3," *Journal of electronic materials*, vol. 41, no. 6, pp. 1546-1553, 2012.

[64] F. F. Jaldurgam *et al.*, "Optimum sintering method and temperature for cold compact Bismuth Telluride pellets for thermoelectric applications," *Journal of Alloys and Compounds*, p. 160256, 2021.

[65] G. Nolas, D. Morelli, and T. M. Tritt, "Skutterudites: A phonon-glass-electron

crystal approach to advanced thermoelectric energy conversion applications," *Annual Review of Materials Science,* vol. 29, no. 1, pp. 89-116, 1999.

[66] Y. Zheng *et al.*, "Mechanically robust BiSbTe alloys with superior thermoelectric performance: a case study of stable hierarchical nanostructured thermoelectric materials," *Advanced Energy Materials,* vol. 5, no. 5, p. 1401391, 2015.

[67] B. Chen *et al.*, "Simultaneous enhancement of the thermoelectric and mechanical performance in one-step sintered n-type Bi2Te3-based alloys via a facile MgB2 doping strategy," *ACS applied materials & interfaces,* vol. 11, no. 49, pp. 45746-45754, 2019.

[68] D. Mei, H. Wang, Z. Yao, and Y. Li, "Ultrasonic-assisted hot pressing of Bi2Te3-based thermoelectric materials," *Materials Science in Semiconductor Processing*, vol. 87, pp. 126-133, 2018.

[69] F. Kremer and A. Schönhals, *Broadband dielectric spectroscopy*. Springer Science & Business Media, 2002.

[70] Q. Zhang *et al.*, "Deep defect level engineering: a strategy of optimizing the carrier concentration for high thermoelectric performance," *Energy & Environmental Science,* vol. 11, no. 4, pp. 933-940, 2018.

[71] S. Pal, A. Banerjee, E. Rozenberg, and B. Chaudhuri, "Polaron hopping conduction and thermoelectric power in LaMnO 3+ δ," *Journal of applied Physics,* vol. 89, no. 9, pp. 4955-4961, 2001.

[72] K. C. B. Naidu, T. S. Sarmash, M. Maddaiah, V. N. Reddy, and T. Subbarao, "Structural and dielectric properties of CuO-doped SrTiO3 ceramics," in *AIP Conference Proceedings*, 2015, vol. 1665, no. 1: AIP Publishing LLC, p. 040001.

[73] J. Cao, D. Ekren, Y. Peng, F. Azough, I. A. Kinloch, and R. Freer, "Modulation of Charge Transport at Grain Boundaries in SrTiO3: Toward a High Thermoelectric Power Factor at Room Temperature," *ACS Applied Materials & Interfaces,* 2021.

[74] A. Jonscher, "A new understanding of the dielectric relaxation of solids," *Journal of materials science,* vol. 16, no. 8, pp. 2037-2060, 1981.

[75] A. K. Jonscher, "The ‘universal’dielectric response," *nature,* vol. 267, no. 5613, pp. 673-679, 1977.

[76] T. Dakin, "Conduction and polarization mechanisms and trends in dielectric," *IEEE Electrical Insulation Magazine,* vol. 22, no. 5, pp. 11-28, 2006.

[77] H. Bouaamlat *et al.,* "Dielectric properties, AC conductivity, and electric modulus analysis of bulk ethylcarbazole-terphenyl," *Advances in Materials Science and Engineering,* vol. 2020, 2020.

[78] M. Seyam, A. Bekheet, and A. Elfalaky, "AC conductivity and dielectric properties of In2S3 films," *The European Physical Journal Applied Physics,* vol. 16, no. 2, pp. 99-104, 2001.

[79] M. A. Mahdy, I. El Zawawi, and G. M. Turky, "Lead telluride nanocrystalline thin films: Structure, optical characterization and a broadband dielectric spectroscopy study," *Current Applied Physics,* vol. 19, no. 7, pp. 787-793, 2019.

[80] M. K. Hatalis and D. W. Greve, "Large grain polycrystalline silicon by low-temperature annealing of low-pressure chemical vapor deposited amorphous silicon films," *Journal of applied physics,* vol. 63, no. 7, pp. 2260-2266, 1988.

[81] R. Iverson and R. Reif, "Recrystallization of amorphized polycrystalline silicon films on SiO2: Temperature dependence of the crystallization

parameters," *Journal of applied physics,* vol. 62, no. 5, pp. 1675-1681, 1987.

[82] W.-E. Hong and J.-S. Ro, "Kinetics of solid phase crystallization of amorphous silicon analyzed by Raman spectroscopy," *Journal of Applied Physics,* vol. 114, no. 7, p. 073511, 2013.

[83] A. Ivanauskas, R. Ivanauskas, and I. Ancutiene, "Effect of In-Incorporation and Annealing on CuxSe Thin Films," *Materials,* vol. 14, no. 14, p. 3810, 2021.

[84] A. Astam, Y. Akaltun, and M. Yıldırım, "Conversion of SILAR deposited Cu3Se2 thin films to Cu2− xSe by annealing," *Materials Letters,* vol. 166, pp. 9-11, 2016.

[85] S. F. Abbas, S.-J. Seo, K.-T. Park, B.-S. Kim, and T.-S. Kim, "Effect of grain size on the electrical conductivity of copper–iron alloys," *Journal of Alloys and Compounds,* vol. 720, pp. 8-16, 2017.

[86] N. Swaminathan, P. J. Kamenski, D. Morgan, and I. Szlufarska, "Effects of grain size and grain boundaries on defect production in nanocrystalline 3C–SiC," *Acta Materialia,* vol. 58, no. 8, pp. 2843-2853, 2010/05/01/ 2010, doi: https://doi.org/10.1016/j.actamat.2010.01.009.

[87] T. Šalkus *et al.,* "Influence of grain size effect on electrical properties of Cu6PS5I superionic ceramics," *Solid State Ionics,* vol. 262, pp. 597-600, 2014.

[88] J. Li *et al.,* "Ultrahigh oxidation resistance and high electrical conductivity in copper-silver powder," *Scientific reports,* vol. 6, no. 1, pp. 1-10, 2016.

[89] R. Padma, B. P. Lakshmi, and V. R. Reddy, "Capacitance–frequency (C–f) and conductance–frequency (G–f) characteristics of Ir/n-InGaN Schottky diode as a function of temperature," *Superlattices and Microstructures,* vol. 60, pp. 358-369, 2013.

[90] P. Mannu, M. Palanisamy, G. Bangaru, S. Ramakrishnan, A. Kandasami, and P. Kumar, "Temperature-dependent AC conductivity and dielectric and impedance properties of ternary In–Te–Se nanocomposite thin films," *Applied Physics A,* vol. 125, no. 7, pp. 1-13, 2019.

[91] F. F. Jaldurgam *et al.,* "Optimum sintering method and temperature for cold compact Bismuth Telluride pellets for thermoelectric applications," *Journal of Alloys and Compounds,* vol. 877, p. 160256, 2021.

[92] S. Ihnatsenka, X. Crispin, and I. Zozoulenko, "Understanding hopping transport and thermoelectric properties of conducting polymers," *Physical Review B,* vol. 92, no. 3, p. 035201, 2015.

[93] Y. Şafak-Asar, T. Asar, Ş. Altındal, and S. Özçelik, "Investigation of dielectric relaxation and ac electrical conductivity using impedance spectroscopy method in (AuZn)/TiO2/p-GaAs(110) schottky barrier diodes," *Journal of Alloys and Compounds,* vol. 628, pp. 442-449, 2015/04/15/ 2015, doi: https://doi.org/10.1016/j.jallcom.2014.12.170.

[94] T. T. M. Phan, N. C. Chu, H. N. Xuan, D. T. Pham, I. Martin, and P. Carriere, "Enhancement of polarization property of silane-modified BaTiO3 nanoparticles and its effect in increasing dielectric property of epoxy/BaTiO3 nanocomposites," *Journal of Science: Advanced Materials and Devices,* vol. 1, no. 1, pp. 90-97, 2016.

[95] S. Fadhilah, R. Marhamah, and A. Izzat, "Copper oxide nanoparticles for advanced refrigerant thermophysical properties: mathematical modeling," *Journal of Nanoparticles,* vol. 2014, 2014.

[96] M. Korzhuev, V. Bankina, I. Korolkova, G. Sheina, and E. Obraztsova, "Doping Effects on Mechanical Properties and Microhardness of Cu2− xSe,"

physica status solidi (a), vol. 123, no. 1, pp. 131-137, 1991.

[97] K. Tyagi *et al.*, "Crystal structure and mechanical properties of spark plasma sintered Cu2Se: An efficient photovoltaic and thermoelectric material," *Solid State Communications,* vol. 207, pp. 21-25, 2015.

[98] J. Zhang, C. Zhang, T. Zhu, Y. Yan, X. Su, and X. Tang, "Mechanical Properties and Thermal Stability of the High-Thermoelectric-Performance Cu2Se Compound," *ACS Applied Materials & Interfaces,* 2021/09/14 2021, doi: 10.1021/acsami.1c12533.

[99] M. Li *et al.*, "Ultrahigh figure-of-merit of Cu2Se incorporated with carbon coated boron nanoparticles," *InfoMat,* vol. 1, no. 1, pp. 108-115, 2019.

[100] D. Roy *et al.*, "Synthesis and characterization of precipitation hardened amorphous matrix composite by mechanical alloying and pulse plasma sintering of Al65Cu20Ti15," *Philosophical Magazine,* vol. 89, no. 12, pp. 1051-1061, 2009.

[101] F. Delobel, S. Lemonnier, R. D'Elia, and J. Cambedouzou, "Effects of density on the mechanical properties of spark plasma sintered β-SiC," *Ceramics International,* vol. 46, no. 9, pp. 13244-13254, 2020/06/15/ 2020, doi: https://doi.org/10.1016/j.ceramint.2020.02.101.

APPENDICES

Appendix A: Supplementary data of bismuth telluride

Figure S1. XRD profile of (a) commercial p-type and n-type powders, (b) Conventional sintered p-type Bi_2Te_3, (c) Conventional sintered n-type Bi_2Te_3, (d) Tube sintered p-type Bi_2Te_3, (e) Tube sintered n-type Bi_2Te_3.

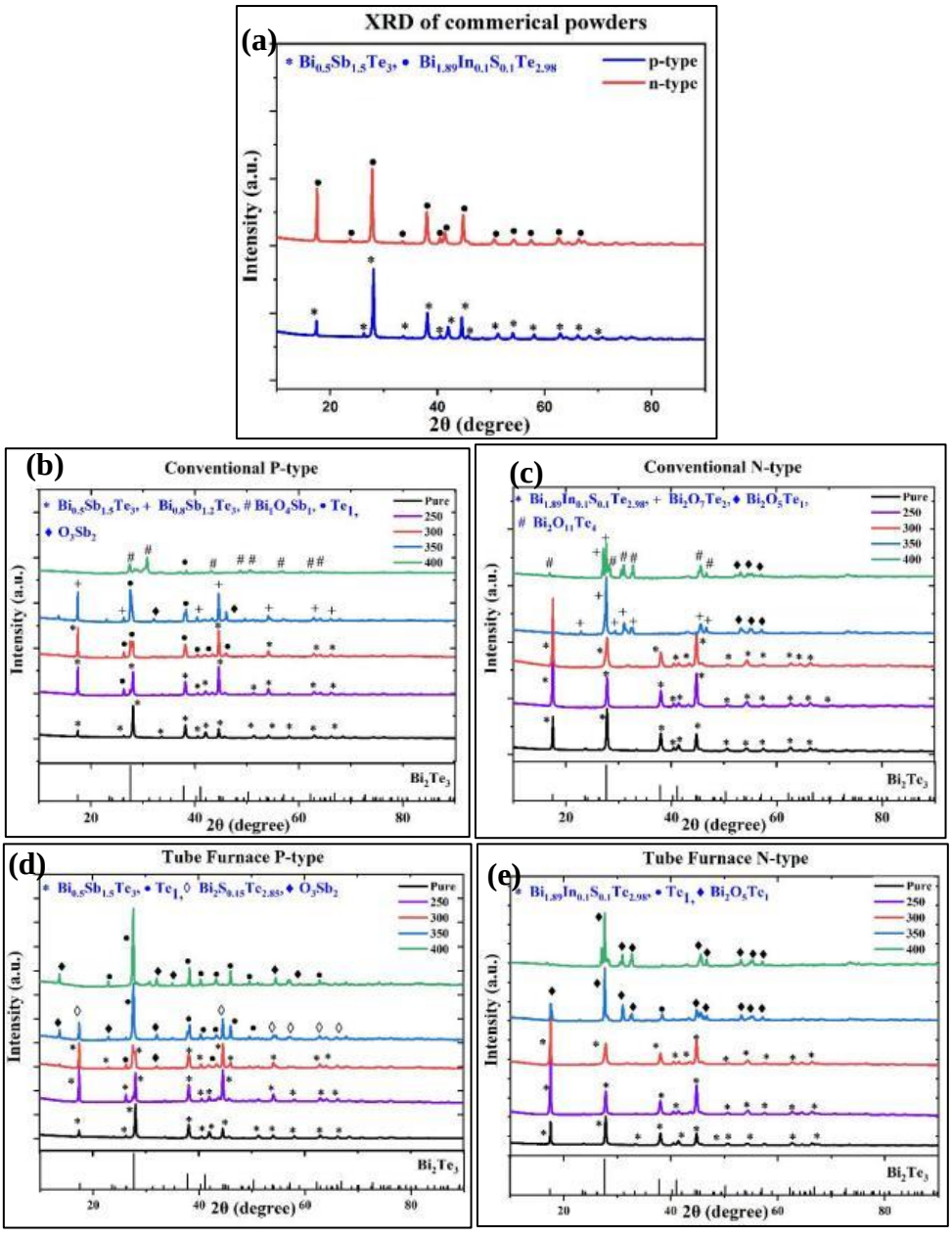

Figure S2. Field emission scanning electron microscopy (FESEM) images at 1µm of (a) pristine p-type Bi_2Te_3 sample, (b) BP250, (c) BP300, (d) BP350.

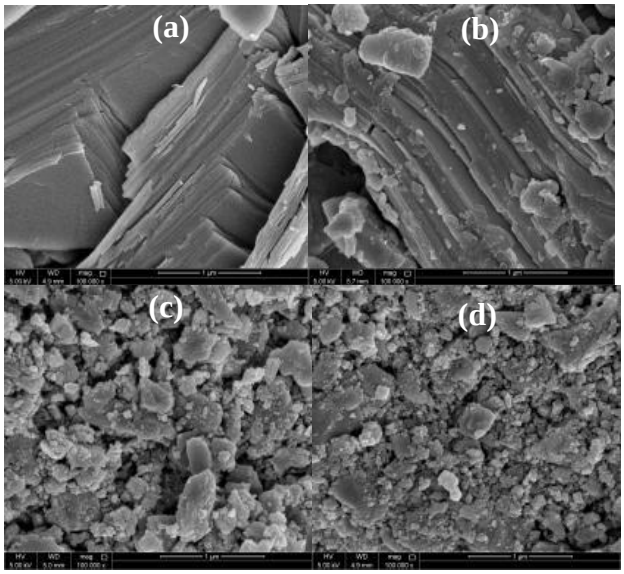

Figure S3. Field emission scanning electron microscopy (FESEM) images at 1µm of (a) pristine p-type Bi_2Te_3 sample, (b) TP250, (c) TP300, (d) TP350. Nanoparticles of sizes less than 1 µm can be observed in the SEM images of samples sintered at 300^{o}C and 350^{o}C.

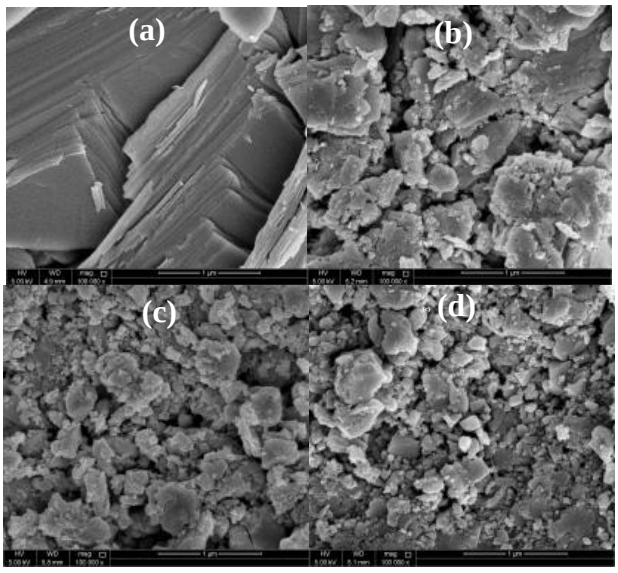

Figure S4. Field emission scanning electron microscopy (FESEM) images at 1μm of (a) pristine p-type Bi_2Te_3 sample, (b) BP250, (c) BP300, (d) BP350.

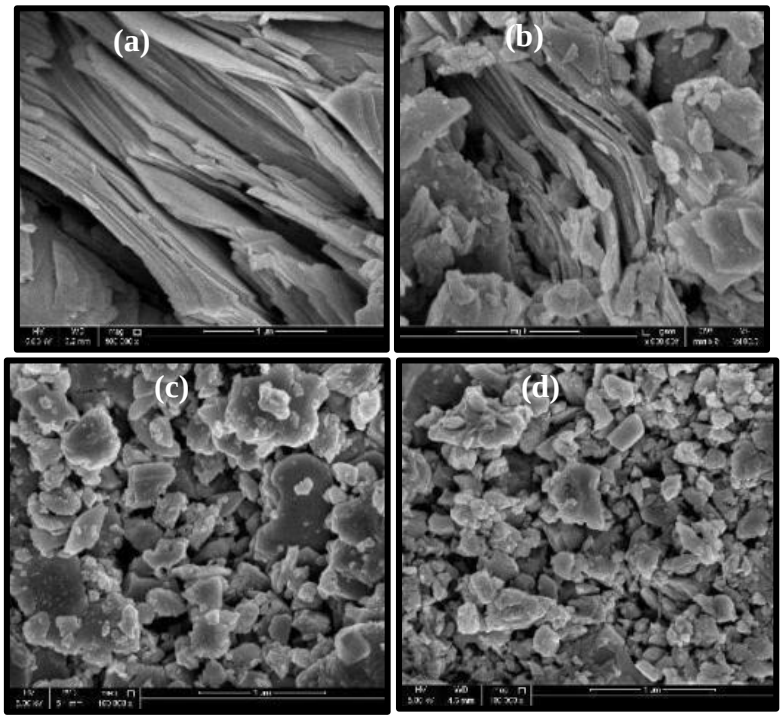

Figure S5. Field emission scanning electron microscopy (FESEM) images at 1μm of (a) pristine p-type Bi_2Te_3 sample, (b) TN250, (c) TN300, (d) TN350.

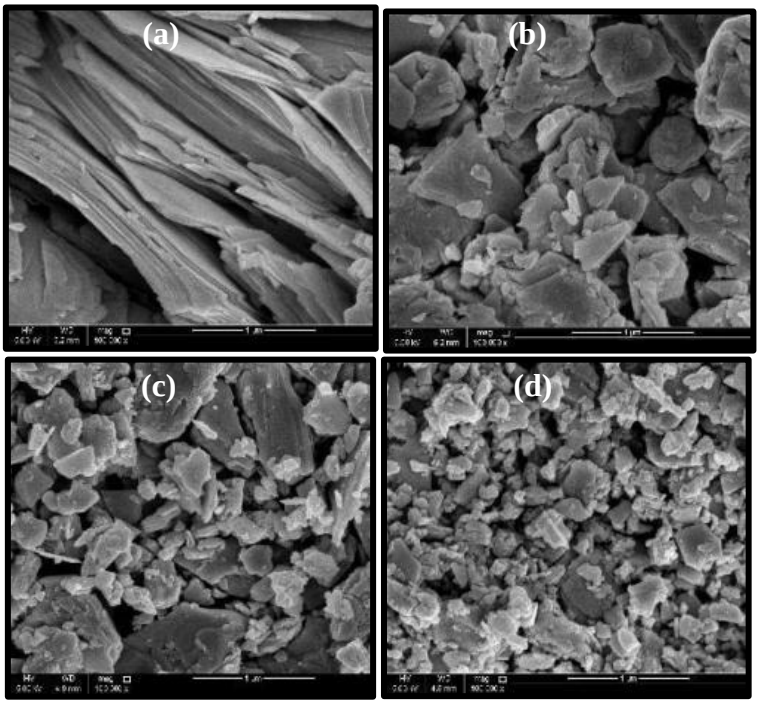

Figure S6. Field emission scanning electron microscopy (FESEM) images at 3µm of (a) cross-section pristine p-type Bi_2Te_3 sample, (b) BN250 (c) BN300, (d) BN350.

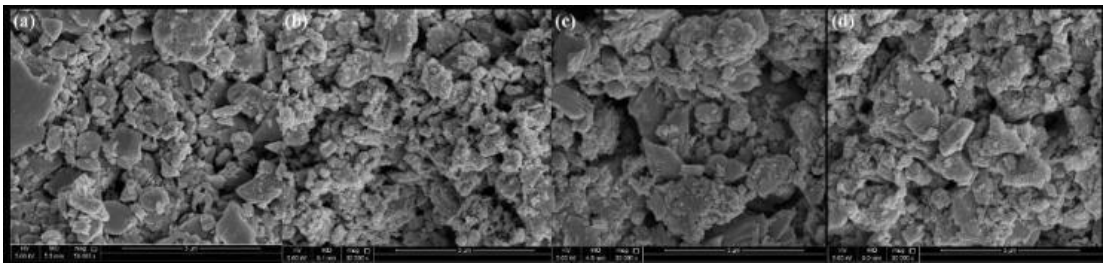

Figure S7. Field emission scanning electron microscopy (FESEM) images at 3µm of (a) cross-section pristine n-type Bi_2Te_3 sample, (b) BN300 (c) MN300, (d) TN300.

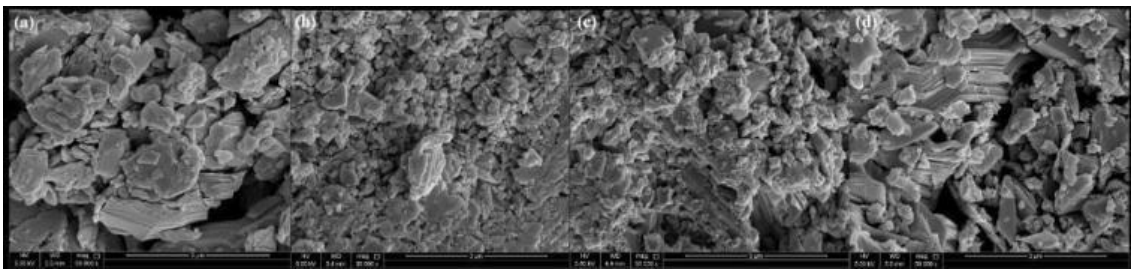

Figure S8. The variation of the AC electrical conductivity with temperature at different frequencies of bismuth telluride sintered in box, microwave, and tube furnace at 300ºC and 350ºC.

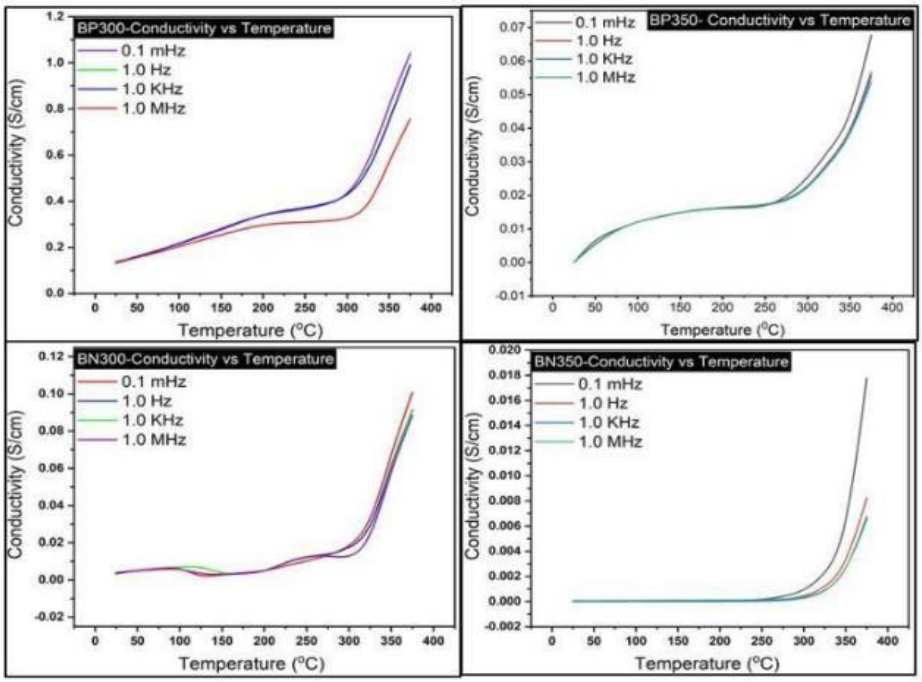

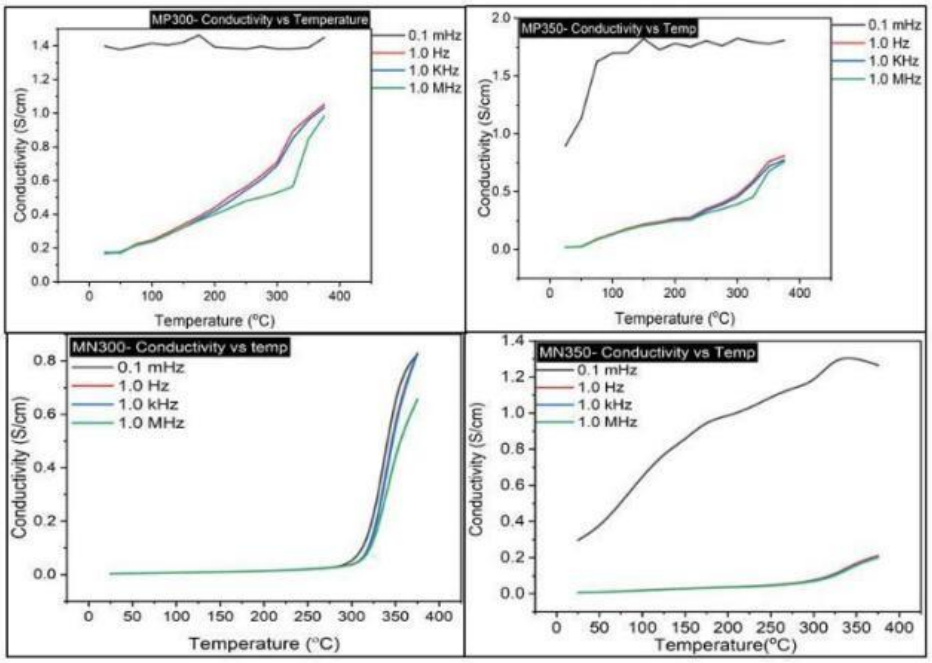
MP300- Conductivity vs Temperature
0.1 mHz
1.0 Hz
1.0 KHz
1.0 MHz
Conductivity (S/cm)
Temperature (°C)
MP350- Conductivity vs Temp
0.1 mHz
1.0 Hz
1.0 KHz
1.0 MHz
Conductivity (S/cm)
Temperature (°C)
MN300- Conductivity vs temp
0.1 mHz
1.0 Hz
1.0 kHz
1.0 MHz
Conductivity (S/cm)
Temperature (°C)
MN350- Conductivity vs Temp
0.1 mHz
1.0 Hz
1.0 kHz
1.0 MHz
Conductivity (S/cm)
Temperature(°C)

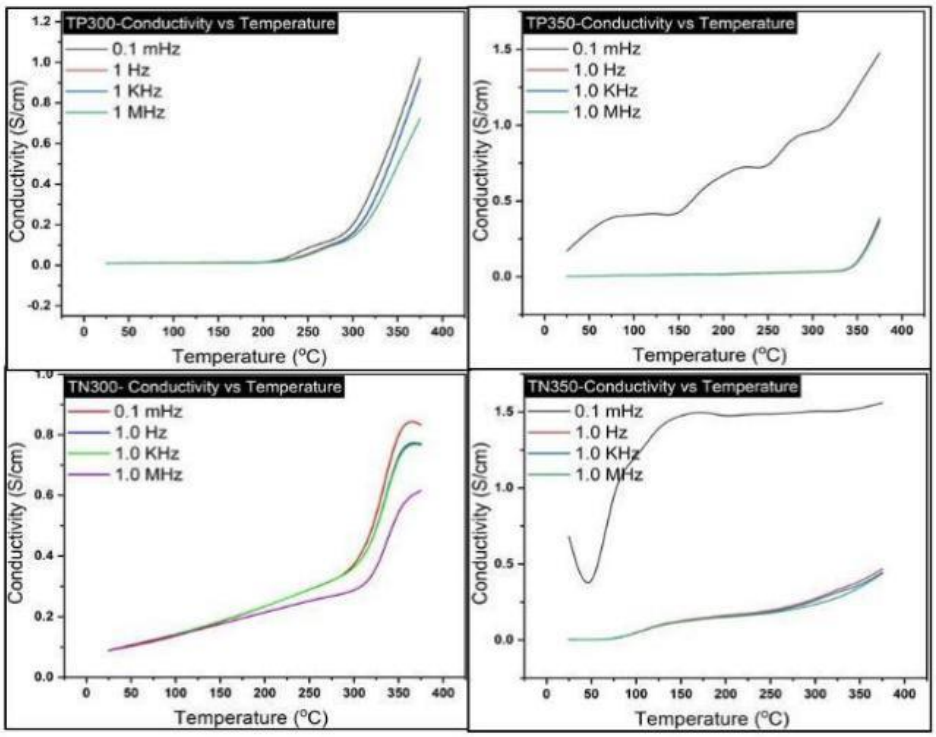
TP300-Conductivity vs Temperature
0.1 mHz
1 Hz
1 KHz
1 MHz
Conductivity (S/cm)
Temperature (°C)
TP350-Conductivity vs Temperature
0.1 mHz
1.0 Hz
1.0 KHz
1.0 MHz
Conductivity (S/cm)
Temperature (°C)
TN300- Conductivity vs Temperature
0.1 mHz
1.0 Hz
1.0 KHz
1.0 MHz
Conductivity (S/cm)
Temperature (°C)
TN350-Conductivity vs Temperature
0.1 mHz
1.0 Hz
1.0 KHz
1.0 MHz
Conductivity (S/cm)
Temperature (°C)

Figure S9. The variation of the AC electrical conductivity with frequency at different temperatures of bismuth telluride sintered in box, microwave, and tube furnace at 300ºC and 350ºC.

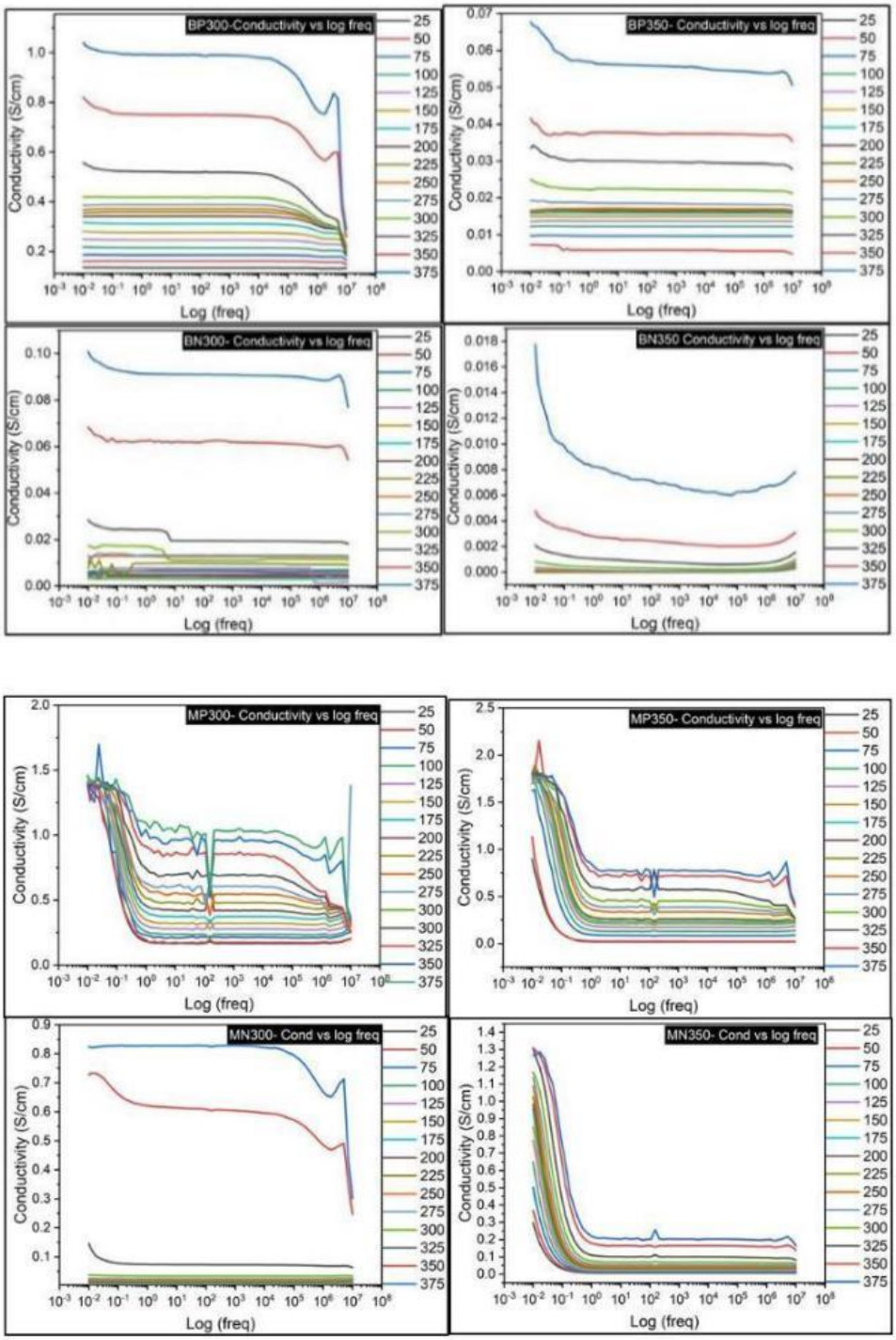

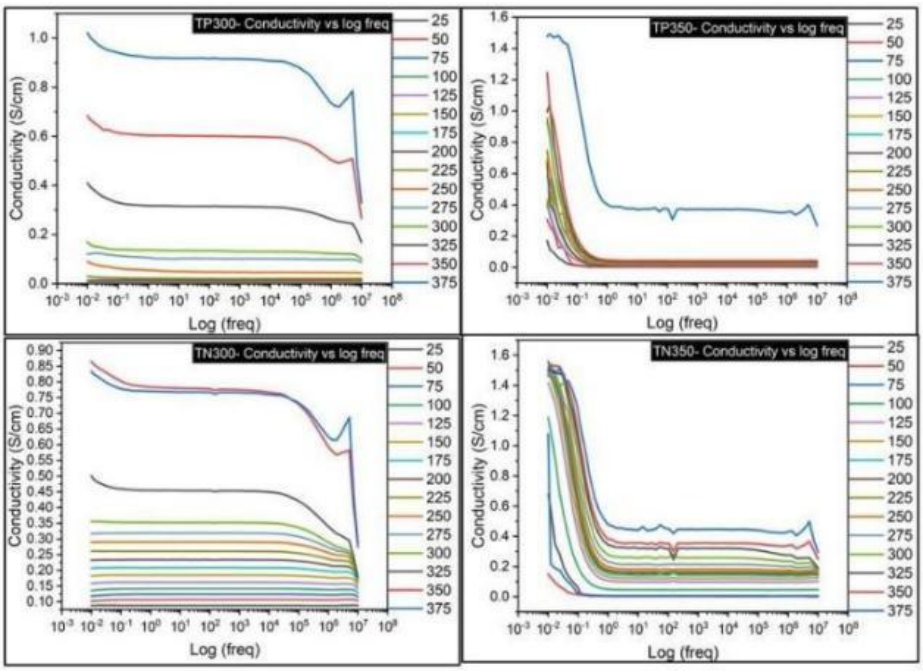

Figure S10. The variation of the dielectric permittivity storage with frequency of bismuth telluride sintered in box, microwave, and tube furnace at 300ºC and 350ºC.

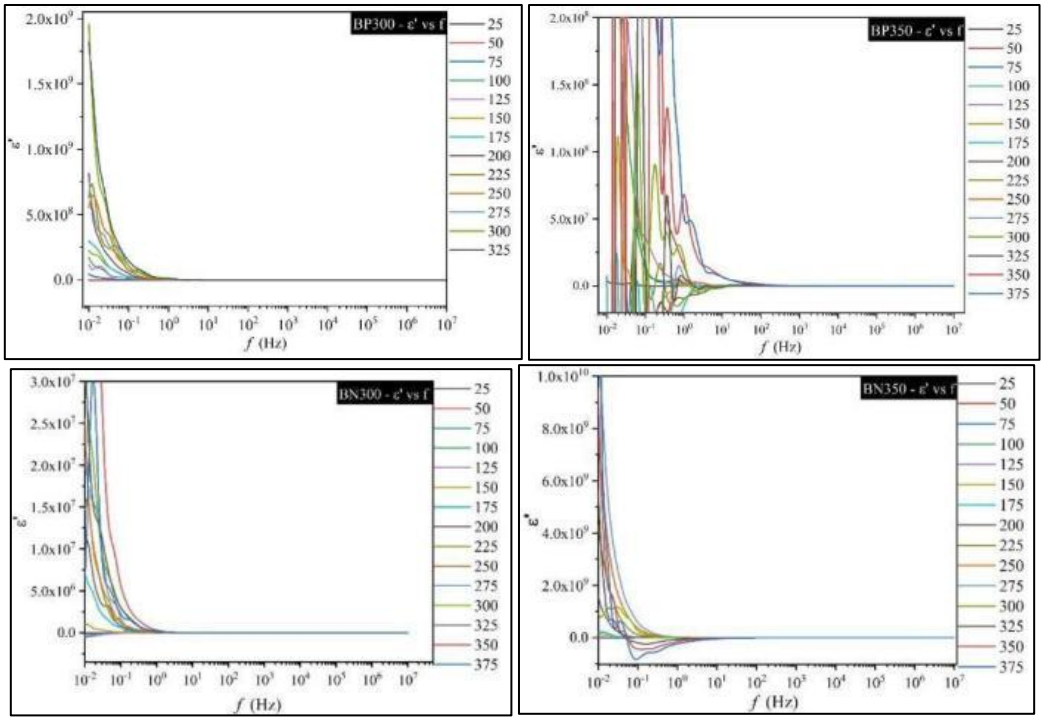

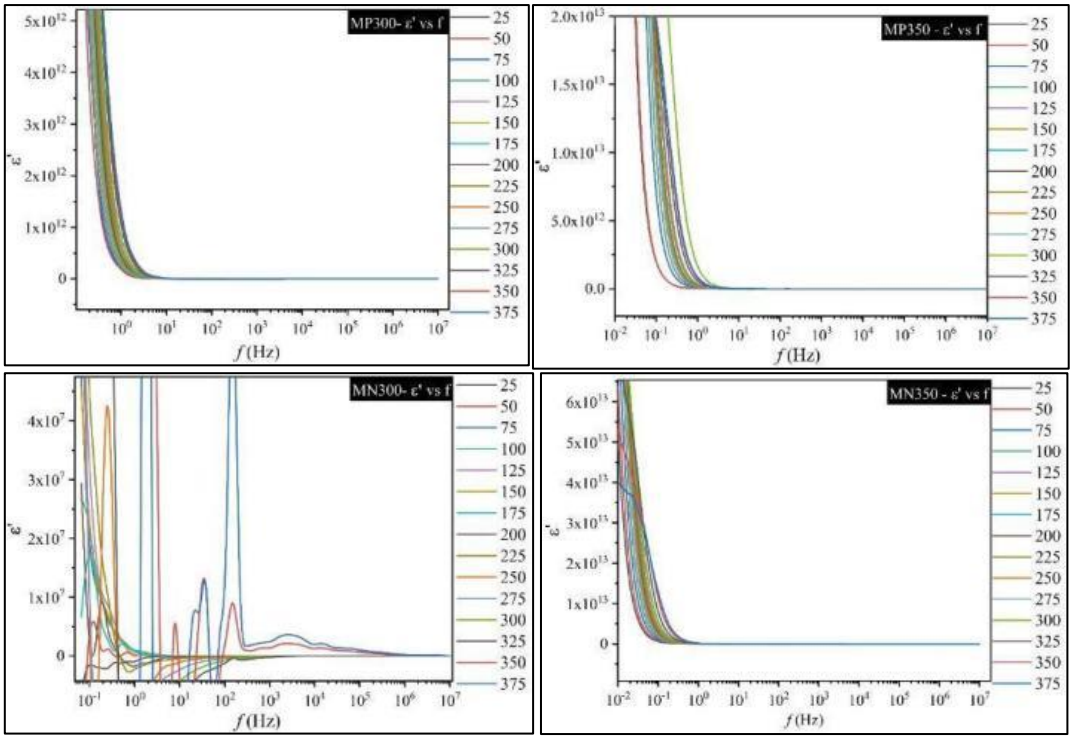
MP300- ε' vs f
MP350 - ε' vs f
MN300- ε' vs f
MN350 - ε' vs f
ε'
f (Hz)
25
50
75
100
125
150
175
200
225
250
275
300
325
350
375

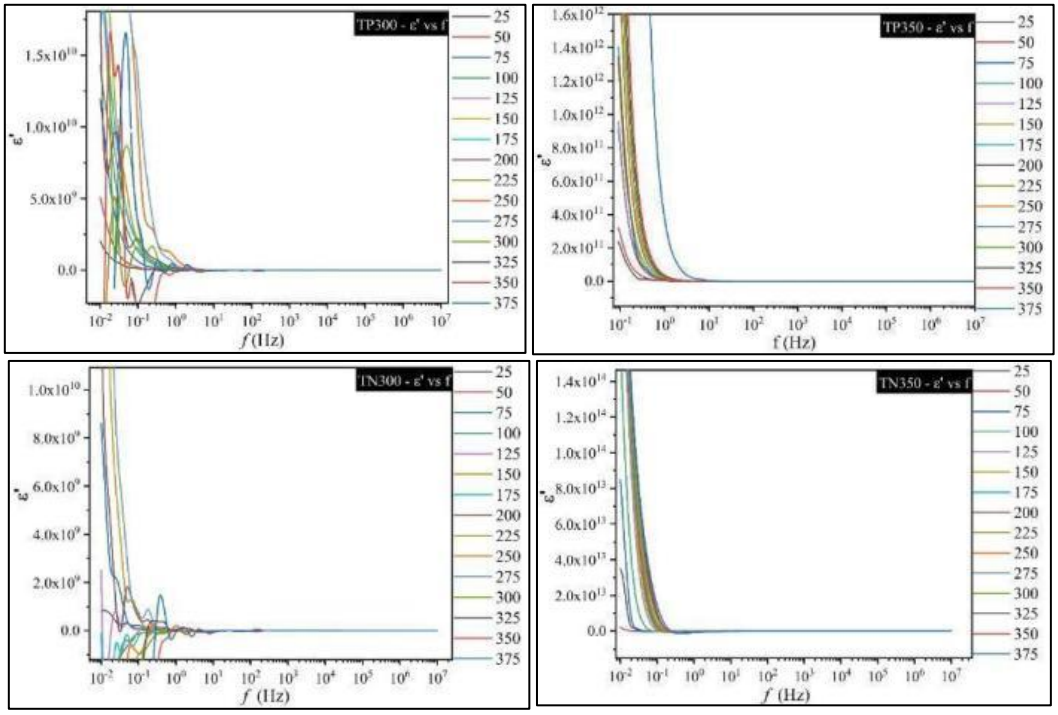
TP300 - ε' vs f
TP350 - ε' vs f
TN300 - ε' vs f
TN350 - ε' vs f
ε'
f (Hz)
25
50
75
100
125
150
175
200
225
250
275
300
325
350
375

Figure S11**.** The variation of the dielectric permittivity loss with frequency of bismuth telluride sintered in box, microwave, and tube furnace at 300^{o}C and 350^{o}C.

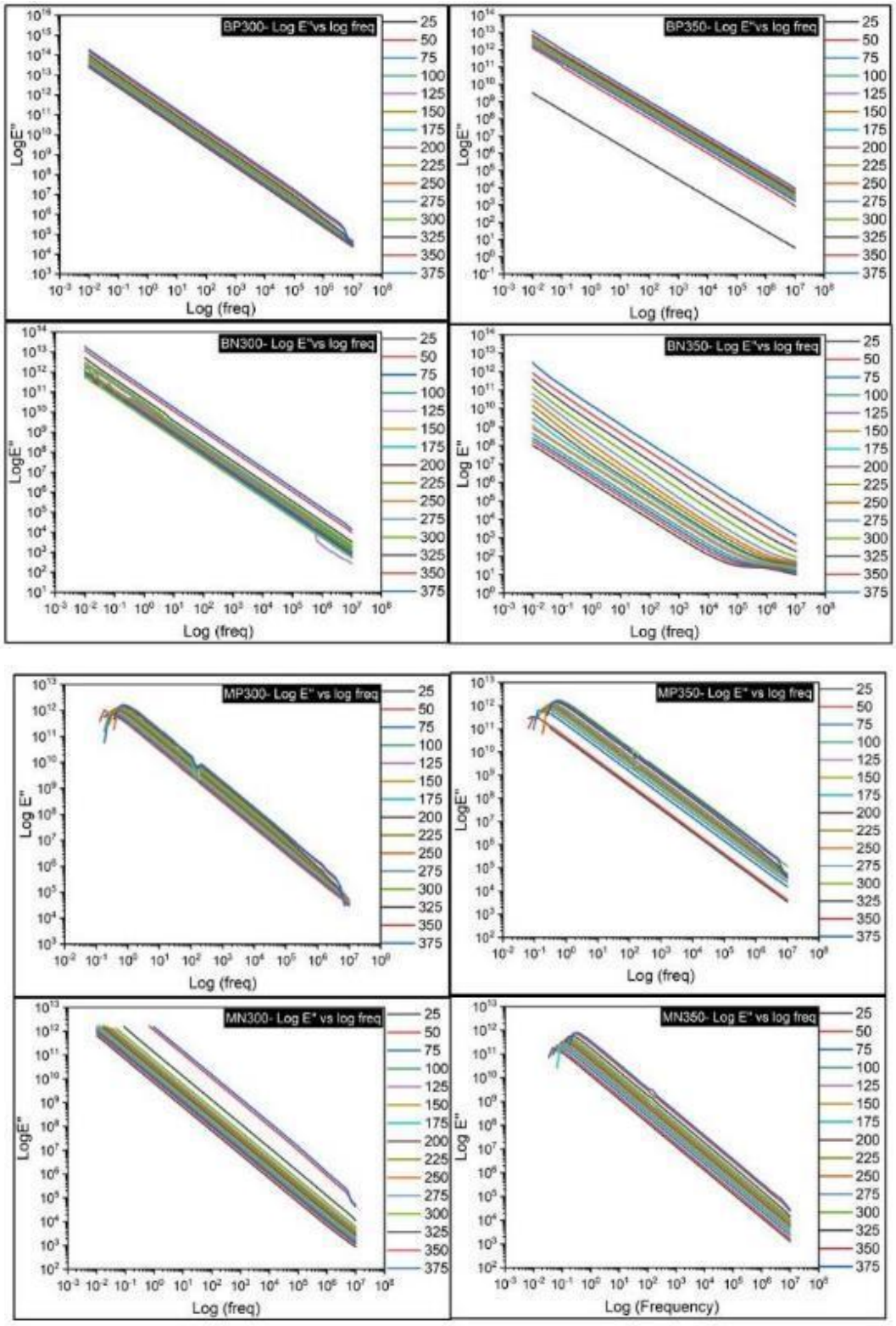

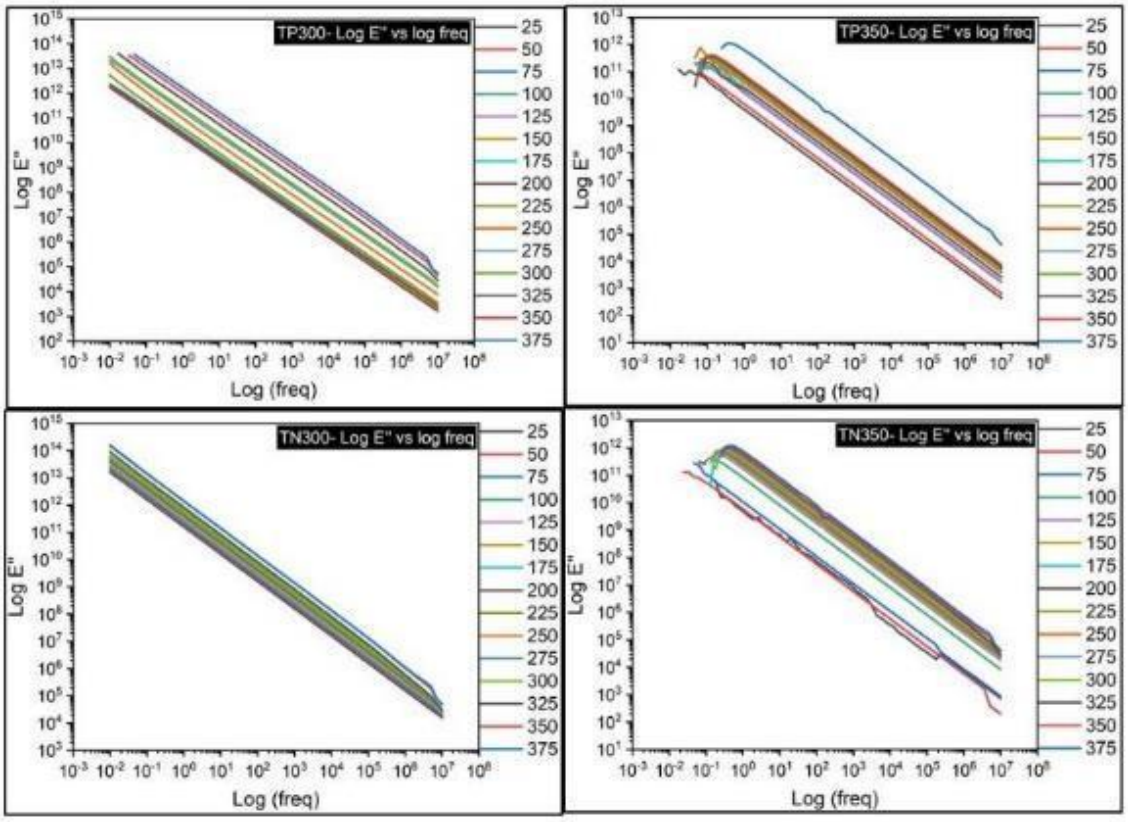

Figure S12. (a) Scanning electron microscopy (SEM) image of the MP250 at 3 µm, (b) low magnification transmission electron microscopy (TEM) image with SAED pattern (selected area electron diffraction) shown in the inset of the MP250 pellet at 200 nm resolution, (c) High-resolution TEM (HRTEM) image of MP250 pellet at 5 nm, (d) Zoom in TEM image at 50 nm resolution.

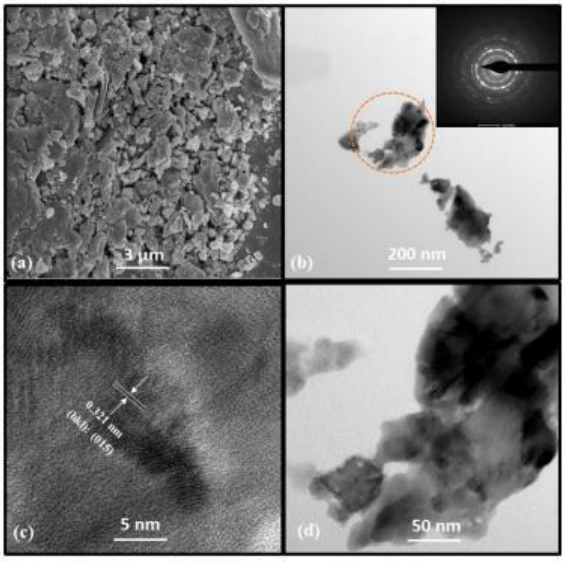

Figure S13. (a) Scanning electron microscopy (SEM) image of the MP300 at 3 µm, (b) low magnification transmission electron microscopy (TEM) image with SAED pattern (selected area electron diffraction) shown in the inset of the MP300 pellet at 200 nm resolution, (c) High-resolution TEM (HRTEM) image of MP300 pellet at 5 nm, (d) Zoom in TEM image at 50 nm resolution.

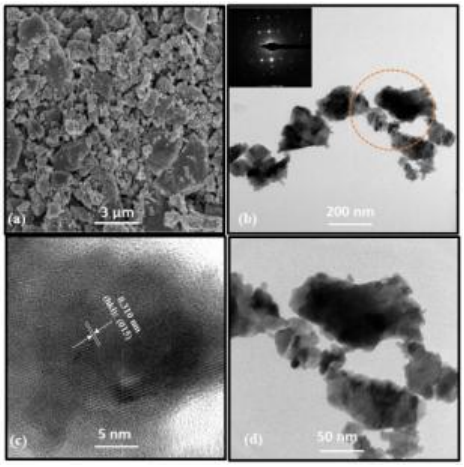

Figure S14. (a) Scanning electron microscopy (SEM) image of the MN250 at 3 µm, (b) low magnification transmission electron microscopy (TEM) image with SAED pattern (selected area electron diffraction) shown in the inset of the MN250 pellet at 200 nm resolution, (c) High-resolution TEM (HRTEM) image of MN250 at 5 nm, (d) Zoom in TEM image at 50 nm resolution.

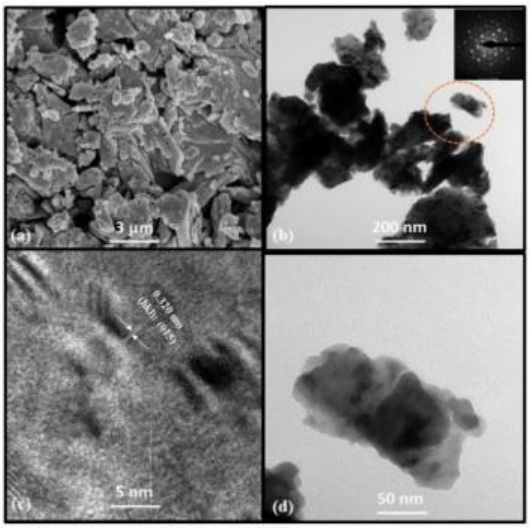

Figure S15. (a) Scanning electron microscopy (SEM) image of the MN300 at 3 µm, (b) low magnification transmission electron microscopy (TEM) image with SAED pattern (selected area electron diffraction) shown in the inset of the MN300 pellet at 200 nm resolution, (c) High-resolution TEM (HRTEM) image of MN300 pellet at 5 nm, (d) Zoom in TEM image at 50 nm resolution.

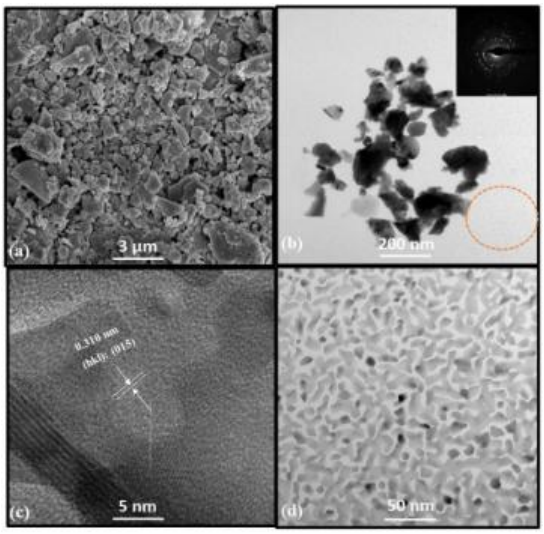

Appendix B: Supplementary data of copper selenide

Figure S1. Copper selenide pellet formation by (a) Cold compaction, (b) Hot pressing.

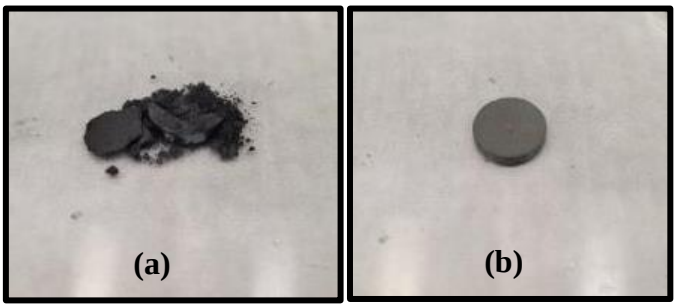

Figure S2. (a) Grain size variation with annealing temperature of microwave sintered p-type copper selenide TE material, (b) comparison of XRD profile of pure samples and samples annealed at 725^{o}C (the CS725 sample has completely oxidized indicating unsuitability of high annealing temperatures).

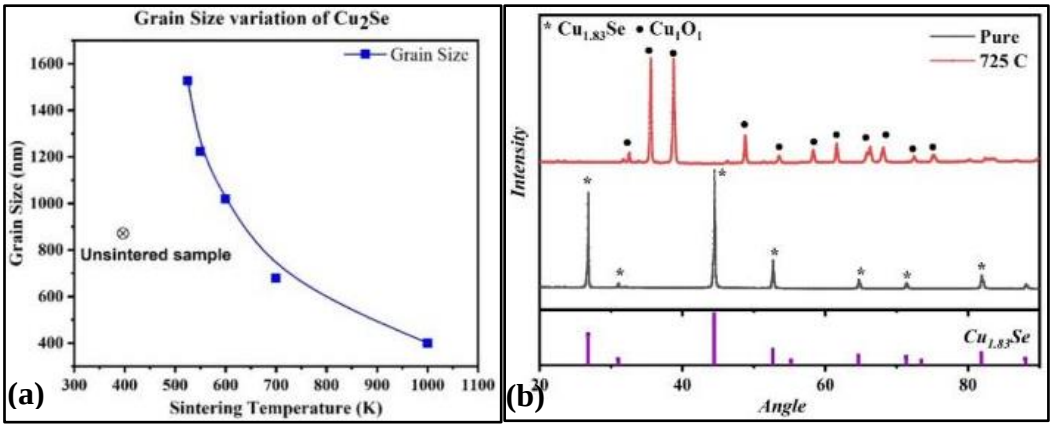

Figure S3. The variation of selenium with annealing temperature of the samples from the EDX data.

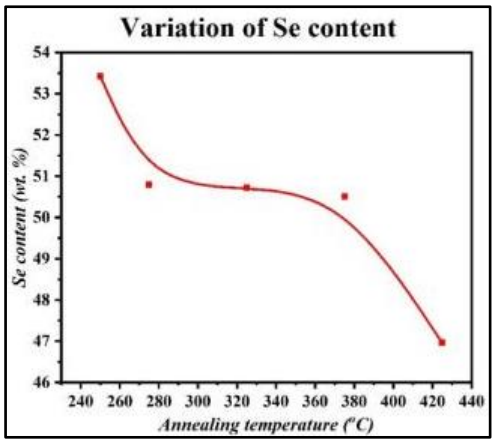

Figure S4. Alteration of (a) the AC electrical conductivity with temperature, (b) the AC electrical conductivity with frequency, (c) the AC capacitance with frequency, (d) the dielectric permittivity storage with frequency, (e) the dielectric permittivity loss with frequency, (f) the tan(δ) with frequency, in the range 25°C to 400°C at frequencies 10 mHz, 1Hz, 1kHz, and 1 MHz for the sample CS275.

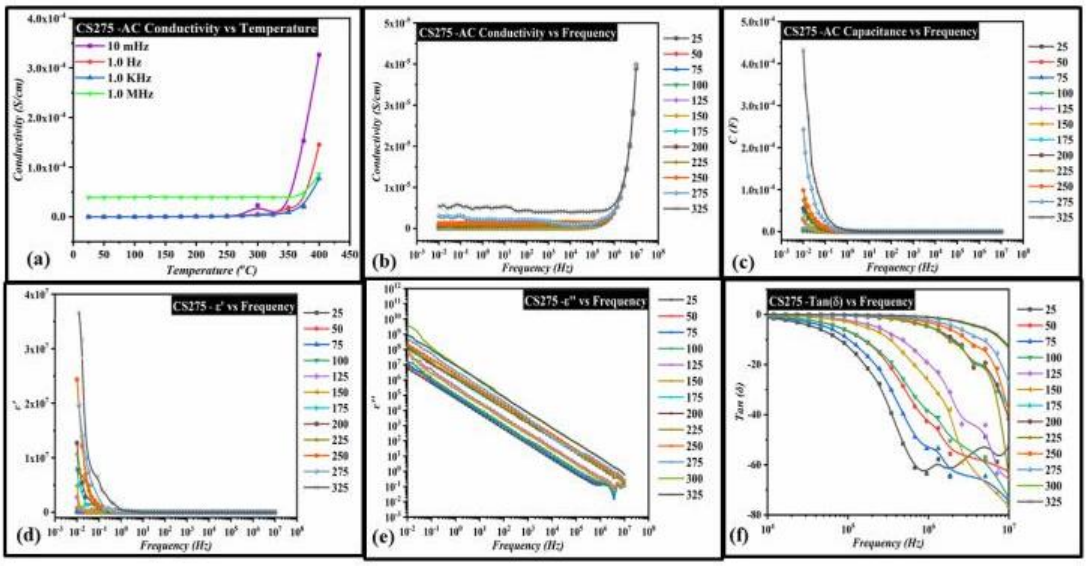

Figure S5. Alteration of (a) the AC electrical conductivity with temperature, (b) the AC electrical conductivity with frequency, (c) the AC capacitance with frequency, (d) the dielectric permittivity storage with frequency, (e) the dielectric permittivity loss with frequency, (f) the tan(δ) with frequency, in the range 25°C to 400°C at frequencies 10 mHz, 1Hz, 1kHz, and 1 MHz for the sample CS325.

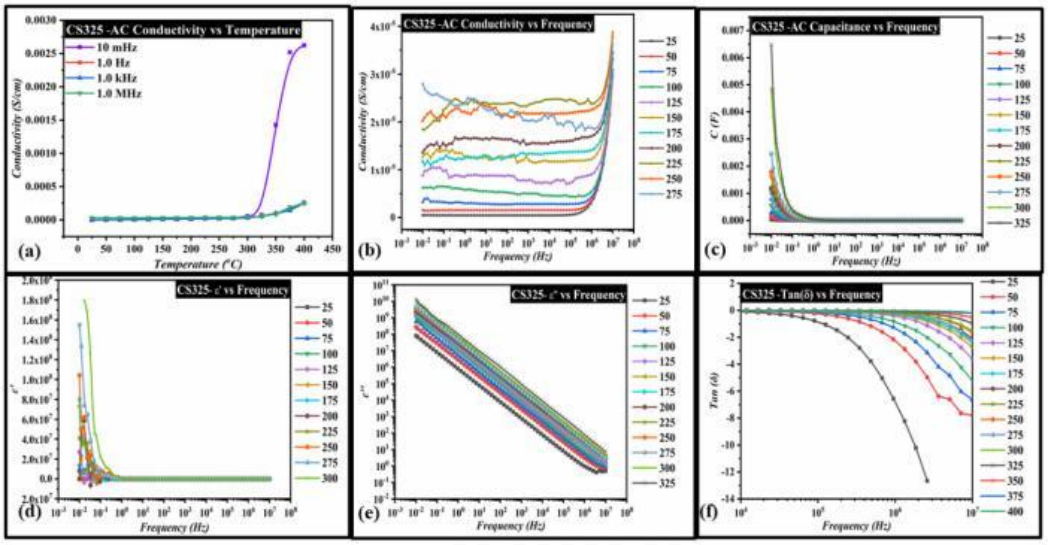

Figure S6. Alteration of (a) the AC electrical conductivity with temperature, (b) the AC electrical conductivity with frequency, (c) the AC capacitance with frequency, (d) the dielectric permittivity storage with frequency, (e) the dielectric permittivity loss with frequency, (f) the tan(δ) with frequency, in the range 25^{o}C to 400^{o}C at frequencies 10 mHz, 1Hz, 1kHz, and 1 MHz for the sample CS375.

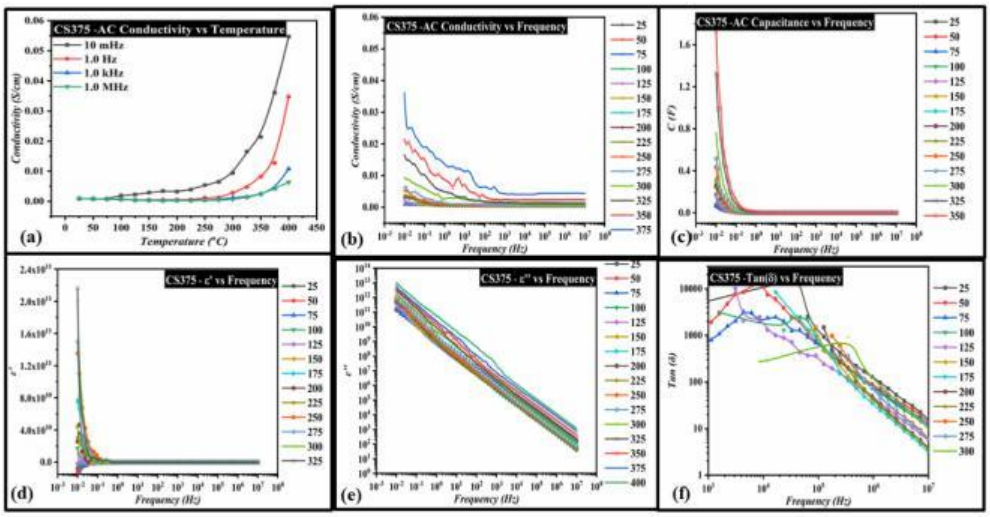

Figure S7. Alteration of (a) the AC electrical conductivity with temperature, (b) the AC electrical conductivity with frequency, (c) the AC capacitance with frequency, (d) the dielectric permittivity storage with frequency, (e) the dielectric permittivity loss with frequency, (f) the tan(δ) with frequency, in the range 25^{o}C to 400^{o}C at frequencies 10 mHz, 1Hz, 1kHz, and 1 MHz for the sample CS425.

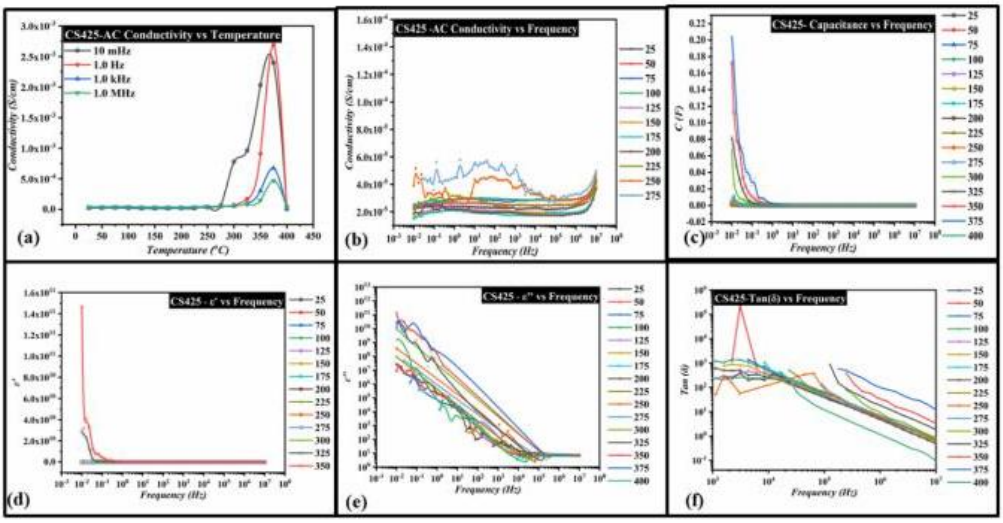

Figure S8. Alteration of (a) the AC electrical conductivity with temperature, (b) the AC electrical conductivity with frequency, (c) the AC capacitance with frequency, (d) the dielectric permittivity storage with frequency, (e) the dielectric permittivity loss with frequency, (f) the tan(δ) with frequency, in the range 25^{o}C to 400^{o}C at frequencies 10 mHz, 1Hz, 1kHz, and 1 MHz for the pristine sample.

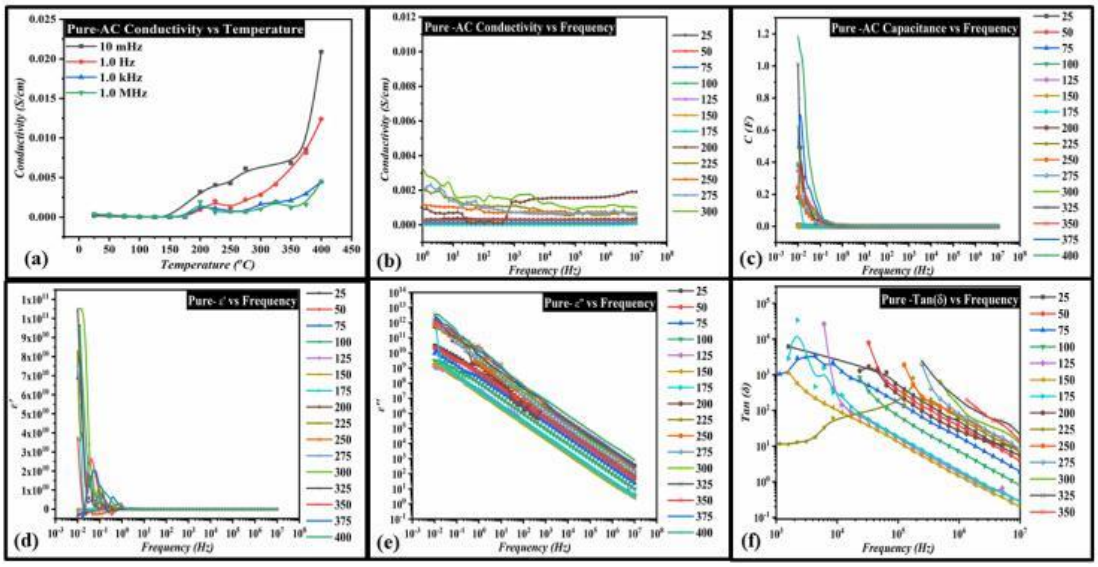

Figure S9. The variation of thermal diffusivity and specific heat of the samples with annealing temperature.

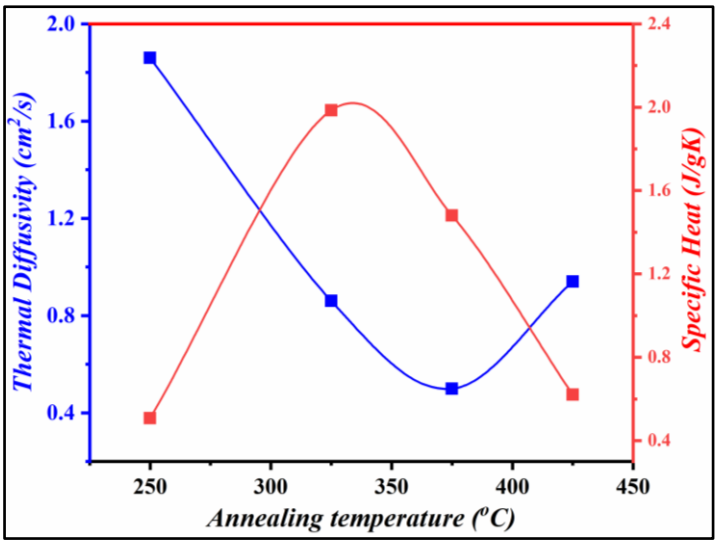

Figure S10. The variation of the average particle size distribution of copper selenide with annealing temperature from TEM analysis.